

Investigation of Thermal Properties of Citric Acid modified Magnetic Nanofluids and Distributions of Drops Deposition Patterns affected by Thermal Strategies

Zeyu Liu, MEng. BEng.

Thesis submitted to the University of Nottingham for the degree of

Doctor of Philosophy

June 2020

ABSTRACT

Over the past decades, the increasing interests in nanofluids offer more potential to control various performances in different applications. Magnetic nanofluids (MNFs) have been extensively studied in many thermal applications due to both the magnetism and the fluidity. Both stability and thermal properties are important indicators in the process of applications. Moreover, poor colloidal stability leads to particle aggregations even precipitations, which results in clogging of flow channels and the pressure drop. Consequently, nanofluids studied in this way cannot be reliable for practical applications due to unstable physical properties.

The first aim of this work is to investigate the synthesis procedure and thermal properties of well-dispersed MNFs. In terms of the synthesis, citric acid (CA) modified MNFs are prepared by a two-step method. The synthesis results show that the stability of CA modified MNFs is sensitive to pH values. The MNFs exhibit well-dispersed distribution when pH is at neutral values. Meanwhile, thermal conductivity can be predicted by the Maxwell model, and the proper aggregation can improve thermal conductivity. For convective heat transfer, it shows that the convective heat transfer of MNFs increases by 10% when the Reynolds number is over 2500. Meanwhile, a similar enhancement is obtained in the thermal efficiency of the solar collector. The experimental results show that the thermal efficiency of parabolic trough solar collector, 0.05 vol.% of MNFs, has a great potential enhancement, which is 25% higher than that of the water-based absorber and 12% higher than that of the selective surface absorber under the external magnetic field. Apart from that, due to the well-dispersed property, the deposition pattern of MNFs is also studied in the following section.

In the framework of the grant of H2020-MSCA-RISE, the distribution of deposition patterns affected by thermal strategies is also studied. Deposition patterns are widely applied in many industrial applications, such as inkjet printing, liquid biopsy, medical science, etc. Previous researchers have investigated different methods to control patterns by adjusting droplet properties. This section is devoted to experimentally exploring how to control the distribution of deposition formations by thermal strategies without changing chemicals. Firstly, two kinds of droplets, including saline and MNFs droplets, have been experimentally conducted by controlling substrate temperatures, ranging from cooling to heating temperatures. The experimental results show that deposited patterns transit from the uniformity, the ring-like structure, to the dual ring structure with the increasing temperature. Meanwhile, IR camera is used to analyse the distribution of surface temperatures, and 3 μm microbeads are applied to track the flow motion of the solute inside for different temperatures. Secondly, deposition patterns with different wettability are also investigated by the local heating. The whole process of the evaporation is recorded by a CCD camera. Experimental results show that the laser-induced local heating changes particle deposition patterns from the ring-like structure to the dot-like structure on a hydrophilic surface, transporting more saline solvents to the centre. Meanwhile, a hydrophobic surface is also investigated. The results show that particles tend to assemble at the central area, but the pattern is slightly different compared to that on the hydrophilic surface. The experimental investigation shows that thermal strategies have great potential to control the distribution of droplet deposition patterns.

LIST OF PUBLICATIONS

Journals

1. **Zeyu Liu**, Yuying Yan, Rong Fu, and Mustafa Alsaady. "Enhancement of solar energy collection with magnetic nanofluids." Thermal Science and Engineering Progress 8 (2018): 130-135.
2. **Zeyu Liu**, Yuying Yan, Xin Wang, and Xinyong Chen. "Droplet deposition pattern affected by different heating directions." Journal of Bionic Engineering 17, no.4 (2020): 795-801.
3. Rong Fu, **Zeyu Liu**, Yiyi Chen, and Yuying Yan. "Experimental investigation of turbulent forced heat transfer of Fe_3O_4 ethylene glycol–water nanofluid with highly disaggregated particles." Thermal Science and Engineering Progress 10 (2019): 1-9.
4. Rong Fu, **Zeyu Liu**, Yiyi Chen, and Yuying Yan. "Experimental Investigation of the Influence of Particle Disaggregation on Shear Thinning of Fe_3O_4 Ethylene Glycol-Water Nanofluid." Journal of Nanofluids 7, no. 4 (2018): 613-619.
5. Rong Fu, Yuying Yan, Clive Roberts, **Zeyu Liu**, and Yiyi Chen. "The role of dipole interactions in hyperthermia heating colloidal clusters of densely-packed superparamagnetic nanoparticles." Scientific reports 8, no. 1 (2018): 4704.

Conference

1. **Zeyu Liu**, Xin Wang, Yuying Yan, Xinyong Chen, "Thermal strategies for controlling droplet deposition patterns", UK heat transfer conference 2019, Nottingham, UK.
2. **Zeyu Liu**, Xin Wang, Yuying Yan, Xinyong Chen, "Droplet deposition pattern affected by substrate temperatures", Progress 100 Symposium and 2nd ThermaSMART Annual Workshop, Kyushu University, Japan.
3. **Zeyu Liu**, Yuying Yan, Rong Fu, and Mustafa Alsaady, "Experimental Study on Solar Energy Collection with Magnetic Nanofluids", Sustainable Energy Technology 2017, Bologna, Italy.

ACKNOWLEDGEMENT

Working on a PhD programme is one of the most important decisions in my life. It not only opens a gate for me to understand the nature of life, but also gives me an opportunity to think about my career and life critically.

First and foremost, I would like to express my sincere gratitude to my supervisor, Professor Yuying Yan, for his patient guidance throughout my 4 years' PhD study. It is impossible to complete my PhD work without his inspiring advice and helpful assistance.

I am also grateful for my colleagues and technical staff in the Built Environment Department and Pharmacy Department. Thanks to Tony Gospel, Andrew Matthews, Dr Xinyong Chen and James Hazzledine for their professional advice and patient assistance in the laboratory. Especially, my special thank goes to Dr Rong Fu, who gave me many helpful suggestions at the beginning of my PhD period. My thanks are extended to Jiaju Hong, Yiyi Chen, Kuo Huang, Wei Gong, Xin Wang, Thomas Werner, Edward Wright, Li Wang. Thanks for meeting them and we would share very beautiful memories for living and studying in Nottingham.

I would like to thank the China Scholarship Council (CSC) for funding living expenses during my PhD period. Meanwhile, I would like to thank ThermaSMART project for my academic exchanges that offer me more opportunities to communicate with researchers in relevant fields.

Most importantly, I am extraordinarily grateful to my parents and my wife. Their unconditional understandings and loves are my safest harbour. They are my warmest parts, lighting me in the darkest time, encouraging me to get through the

most difficult moments. Thank you for all your support and you all are the most precious gifts given in my life.

NOMENCLATURE

Symbol	Meaning	Unit
d_f	Fractal dimension of the aggregates	
k_{copper}	Thermal conductivity of the copper	W/(m·K)
r_a	Radius of aggregates	m
r_p	Radius of particles	m
T_c	Critical temperature	°C
t_f	Mean bulk temperature of the fluid	°C
$t_{w,in}$	Inner wall temperature	°C
$t_{w,out}$	Outer surface temperature of the tube	°C
w_c	Work of cohesion	J/m^2
H_c	Coercivity	A/m
k	Thermal conductivity	W/(m·K)
k_B	Boltzmann constant	
K_{eff}	Magnetic anisotropy constant	
K_S	Surface anisotropy	J/m^2
K_V	Volume anisotropy constant	
m	Mass flow rate	kg/s
M_r	Residual magnetization	A/m
M_s	Maximum magnetization	A/m
Nu	Nusselt number	
q	Heat flux	W/m^2
$S_{2/1}$	Spreading of 2 on 1	
T	Temperature	°C
T_B	Blocking temperature	°C
V	Molar volume of a substance	L/mol
V_p	Particle volume	m^3

Greek symbols

μ_f	Dynamic viscosity at the mean bulk temperature of the fluid	N·s/m^2
μ_r	Ratio of the viscosity of nanofluids to that of the base liquids	
$\mu_{w,f}$	Dynamic viscosity at the inner wall temperature	N·s/m^2
ρ_{bl}	Density of the base liquid	kg/m^3
ρ_n	Density of particles	kg/m^3
ρ_{nf}	Density of nanofluids	kg/m^3
ρ_s	Density of particles	kg/m^3
γ	Surface tension	J / m^2
δ	Overall uncertainty	
τ_0	Attempt time	s
τ_N	Nèel relaxation time	s
ϕ	Volume fraction of particles	

Abbreviation

bl	Base liquid
CA	Citric acid
CAH	Contact angle hysteresis
CSP	Concentrated solar panel
DSC	Differential Scanning Calorimeter
DLS	Dynamic light scattering
IC	Internal combustion
MNFs	Magnetic nanofluids
TEM	Transmission electron microscopy

Table of Contents

ABSTRACT I

LIST OF PUBLICATIONS III

ACKNOWLEDGEMENT V

NOMENCLATURE VII

Table of Contents IX

List of Figures XII

List of Tables XVII

Chapter 1 Introduction 1

1.1 General Background 1

1.2 Research Objectives 8

1.3 Outline of the Work 9

Chapter 2 Literature Review for Characters of Magnetic Nanofluids (MNFs) and Recent Advances in Droplet Evaporation 11

2.1 Synthesis of Magnetic Nanofluids 11

2.2 Thermal Properties of Magnetic Nanofluids 13

2.2.1 Density 13

2.2.2 Specific heat capacity 14

2.2.3 Viscosity 15

2.2.4 Thermal conductivity 17

2.2.5 Convective heat transfer 18

2.3 Sessile Droplet Evaporation 20

2.3.1 Wettability 21

2.3.2 Evaporation modes 21

2.3.3 Flow fields of the drying droplet 22

2.4 Typical Drying Patterns 23

2.4.1 The ring-structure pattern 24

2.4.2 The uniform deposition pattern 25

2.4.3 The dot-like structure pattern 26
2.4.4 The stick-slip mode pattern 26
2.4.5 The crystal pattern 28
2.5 Influencing Factors for Deposition Patterns 29
2.5.1 Concentration 29
2.5.2 Size 30
2.5.3 Surfactants 31
2.5.4 Wettability of substrate 32
2.5.5 Substrate temperature 33
2.6 Summary 34
Chapter 3 Properties of Citric Acid modified Magnetic Nanofluids 36
3.1 Introduction 36
3.2 Synthesis of Magnetic Nanofluids 36
3.3 Characterizations of Fe_3O_4 Particles and Clusters 38
3.4 Characterizations of Ferrofluids 43
3.4.1 Density 44
3.4.2 Specific heat capacity 45
3.4.3 Viscosity 47
3.4.4 Thermal conductivity 49
3.4.5 Convective heat transfer 52
3.5 Summary 59
Chapter 4 The Distribution of Droplet Deposition Patterns affected by Thermal Strategies 61
4.1 Introduction 61
4.2 Materials 63
4.3 Experimental Setup 65
4.3.1 Experimental setup for substrate heating temperatures. 66
4.3.2 Experimental setup for local heating 67
4.4 Results and Discussion for Substrate Temperatures 68

4.4.1 The properties of pattern formations with substrate temperatures. 69
4.4.2 Results and discussion for the mechanism of deposition patterns with substrate temperatures 74
4.5 Results and Discussion for the Local Heating. 85
4.5.1 The properties of pattern formations for the local heating 85
4.5.2 Results and analysis for the local heating..... 88
4.6 Summary 92
Chapter 5 Conclusions and Further Work 94
5.1 Properties of CA modified MNFs 94
5.2 Droplet Deposition Patterns affected by Thermal Strategies 96
Reference 98
Appendix..... 118

List of Figures

Figure 1. 1 Different fields on addressing droplet evaporation issues. [40] 5

*Figure 2. 1 Viscosity with concentrations for spherical particle nanofluids. [67]*17

Figure 2. 2 The effect of thermal conductivity on aggregation. [17] 18

Figure 2. 3 Methods to address droplet wetting and evaporation. [40]..... 20

Figure 2. 4 Conceptual diagram of the contact line. 21

Figure 2. 5 Constant contact radius and constant contact angle. [125] 22

Figure 2. 6 Coffee ring stain left after the drying of a coffee drop following the CCR mode. [39] 24

Figure 2. 7 Evaporation of a colloidal drop under standard ambient conditions: (a) outward flow in a droplet creates a coffee-ring stain; (b) recirculating the Marangoni flow creates a uniform pattern. [130] 25

Figure 2. 8 Evaporation of a droplet on a hydrophobic surface in the CCA mode leads to the dot-like pattern. [134] 26

Figure 2. 9 (a) Stick-slip pattern. (b) Contact radius and contact angle versus evaporation time. [135] 27

Figure 2. 10 Lifetime of a saline droplet containing 10% salt: (a) side view and (b) top view. Scale bar, 1 mm. [119] 29

Figure 2. 11 Influence of nanoparticle concentration on final deposition patterns. A coffee-ring pattern is formed between 0.01 and 0.47 wt.%, and a flower petal pattern is formed between 1.15 and 5.70 wt.%. [50] 30

Figure 2. 12 (a) Separation of particles with different sizes (2 μm (blue), 1 μm (red), 40 nm (green)) after complete evaporation. (b) Separation of B-lymphoma cells (red), Escherichia coli (green), and antimouse IgG antibodies (blue). [150]..... 31

Figure 2. 13 (a) A coffee-ring pattern was formed without biosurfactants. (b) A uniform pattern was formed with biosurfactants due to the Marangoni flow. [151] 32

Figure 2. 14 Deposition patterns of polymer particles on substrates with different contact angle hysteresis (CAH): (a) strong CAH, (b) weak CAH. [153] 33

Figure 2. 15 The surface profile of poly (ethylene oxide) film: (a) isothermal evaporation process; (b) non-isothermal evaporation process. [156] 34

Figure 3. 1 TEM Image and Size Distribution of Fe_3O_4 nanofluids. 39

Figure 3. 2 TEM image of citric acid modified Fe_3O_4 particle sample. 39

Figure 3. 3 XRD characterization of modified Fe_3O_4 nanoparticles. 40

Figure 3. 4 Weight fraction of citric acid by TGA measurement. 41

Figure 3. 5 (a) the relationship between Zeta-potential and pH values. (b) relationship between hydrodynamic diameter and pH values of CA coated Fe_3O_4 particles dispersed in the base liquid. 42

Figure 3. 6 Comparison of colloidal stability (a) and foaming (b) of naked and modified Fe_3O_4. 43

Figure 3. 7 Density of CA modified MNFs as a function of the particle concentration. 45

Figure 3. 8 Specific heat capacity of CA modified Fe_3O_4 nanofluids against particle concentration. 47

Figure 3. 9 (a) Viscosity as a function of shear rate for CA modified Fe_3O_4 nanofluids at different pH values. (b) Decrease of the viscosity at each pH. 48

Figure 3. 10 Viscosity of CA modified Fe_3O_4 nanofluids against particle concentration with different temperatures. 49

Figure 3. 11 Thermal conductivity of CA modified Fe_3O_4 nanofluids against the temperature at different particle concentrations. 50

Figure 3. 12 Comparison of experimental data and the Maxwell model in thermal conductivity. 52

Figure 3. 13 The experimental schematics for the convective heat transfer. 53

Figure 3. 14 Experimental setup for the measurement of heat transfer coefficient of nanofluids. 54

Figure 3. 15 Comparison between the experimental data of water with the ones calculated by the Dittus-Boelter equation. 57

Figure 3. 16 Convective heat transfer coefficients of the base liquid and MNFs as a function of the Reynold number. 59

Figure 4. 1 Contact angle of the hydrophobic surface coated by PDMS-SiO_2. ... 64

Figure 4. 2 Contact angle of the hydrophilic surface coated by magnetic nanofluids. 65

Figure 4. 3 Schematic set-up for controlling deposition patterns through substrate temperature. 67

Figure 4. 4 Schematic set-up for deposition patterns of the saline droplet with both the local and the substrate heating on different wettability. 68

Figure 4. 5 Evaporation process of saline deposition patterns at temperatures (10 °C, 15 °C, 20 °C). 70

Figure 4. 6 Evaporation process of MNFs deposition patterns at the low temperature range (10 °C, 15 °C, 20 °C). 71

Figure 4. 7 Evaporation process of saline deposition patterns at 25 °C. 71

Figure 4. 8 Evaporation process of MNFs deposition patterns at 25 °C. 72

Figure 4. 9 Evaporation process of saline deposition patterns at the high-temperature range (40 °C, 55 °C, 70 °C). 73

Figure 4. 10 Evaporation process of MNFs deposition patterns at the high-temperature range (40 °C, 55 °C, 70 °C). 74

Figure 4. 11 Microbeads travel to the boundary along the air-liquid interface at the low temperature range. 75

Figure 4. 12 Microbeads tracked at the central area at the early stage. 76

Figure 4. 13 Red marked microbead travel back from the edge along air-liquid interface at the middle stage. 77

Figure 4. 14 Microbeads trajectories at the end of the evaporation. 77

Figure 4. 15 Surface temperature distributions at the low-temperature range.... 78

Figure 4. 16 Microbeads movement directions at 25 °C. 80

Figure 4. 17 Particles motion distribution at 25 °C. 80

Figure 4. 18 Microbeads movement direction trends at the final stage at 25 °C.. 81

Figure 4. 19 Surface temperature distributions at 25 °C. 81

Figure 4. 20 Microbeads movement recording at the early stage of 55 °C...... 82

Figure 4. 21 Microbeads movement direction tracking at the middle stage of 55 °C. 83

Figure 4. 22 Microbeads movement trajectory at the final stage of 55 °C. 83

Figure 4. 23 Final pattern distribution of microbeads at 55 °C...... 84

Figure 4. 24 Surface temperature distributions at the high-temperature range. . 85

Figure 4. 25 Evaporation process from the substrate heating to the localized heating on the hydrophilic and the hydrophobic surfaces. (a) 2μL saline droplet heated from the substrate (hydrophilic surface). (b) 2μL saline droplet heated from

the apex (hydrophilic surface). (c) 2μL saline droplet heated from substrate (hydrophobic surface). (d) 2μL saline droplet process heated from apex (hydrophilic surface). 86

Figure 4. 26 Substrate and local heating of saline deposition patterns on the hydrophilic surface. 87

Figure 4. 27 Substrate and local heating of saline deposition patterns on the hydrophobic surface. 88

Figure 4. 28 Surface temperature distribution profiles of the substrate heating at 25 °C. 89

Figure 4. 29 Schematic diagrams for the mechanism of the coffee ring effect and reversing internal flow by the localized heating. 90

List of Tables

Table 1 Experimental equipment of characterizations. 38

Table 2 Experimental equipment of thermal physical properties. 43

Table 3 The detailed specifications of the convective heat transfer. 53

Table 4 The detailed specifications for deposition patterns. 65

Table 5 Parameters of the parabolic trough and test conditions 119

Chapter 1 Introduction

1.1 General Background

With the continuous development of engineering applications, such as automotive cooling system, solar energy and micro-electronics, higher requirements are placed in the heat transfer performance. However, most applications utilize conventional fluids, like water, ethylene glycol and heat transfer oil, as working media. Such conventional cooling media cannot reach heat transfer performances in the latest compact engineering applications due to their relatively limited heat transfer properties.

Over the past decades, researchers have shown great interests in suspending nano-size particles into the conventional fluid to improve heat transfer performance. The term 'nanofluid', is a nano-size suspension, and particles (1-100 nm) are typically made of metal, metal oxide and semi-conductor. Nanofluids were first experimentally proposed by Choi in 1995 [1]. Generally, conventional heat transfer liquids, including oil, water, and ethylene glycol mixture, are used as the base liquids to disperse particles and make the suspension flowable. Due to enhanced properties compared to millimetre and micrometre sized particles, nanofluids exhibit the great potential in different engineering applications.

Compared to conventional nanofluids, magnetic nanofluids (MNFs), also called ferrofluids, were first discovered in the 1960s, when scientists of NASA Research Centre were sorting out liquid manipulation in space. MNFs are superior to other nanofluids since they possess both the magnetic property and the flowability. Such distinctive characteristics enable the control of the particle movement, particle

dispersion and fluidity through magnetic forces. With the absence of external magnetic fields, superparamagnetic nanoparticles (SMNP) behave as non-magnetic ones. However, the physical properties of magnetic nanofluids are changed with an applied magnetic field. It is possible to control thermal physical properties of MNFs by adjusting both the intensity and the orientation of the magnetic field [2, 3]. Field dependent thermal conductivity [4, 5] and magnetoviscous effect [6] have been reported by many studies. Specific heat capacity of MNFs is related to the field of the magnetic intensity [7]. Moreover, when the temperature and the magnetic gradient co-exist, MNFs can generate another new convection loop that is more intensive than the gravitational one. This convection is called thermomagnetic convection, which is exclusive to MNFs. It has been suggested that a solution for the micro-sized cooling is considered [2]. Most importantly, the convective heat transfer of MNFs is further improved by magnetic forces. Some reports [8, 9] show that the local Nusselt number is increased by 300% when a constant magnetic gradient is applied.

Although characteristics of magnetic nanofluids show greater potential in various thermal applications, the preparation and the stability are two important prerequisites. In the process of the preparation, the cluster is the key issue. Both the strong magnetostatic attraction force among particles and magnetic saturation with magnetic fields impede ferrofluids in practical engineering applications. To overcome the aggregation, the diameter of the colloidal suspension should be approximately within 10 nm [10]. Meanwhile, it is valid to treat modifications on the magnetic particle surface to remain stable.

In addition, when nanofluids are considered for thermal applications, one of the biggest challenges is how to ensure the colloidal stability of particles in the base liquid. Poor colloidal stability will lead to particle aggregations even precipitations. Large precipitates of particles will result in corrosion of components, clogging of flow channels and pressure drop. Furthermore, it is found that uncontrolled particle aggregations lead to unpredictable thermal physical properties [11, 12]. To explain the relationship between particle aggregations and thermal conductivity, there are two main theories dominating thermal conductivity enhancement of nanofluids, containing Kapitsa resistance at the nanoparticle fluid interface [13] and the thermal percolation paths formed by particle aggregations [14]. The latter could be explained by faster heat transfer along a solid structure than through a liquid. In particular, the "chain up" of SMNPs driven by the magnetic field can supply a "highway" for heat transfer when the field is collinear with the temperature gradient [15, 16]. However, once the scale of the aggregation is beyond a critical level, it will decrease thermal conductivity [17] because the major part of the fluid is empty of particles. If particles undergo uncontrolled aggregations, no theory is useful to predict the thermal conductivity.

Moreover, aggregations may change nanofluids to non-Newtonian fluids [18, 19], regardless of whether the particles are magnetic or not. Many researchers reported shear thinning of nanofluids. In their studies, they found that the viscosity decreased with the increase of shear rate during rheological measurements [18, 20-26]. Zhou et al. [21] made a hypothesis that the decrease of the viscosity under shear results from broken particle aggregates. Several studies showed that the anomalous

viscosity had to do with particle aggregations [18, 22]. If uncontrolled aggregations occurred, no models would be effective to estimate the viscosity of nanofluids.

There are two most used approaches to improve particle dispersions in the engineering field, including the ultrasonic treatment and modifying surfactants. Vigorous ultrasonic vibration can break large aggregates. Although the short-term stability can be achieved after ultrasonic treatment, aggregations will be still inevitable as long as colloidal stability is poor. Colloidal stability depends on either the steric effect or electrostatic repulsion [27]. The former stabilizes a particle by coating it with a large molecule so that particles cannot get too close to each other. The mechanism of the later one is because of the electric repulsive force that arises among the charges of the particles with the same sign. Surfactants stabilize particles by enhancing one or both of them, depending on the molecular size of the surfactant and its type. Surfactants stay at the surface of the particle by the physical absorption. To favour the absorption kinetic, there must be a large number of free surfactants dispersed in the liquid phase. However, these free surfactants produce foams during the heating and the pumping. Moreover, adding solvents of the low polarity (i.e. anti-freezer ethylene glycol) will trigger the desorption of surfactants [28], making the colloidal stability worse. Therefore, stable and surfactant-free nanofluids with predicable thermal physical properties should be much more promising for heat transfer enhancement.

The other aim of this work is to control the distribution of various deposition patterns without additional chemicals. Both liquid drops and droplets are ubiquitous, which have attracted the attention of many researchers. Technically, a drop can be defined as a small (millimetric or smaller) volume of the liquid, which is bound by

interfaces with other fluids or solids. In our daily life, droplets encounter a solid surface, which is defined as the sessile drop. It can be not only observed in nature, such as spilled coffee on the desk, rain droplets on the lotus, but also be applied on different industrial and practical applications, like pharmaceutical purification [29], salt manufacturing [30], inkjet printing [31-33], DNA microarrays [34, 35], Nanotechnology [36-38] and so on.

In 1997, Robert D Deegan [39] firstly proposed the coffee ring effect, which sparked researchers' interests in different fields as shown in Figure 1.1. Chemists are concerned with the wetting issue, colloid motions and their influence on spreading and evaporation; in mechanical engineers' view, the problem of the droplet evaporation should be solved by investigating internal flow motion and the vapour flow behaviour around the evaporating droplet; while in terms of physics, surface tension and evaporation dynamics are involved as solutions.

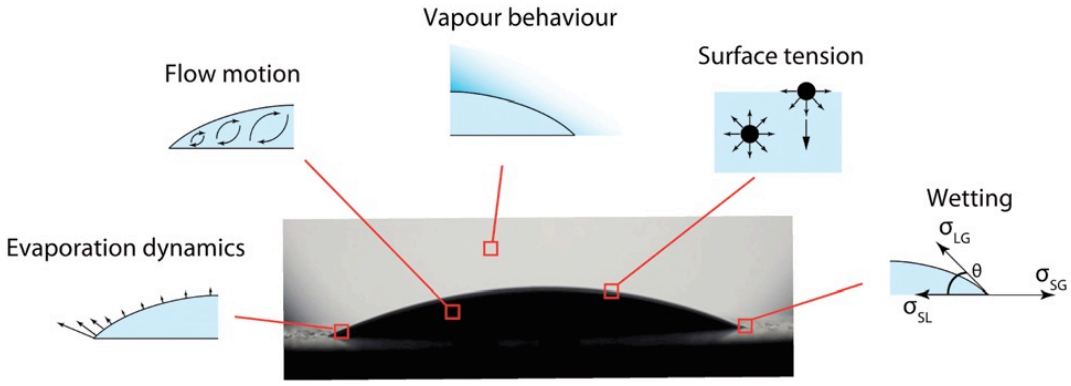


Figure 1. 1 Different fields on addressing droplet evaporation issues. [40]

In addition, due to dramatically increasing demands in industrial and practical applications, such as inkjet [31, 41], polymer coating, micro/nanotechnology, biomedical analysis and diagnosis, deposition patterns have attracted many

attentions, which have encouraged many scholars to make great contributions in understanding pattern formations.

For biomedical analysis, David Brutin et al. [42] proposed the final formations of the whole blood drop evaporation, which formed regular deposition patterns with a good reproducibility for a healthy person. Meanwhile, dried blood patterns on anaemic and hyperlipidaemia diseases were also investigated, which exhibited more concentrated near the contact line comparing that of healthy patterns. The mechanisms behind final blood patterns were presented and explained in the conjunction with the principles of haematology. In their study, they found that the evaporation process of the blood drop was driven by the Marangoni flow.

For inkjet printing, Allon S. et al. [43] investigated the effect of the coffee ring phenomenon of the inkjet printing of flexible high-performance carbon nanotube transparent conductive films. In their research, they found that the pattern dimensions could be controlled by the temperature, which was a practical solution for selecting patterns. Meanwhile, the ring-like structure contributed to the higher transparency, which enabled overlapped layers still with excellent transparency in the practical application.

In 2018, Huang et al. [44] pre-concentrated the protein solution by the coffee-ring drying pattern, prior to Raman analysis in Drop Coating Deposition Raman (DCDR) technique that was used in the field of biomedical science. In their research, Raman Spectra acquired from the ring-like deposits exhibited great enhancement owing to the presence of the silver nano-film, which offered a complementary low-cost method for the preparation of the protein.

In practical applications, the ‘coffee ring’ effect should be firstly illustrated to understand the formation of deposition patterns. Drops sometimes accidentally spill out and exhibit ring-like deposition patterns on the substrate after complete evaporation. Such phenomenon is called the coffee ring effect, which was first proposed by Robert D Deegan et al. [39]. Nearly all the droplets eventually form a ring-structure stain during the process of the natural evaporation whether it is expected or not. Therefore, researchers have made great efforts to control the distribution of deposition patterns by studying the factors influencing the formation of sedimentary patterns over the past decades [40, 45-47].

B Rajneesh et al. [48] tried to study how the distributions of the nanofluids formations were affected by the Van der Waals force. In their research, they investigated deposited patterns for water glass Titanium system. The diameter and volume concentration of the particles were 25 nm, 2% with different pH values of 11.7, 5.8 and 2.8 respectively. In this way, the number of neutralized electrons was controlled by adjusting pH values, which affected the number of interacting particles in the droplet. When pH value reached 5.8, the internal particles were balanced by the Van der Waals force, which made the sediment particles evenly distributed.

Surfactant is another significant influencing factor that affects drying patterns. In 2016, Kim et al. [49] described influencing parameters for uniform patterns coating of binary solutions. They studied the effects of surfactants driven by the Marangoni flow and surface-adsorbed materials in the binary mixture on the final deposit. They found an optimal formulation ratio.

After that, in 2018, David Brutin et al. [50] studied the relationship between concentrations and deposition patterns. In the experiment, nanofluid concentrations, ranging from 0.01% to 5.70%, were experimentally conducted. The results showed that there was a critical concentration point for different pattern formations. The typical ring-like structure was formed when the nanofluid concentration is less than 0.47%. However, the petal shape pattern was performed when the concentration was up to 1.15%. The number of petals of the flower pattern increased with the increasing concentration, which provided a potential attempt for the deposition pattern.

1.2 Research Objectives

There are two main aims of the present work. The first aim is to investigate influencing factors that affect the stability of nanoparticles in MNFs. Meanwhile, with well-dispersed MNFs, thermal properties are also comprehensively studied, including density, specific heat capacity, viscosity, thermal conductivity and convective heat transfer.

The other aim is to explore an effective method that enables the distribution of droplet drying patterns without chemicals. This is because most industrial productions have very demanding requirements, which are difficult to adjust the pattern distribution by changing properties of the droplet to achieve strict requirements. The present work aims to explore effective thermal strategies to control the distribution of deposition patterns without chemicals. To achieve these two aims, the objectives are as follows,

- Synthesis of highly stable magnetic nanofluids. On one hand, effective modifications/surfactants need to be investigated to make the magnetic nanoparticles more stable. On the other hand, to optimise the stability, the relationship between the stability of MNFs and influencing factors also needs to be studied.
- Study on thermal properties of prepared MNFs, which includes thermal physical properties (density, heat capacity and viscosity) and heat transfer properties (thermal conductivity and convective heat transfer).
- Experimentally investigate the relationship between the distributions of pattern formations (including saline and MNFs droplets) and substrate temperatures, ranging from cooling to heating temperatures, and explore the mechanism behind different pattern formations.
- Experimentally investigate the effect of the heating direction (the uniform heating and the local heating) on the distribution of pattern formations and explore the mechanism behind different pattern formations.

1.3 Outline of the Work

The project aims not only to comprehensively analyse the thermal properties of well-prepared MNFs, but also to explore thermal methods to control the distribution of deposition patterns without adjusting chemicals inside solutions. The main works are outlined and presented as follows.

- Chapter 2 reviews the background and the relevant theories of both nanofluids and droplet deposition patterns. For nanofluids, they include different techniques for preparation of ferrofluids, influencing factors of the stability and previous works in thermal properties of ferrofluids. For droplet

deposition patterns, the history and relevant theories are reviewed. Besides, typical deposition patterns are introduced based on previous works. Various influencing factors, including droplet properties, environmental conditions, and fluid compositions, are also comprehensively reviewed.

- In Chapter 3, the magnetic nanofluids are firstly modified citric acid by the co-precipitation method. Characterizations of nanofluids are then comprehensively analysed to explore effective factors for optimizing the stability of MNFs. In addition, thermal properties are also investigated.
- In Chapter 4, deposition patterns of both saline and MNFs are experimentally investigated by thermal strategies, including substrate temperatures and the local heating.
- Chapter 5 presents the conclusions of the present research and recommendations for future work.

Chapter 2 Literature Review for Characters of Magnetic Nanofluids (MNFs) and Recent Advances in Droplet Evaporation

Firstly, this chapter reviews synthesis technology and thermal properties of MNFs. Then, relevant concepts and theories are then introduced for droplet deposition patterns. Meanwhile, typical drying formations and influencing factors are also reviewed based on previous work.

2.1 Synthesis of Magnetic Nanofluids

The synthesis is a significant prerequisite for the properties of ferrofluids. Generally, MNFs are synthesised by dispersing nano-size magnetic particles (Fe_3O_4, γ-Fe_2O_3, Fe, Co, etc.) into carrier fluids (water, ethylene glycol, etc.) [51]. The synthesis can be classified into the one-step method and the two-step method.

The one-step method is a combination of the production of nanoparticles with the synthesis of nanofluids simultaneously. Akon et al. [52] developed a single-step direct evaporation approach (Vacuum Evaporation onto a Running Oil Substrate technology) for the preparation of oil-based ferrofluids. Another one-step approach is the laser ablation approach, which generates nanofluids by irradiating with laser light [53, 54]. Even though the one-step method makes the quality purer and more homogeneous, the quantity is very limited, which hinders the process of the industrial production of nanofluids.

For the two-step method, particles are first prepared, and then dispersed into the base liquid. Among different procedures [55-59], the co-precipitation is the most-used method, which modifies iron oxide nanoparticles (Fe_3O_4, γ-Fe_2O_3) by the simultaneous precipitation of Fe^{3+} and Fe^{2+} ions in basic aqueous media. Once the configuration ratio is fixed, the quality of nanoparticles can be fully reproducible.

Sundar et al. [60] dispersed Fe_3O_4 particles prepared by the co-precipitation method into ethylene glycol and water mixture directly, and MNFs kept stable up to 80 days. In addition, the surface of the particles is clean, and the cost is relatively cheap. The iron atoms on the surface can bind several kinds of chemical groups (i.e. carboxyl [61-63], silane [64] and phosphate [65]) through the formation of coordination bonds, which is beneficial for further surface modification. However, the reaction is too fast to be controlled, so the prepared particles are usually polydisperse in their shapes and sizes. It is possible to control the average size of the particle by adding the stabilizer, like citrate [56], to the reaction system.

It is known that MNPs have a great tendency to accumulate in the solution due to the Van der Waals attractive force [27]. In the engineering field, the ultrasonic treatment is often used for breaking large aggregates [66, 67]. However, aggregations will not be under control if no measure is carried out to enhance colloidal stability. Usually, steric stabilization and electrostatic stabilization [27] are efficient methods to stabilize particles.

The first method coats particles with the sufficiently large molecule and stabilizes particles by the “steric effect”. The steric effect arises from a fact that each atom within a molecule occupies a certain amount of space. When particles are trying to merge with each other, atoms will be too close, leading to an increase in energy. The increased energy will generate a repulsive force to stop the merging process. Steric stabilization should be the only option to stabilize particles in the oil since it is impossible for particles to carry charges in the oil. The oleic acid is the most used surface activator to stabilize particles in the oil [68, 69].

Electrostatic stabilization is based on the electric repulsive force arising due to two particles possessing charges with the same sign. According to the classical DLVO theory [70, 71], particles carrying charges do not undergo aggregations when electric repulsive force is stronger than the Van der Waals attractive force. To achieve electrostatic stabilization, it can be chemically attached to the surface of the particle via the formation of the coordination bond between the metal atom and the carboxyl group, leaving one or two carboxyl groups into the surrounding liquid phase [61]. These free carboxyl groups are expected to dissociate in the water, generating negatively charged group COO- on the surface of particles. With the increasing pH of the particle suspension, more COO- groups will be generated on the surface of particles, resulting in an enhancement of the surface potential [61-63]. Therefore, the strength of the aggregation of CA modified particles can be controlled by changing pH values [61].

2.2 Thermal Properties of Magnetic Nanofluids

2.2.1 Density

Density is a factor affecting Reynolds number, the pressure loss and Nusselt number of nanofluids. Mostly, the density of particles is larger than that of the base liquid. The density of nanofluids is proportional to the volume fraction of particles and linearly increases with the particle concentration. Usually, the density is reported with the mixing theory [72],

$$\rho_{nf} = (1 - \phi)\rho_{bl} + \phi\rho_s \tag{2.1}$$

where ρ_{nf} refers to the density of nanofluids, ϕ is the volume fraction of particles, ρ_{bl} is the density of the base liquid and ρ_s is the density of particles.

Besides the particle concentration, the density of nanofluids is also dependent on the temperature [73, 74] and the pressure [75]. After the investigation of density of alumina nanofluids, antimony-tin oxide or zinc oxide particles, Vajjha et al. [74] decided to attribute the effect of the temperature to the change of ρ_{bl}, assuming that ρ_s kept constant. In this way, equation (2.1) will be still valid as long as ρ_{bl} keeps at a certain temperature.

2.2.2 Specific heat capacity

Specific heat capacity is required in the measurements of the thermal conductivity [76], thermal diffusivity [77, 78] and the spatial temperature inside the flow [79, 80]. In natural convection, specific heat capacity is a key parameter for describing nanofluids and the convective flow status [81-83]. Differential Scanning Calorimeter (DSC) has been used in measuring the specific heat capacity of nanofluids [84-86]. Evidence has shown that the specific heat capacity is influenced by the particle concentration [87], temperature [88, 89], particle size [90], particle material [91] and the base liquid type [91].

In Pak and Cho's [72] study, they proposed a model showing the relationship between the particle concentration and the specific heat of nanofluids in 1998,

$$C_{p,nf} = \phi C_{p,n} + (1-\phi) C_{p,bl} \tag{2.2}$$

where nf is nanofluid, n is nanoparticle, bl is the base liquid.

In 2000, Xuan and Roetze [92] expressed the following model based on the classical and statistical mechanism [83, 93],

$$C_{p,nf} = \frac{\phi \rho_n C_{p,n} + (1-\phi)\rho_{bl} C_{p,bl}}{\phi \rho_n + (1-\phi)\rho_{bl}} \tag{2.3}$$

where ρ_n and ρ_{bl} are respectively the density of the particle and the base liquid.

Although equation (2.2) is not density-dependent, which is more fitter than equation (2.3) for interpreting ϕ -dependent $C_{p,nf}$ [87]. Meanwhile, several empirical relations are proposed to estimate the effect of the temperature [94-96] without theoretical explanations.

For the effect of the specific heat capacity of MNFs on particle aggregations, Chiu et al. [7] suggested that the specific heat of MNFs was sensitive to the intensity of an external magnetic field. In their study, the specific heat capacity barely changed with the temperature under a weak magnetic field but decreased dramatically with the temperature under a strong field. They attributed this decrease to the reduction in the degrees of freedom of MNPs under magnetic field. In fact, under the magnetic field, MNPs formed the chain-like clusters, which reduced the mobility of particles.

2.2.3 Viscosity

The increasing viscosity of nanofluids can increase thermal conductivity and pumping power. Moreover, the increasing viscosity sometimes makes nanofluids behave like a non-Newtonian fluid [20, 26]. If the strong shear stress destroys particle aggregates, a decrease of the viscosity should be expected [67]. Pastoriza-Gallego et al. [22] observed a peak shown on the profile of loss modulus against strain. They interpreted the peak as that some kinds of structures formed by particles within the fluid were lost during the increase of the strain. Duan et al. [18] found that the shear thinning of alumina nanofluids disappeared after ultrasonically treated. If the shear thinning was related to aggregates being broken under shear, the enhancement of the colloidal stability made viscosity less dependent on shear rate.

For concentration-dependent models, Einstein [97] theoretically studied the viscosity of infinite dilute suspensions of ideally dispersed and non-interacting hard spheres, with the assumption that particles rotated under shear,

$$\mu_r = 1 + 2.5\phi \tag{2.4}$$

where μ_r refers to the ratio of the viscosity of nanofluids to that of base liquids. Einstein model applied to the low volume concentration (ϕ < 1%) [67]. Krieger and Dougherty [98] gave a semi-empirical equation with the relationship between the viscosity and the particle volume fraction of the full range,

$$\mu_r = (1 - \phi/\phi_m)^{-2.5\phi_m} \tag{2.5}$$

where ϕ_m refers to the volume fraction of densely packed particles, ranging from 0.495 to 0.54, and μ_r is approximately 0.605 at the high shear rate. To take aggregations into considerations, Chen et al. [67] modified Krieger and

$$\mu_r = (1 - \phi_a/\phi_m)^{-2.5\phi_m} \tag{2.6}$$

Dougherty's model,

with $$\phi_a = \phi\left(r_a/r_p\right)^{3-d_f} \tag{2.7}$$

where r_a refers to the radius of aggregates, r_p refers to the radius of particles and d_f refers to the fractal dimension of the aggregates, and the fractal dimension is around 1.8 [99]. Equation 2.6 compares the measured data and calculated results (Figure 2.1). They found that the model fitted best when $r_a\ /r_p$ was about 3. When ϕ_a was very small, Prasher et al. [100] suggested that it could perform a binomial expansion to reduce equation 2.6 to a linear relationship,

$$\mu_r = 1 + 2.5\phi_a \tag{2.8}$$

where ϕ_a is the slope and a_a determines how fast the viscosity increases with the particle concentration. When particles inside are ideally dispersed, ϕ_a is equal to ϕ. In other words, Krieger and Dougherty's model is the same as the Einstein model.

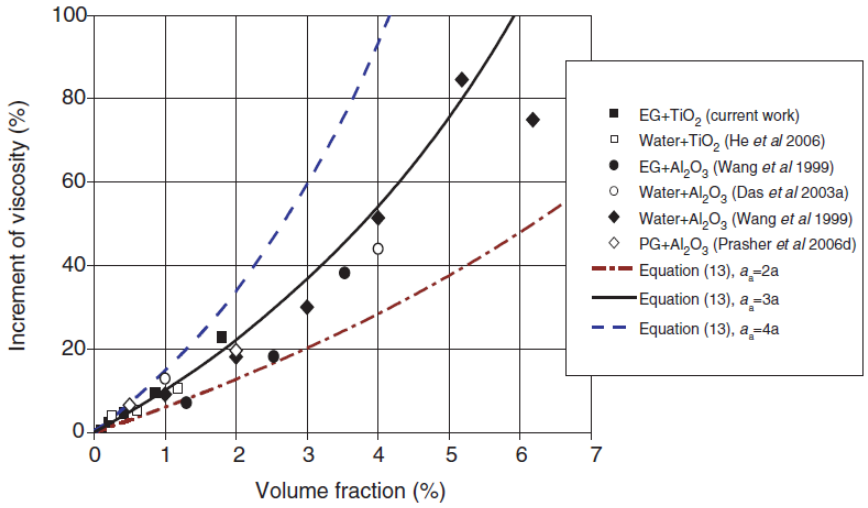


Figure 2. 1 Viscosity with concentrations for spherical particle nanofluids. [67]

2.2.4 Thermal conductivity

Thermal conductivity of MNFs is an attractive feature [101, 102], especially under the magnetic field. However, it is very difficult to predict the amount of the increment by established theoretical models. Most models are derived from the well-known Hamilton-Crosser model [103]. As nanofluids are two-phase fluids, Hamilton–Crosser model is described as solid-liquid mixtures,

$$k_{nf} = k_{bl}\left[\frac{k_p + (n-1)k_{bl} + (n-1)\phi(k_p - k_{bl})}{k_p + (n-1)k_{bl} - \phi(k_p - k_{bl})}\right] \tag{2.9}$$

where subscripts, nf, bl and p, stand for nanofluid, base liquid and particle, n is the empirical shape factor. When the value of n is 3, it is the Maxwell model, which is for spherical particles with low volume concentrations [104].

$$k_{nf} = k_{bl}\left[\frac{k_p + 2k_{bl} + 2\phi(k_p - k_{bl})}{k_p + 2k_{bl} - \phi(k_p - k_{bl})}\right] \tag{2.10}$$

However, researchers also use empirical equations. Tawfik et al. [105] summarized seven parameters affecting thermal conductivity of nanofluids, which were particle's concentration, size, shape, thermal conductivity, base liquid type, temperature and preparation method. The first six ones had been discussed by the reported models [76, 106, 107]. The preparation method determined the stability of the particle dispersion. It was widely accepted that heat transfer should be faster along the structure of aggregates than through the body of the base liquid. On the other hand, Prasher [99] reported that there should be an optimal scale of the aggregation for thermal conductivity (Figure 2.2). Fully aggregated and dispersed nanofluids should generate the thermal conductivity compared to the value predicted by the Maxwell model. If particles underwent uncontrolled aggregations, it was impossible to predict the thermal conductivity of nanofluids.

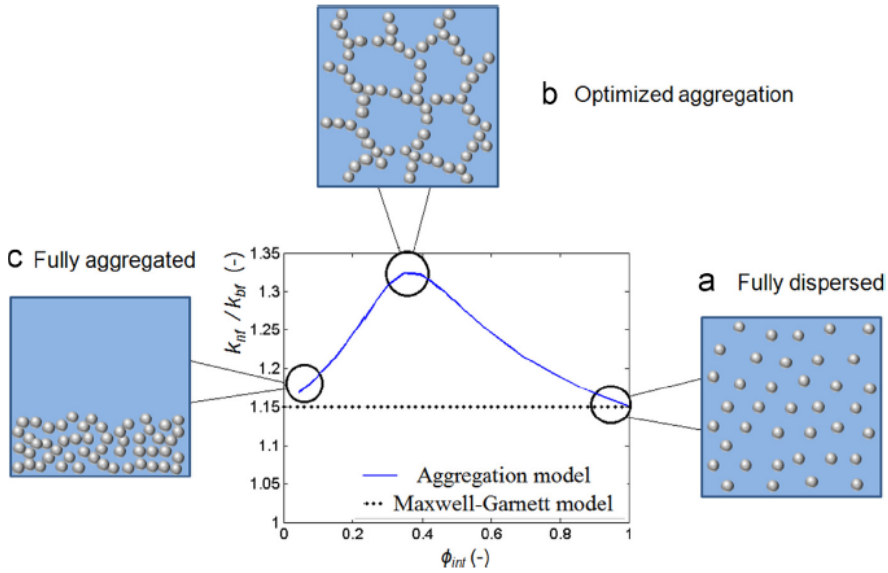


Figure 2. 2 The effect of thermal conductivity on aggregation. [17]

2.2.5 Convective heat transfer

In terms of the convective heat transfer, besides concentrations, properties of particles and base liquids [8, 79, 80, 108], the particle migration is another factor

for abnormal heat transfer enhancement [109]. Sohn and Kim [110] confirmed that the particle migration mainly depends on thermophoresis and Brownian diffusion. Bahiraei et al. [111] suggested that particle fluxes due to Brownian diffusion and thermophoresis have orders of 10^{-10} and 10^{-8} respectively. Hence, thermophoresis should contribute to the particle migration. When nanofluids are heated, thermophoresis reduces nanoparticle concentration in the wall boundary layer, leading to a decrease of the viscosity and the increase of velocity near the wall, and thus thinning the boundary layer [112, 113]. By using MRI technology, our group has demonstrated that when MNFs are cooled, the concentration near the wall is higher than that at the centre of pipe [114].

On the other hand, MNFs are inclined to the magnetic gradient. Evidence shows that enhanced heat transfer efficiency exists when the magnetic field is perpendicular to the direction of the flow [115-119]. In addition, Ghofrani et al. [120] and Yarahmadi et al. [121] demonstrated that an alternating magnetic field was better than a constant one and the local heat transfer coefficient increased when the alternating frequency increased. Goharkhah et al. [118] explained that repeating attraction and releasing of nanoparticles brought better mixing and the disturbance of the boundary layer. However, Shahsavar et al. [119] found that increasing the frequency reduced the enhancement of the local Nusselt number, after studying laminar forced convective heat transfer of ferrofluids of MNP-carbon nanotubes composited under alternating magnetic fields. Yarahmadi et al. [121] also showed that the effect of the magnetic field decreased when the Reynolds number increased. When particles suspended in forms of aggregates, the size of aggregates determined how fast the response of the particles to a magnetic field. If the response was very

fast, too many accumulations of particles near the wall decreased the flow velocity in this area, so increasing the frequency would be better; If it was very slow, there might not be enough particles in the boundary layer, thus reducing the frequency should be better. Therefore, the convective heat transfer experiment should be developed based on the MNFs whose colloidal stability was under control.

2.3 Sessile Droplet Evaporation

In 1612, Galileo Galilei [122] first observed that the free surface of water was higher than the solid surface, which prompted him to comment further on spreading and wetting behaviours. Gudris and Kulikowa [123] then investigated on the droplet evaporation in micro-scale. In 1962, Mangel and Baer [124] studied on sessile droplets evaporation on solid surfaces. Since then, researchers have extensively studied the effects of influencing factors on wetting and evaporation of the droplet. According to David Brutin et al.'s [40] research, there were several main studies in the droplet, including mechanical, chemical, material science and so on. Their studies (Figure 2.3) included evaporation dynamics, flow motion, vapour behaviour, surface tension and wetting.

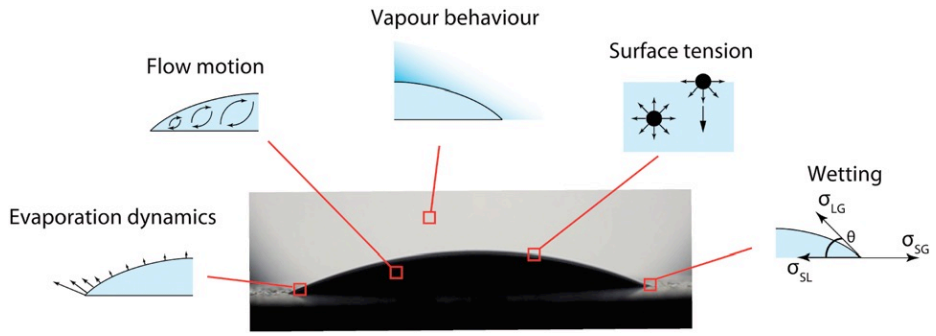


Figure 2. 3 Methods to address droplet wetting and evaporation. [40]

2.3.1 Wettability

In terms of wettability, the relationship can be obtained connecting θ with the system surface and interfacial tensions (Figure 2.4). At equilibrium, the force associated with tension γ_{SV} is balanced by the sum of the forces due to γ_{SL}, the component of γ_{LV} lying in the same plane and direction as γ_{SL}. This component has the magnitude ab and is equal to $\gamma_{LV} \cos \theta$. Thus, equation (2.11) can be written as,

$$\gamma_{SV} = \gamma_{SL} + \gamma_{LV} \cos \theta \tag{2.11}$$

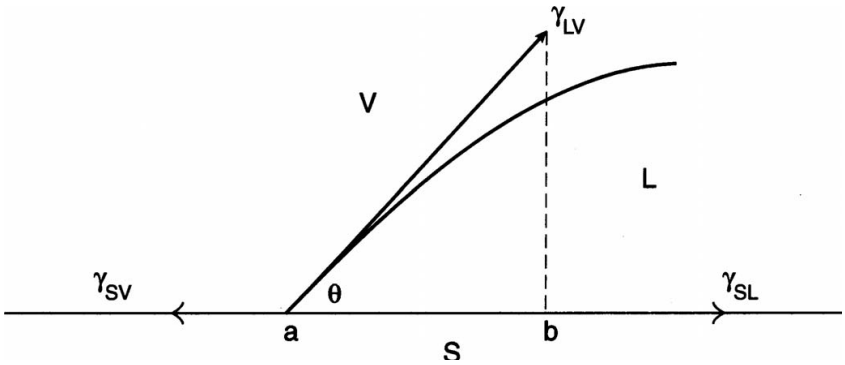


Figure 2. 4 Conceptual diagram of the contact line.

If the liquid wets the solid, the liquid spreads out on the surface, reducing the angle θ<90°; If θ >90°, the liquid does not wet the solid. Figure 2.4 shows that θ will be reduced by a larger value of γ_{SV}, or smaller values of γ_{LV} and γ_{SL}.

2.3.2 Evaporation modes

Droplet evaporation modes can be divided into three modes as follows,

1. The constant contact radius (CCR) mode. The contact line remains pinned, while the contact angle decreases (Figure 2.5), which follows a linear relationship of the volume loss with the evaporation time. The linear evolution also shows that the evaporation rate of the CCR mode is constant, especially when occurring on the roughness substrate.
2. The constant contact angle (CCA) mode, which remains the contact angle fixed with the decrease of the contact radius when droplet evaporates.

Comparing to the CCR mode, the CCA mode exhibits a non-linear decrease of the volume with the evaporation. Based on experimental results, the CCA mode always exhibits on smooth and hydrophobic substrates.

3. The third one is the mixture of two modes, where the process of the evaporation transits from one mode to the other. Moreover, both the contact line and the contact angle decrease simultaneously. Based on experimental reports, the transition mostly happens from the CCR to the CCA mode.

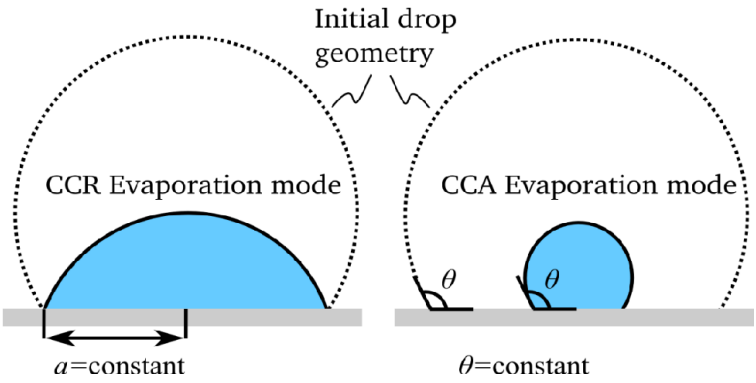


Figure 2. 5 Constant contact radius and constant contact angle. [125]

2.3.3 Flow fields of the drying droplet

There are two main influencing factors in flow fields, the capillary flow and the Marangoni flow, affecting the distribution of droplet deposition patterns.

For the capillary flow, based on Deegan's [39] investigation, the highest evaporation rate is near the contact line. The contact line is pinned, solvents transport radially from the central region to the edge to replenish the evaporated liquid. The trend of the outward flow is called the capillary flow, which follows the CCR mode.

The Marangoni flow can be manipulated by altering surface tension from the low to the high along the air-liquid interface. Kim et al. [49] studied the effects of substrate temperatures on the Marangoni flow in water with polymers. When the

substrate is heated isothermally, the evaporative rate at the contact line is the highest, while the rate at the apex is the lowest along the vapour-liquid interface, resulting in an evaporative rate difference. Surfactant is another factor affecting the Marangoni flow. The surfactant locally lowers surface tension and causes a radial outward fluid motion along the interface. Consequently, the drying pattern formation is affected by the surfactant that is induced by the Marangoni flow. Tim still et al. [126] investigated the influence of the sodium dodecyl sulfate (SDS) on the evaporation of drying colloidal droplets. The results showed that additional SDS made the drying pattern uniform. This is because the density difference of SDS leads to a Marangoni eddy. In this way, SDS prevents spheres from reaching the contact line and finally supports the depinning of the contact line.

In addition, the co-occurrence of the capillary and the Marangoni flows inside the droplets is possible when the solvent evaporation causes a thermodynamic and/or hydrodynamic instability. Kim et al. [49] found that the capillary flow was stronger than the Marangoni flow when the substrate was heated, whereas the opposite was true in the case of cooled substrates.

2.4 Typical Drying Patterns

Deposition patterns are ubiquitous in nature and practical applications [19, 127, 128]. Although the ‘coffee ring’ structure is a typical deposition in the evaporation, various conditions make sessile droplet evaporating in different formations. Many studies have focused on how to understand the mechanism behind different deposit patterns and control the morphologies of drying patterns with key parameters. In this section, the most well-known drying patterns are introduced as follows.

2.4.1 The ring-structure pattern

Droplets sometimes accidentally spill out and form a 'ring-like' pattern on the surface after complete evaporation. This phenomenon is called the coffee ring effect (Figure 2.6). In 1997, Deegan et al. [126] firstly proposed the coffee ring effect. They investigated the pattern distribution, flow velocity and growth rate of the ring-like deposits. Based on their reports, the evaporation process was mainly occupied in the CCR mode. The contact line was the highest evaporation flux along the air-liquid interface, which transported solvents from the centre to the edge. Eventually, it formed an outward flow inside the pinned droplet. In this way, more suspended solvents at the central area transported to the boundary, leading to more suspended particles accumulating along the contact line (Figure 2.7a). According to Uno et al.'s [129] study, there were two conditions for the coffee ring effect, the first of which was that the CCR mode occupied the whole evaporation process. The other one was the higher evaporation rate at the contact line. In addition, Hu and Larson [35] proposed that the suppression of the Marangoni flow was the third required factor for the ring-like structure. This was because recirculating the Marangoni flow induced particles deposited to travel back to the central region due to the surface tension gradient.

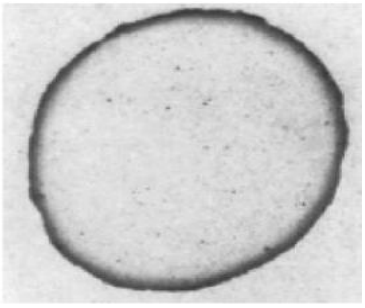


Figure 2. 6 Coffee ring stain left after the drying of a coffee drop following the CCR mode. [39]

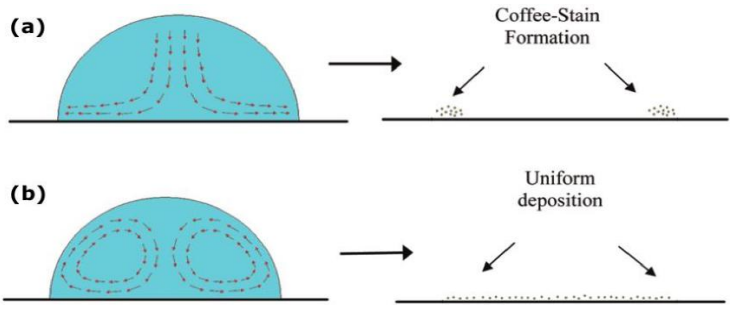


Figure 2. 7 Evaporation of a colloidal drop under standard ambient conditions: (a) outward flow in a droplet creates a coffee-ring stain; (b) recirculating the Marangoni flow creates a uniform pattern. [130]

2.4.2 The uniform deposition pattern

To suppress the ring-like structure and make the formation uniform, the capillary and the Marangoni flows are two main factors that need to be considered. Mostly, the capillary flow dominates the flow field inside the droplet, while the Marangoni effect is always either sufficient suppression or elimination, making the distribution of the formation more uniform. Majumder et al. [130] tried to alter the internal flow by recirculating the Marangoni flow inside the droplet on a hydrophilic substrate. In this way, accumulating particles moved back from the pinned contact line along the air-liquid interface (Figure 2.7b). In their study, the Marangoni flow homogenised the particle concentration and eventually formed a uniform pattern.

Concentration is another important factor in uniform deposition patterns. Typically, the drying pattern forms a ring-like structure with concentration. When the concentration is high enough, the particles will form a uniform distribution which is enclosed by the ring [131, 132].

In addition, pH values also make a great contribution to the uniformity of the deposition pattern due to the DLVO theory. In Bhardwaj et al.'s [48] research, pH values (1.4-11.7) were used to control DLVO forces among colloidal particles. The

results showed that, at a low pH value, the attractive interaction between particles and the substrate dominated the pattern distribution and finally formed a ring-like structure with uniform deposits inside.

2.4.3 The dot-like structure pattern

The dot-like pattern always happens in the constant contact angle mode as shown in Figure 2.8 [133, 134]. Uno et al. [129] investigated the deposition formation of the droplet with constant contact angle mode on the hydrophobic surface. In the process, the shrinking edge prevented outward particles from accumulating at the fixed contact line. With the increasing concentration of particles inside, particles finally aggregated in the central region, forming a dot-like pattern.

In addition, the Marangoni flow also makes a contribution to the dot-like pattern. Thokchom et al. [133] reported that evaporating droplet followed the CCA mode on the hydrophobic surface. In their report, particles were transported from the contact line to the central region along the air-liquid interface by the Marangoni flow. Consequently, the Marangoni flow made the deposit pattern like a dot-like pattern.

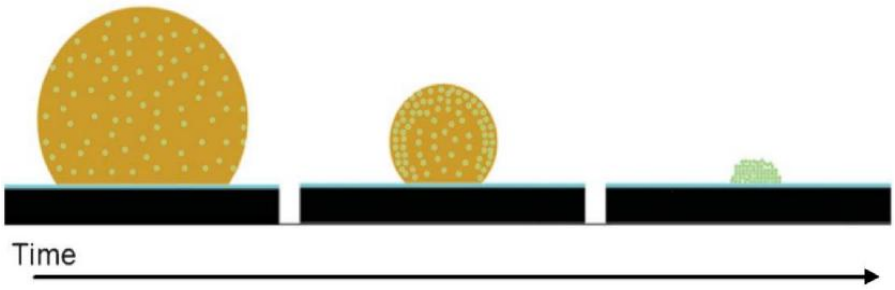


Figure 2. 8 Evaporation of a droplet on a hydrophobic surface in the CCA mode leads to the dot-like pattern. [134]

2.4.4 The stick-slip mode pattern

The mixture of the CCA and the CCR modes is the key parameter for stick-slip mode, leaving a series of concentric rings after complete evaporation (Figure 2.19a)

[135]. The stick-slip pattern is the combination of the ring-like pattern and the dot-like pattern. When the evaporation comes to the CCR mode of combined modes, particles transport outward along the contact line, forming a ring-like pattern. When it comes to the CCA mode, the periphery shrinks inward, which prevents particles to accumulate at the edge and brings particles to the central region. The CCR mode and the CCA mode proceed alternately, and finally form multiple concentric rings. Unexpectedly, droplet profile shows that there is a slight drift of the deposits without sticking along the constant contact lines exactly, which we call it pseudo-pinning (Figure 2.9b) [135-137]. There are two main explanations for pseudo-pinning. Adachi et al. [138] established a numerical model for describing the mechanism of the oscillatory motion of the stick-slip process. In this model, particles travelled from central region to the edge by overcoming the friction force; on the other hand, at the contact line, surface tension and friction force led to the oscillatory motion, consequently, forming a striped stain pattern. The result showed that the stick-slip pattern was the consequence of the balance of both surface tension and the friction force, rather than evaporation modes [38, 138].

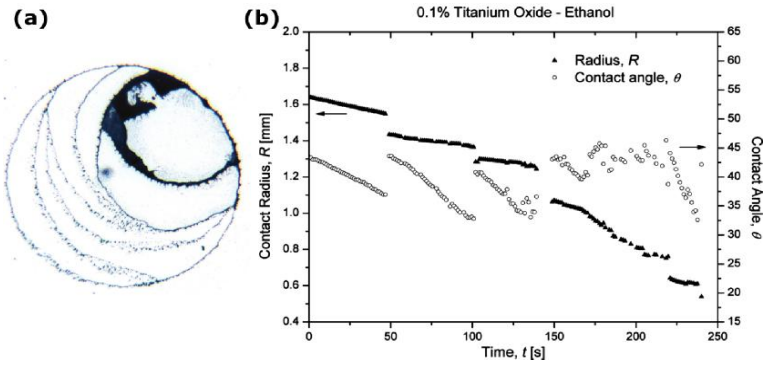


Figure 2. 9 (a) Stick-slip pattern. (b) Contact radius and contact angle versus evaporation time. [135]

2.4.5 The crystal pattern

The crystal patterns are always observed in the interior regions of biological fluids that contain salts [139-141] as shown in Figure 2.10. The combination of the CCR mode and the CCA mode contributes to the formation of the saline crystallisation [142, 143]. Due to the significant applications in medical science, many researchers are interested in crystal patterns. Gorr et al. [142] investigated the deposition patterns of water-based lysozyme protein solutions with saline concentrations. In their report, the capillary flow transported solvents to the contact line at the beginning of the protein separation from the fluids. Then, more salts remained in the droplet and crystallised with constant contact angle, and finally formed a uniform layer of salt crystals in the centre of the dried pattern. For the formation of crystal patterns, some researchers reported that inorganic salts made the main contributions [143, 144], while others believed that the increase of the salt concentration augmented the aggregation of macromolecular proteins, which finally formed crystal patterns [128, 140]. In addition, another explanation for crystal patterns is that these patterns are the salt crystals in the gelled protein matrix, and proteins only have the role of seeds for the salt crystal growth [128, 145]. So far, there is no conclusion for the mechanisms of crystal patterns as it is difficult to distinguish the main components of crystal patterns by analytical techniques [128].

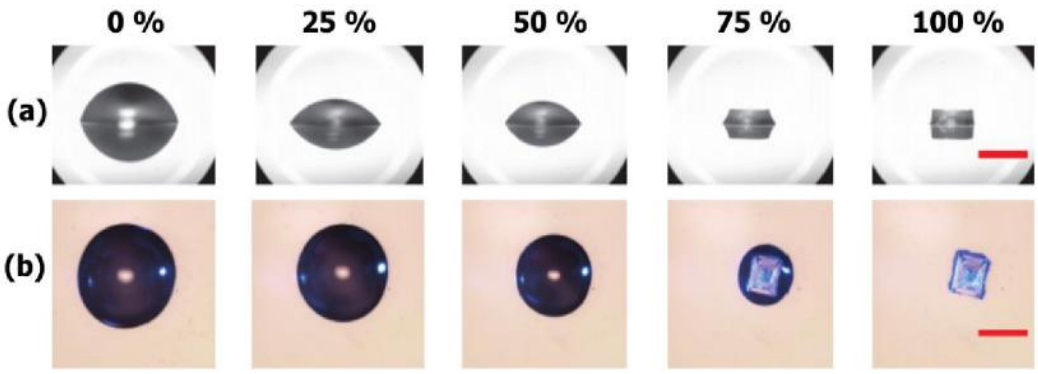


Figure 2. 10 Lifetime of a saline droplet containing 10% salt: (a) side view and (b) top view. Scale bar, 1 mm. [119]

2.5 Influencing Factors for Deposition Patterns

In the previous section, we introduce typical distributions of deposition patterns, and also mention different influencing factors that affect drying patterns, including concentrations, pH values, evaporation modes, etc. Main influencing factors are reviewed in this section.

2.5.1 Concentration

Concentrations can affect the distribution of drying patterns in different aspects. David Brutin et al. [50] studied the effect of concentrations on the shape of deposited patterns. In their research, they reported a transition from an O-ring pattern to a flower pattern by changing concentrations (Figure 2.11). When concentration reached 1.15 wt.%, the deposition pattern formed a petal pattern. When the concentration was over 1.15%, the thickness still increased with the concentration, while the number of flower petals decreased. In addition, Sefiane [146] studied on concentrations of Al_2O_3 nanofluids with 0.1%, 0.5%, 1% and 2% respectively. Although concentrations exhibited ring-like structures, the thickness of the ring-like structure increased with concentrations, and cracking patterns became more prominent at higher concentrations.

Lee et al. [147] combined the concentration and size to investigate the relationship between these factors and their formations. They classified influencing factors into three levels. At the low nanoparticle concentration with small size, deposition patterns formed the coffee-ring structure; moderate concentration and size led to an irregular pattern; when it came to the high concentration and size, the formation tended to be uniform. Sometimes, different concentrations also affect evaporation modes. Moffat et al. [136] studied one kind of nanofluids with 0.01 wt.% and 0.1 wt.%. In their research, when the concentration of nanoparticles was at 0.1 wt.%, evaporation mode changed into stick-slip. Results showed that concentration also had the potential to improve the stick-slip behaviour [136, 137].

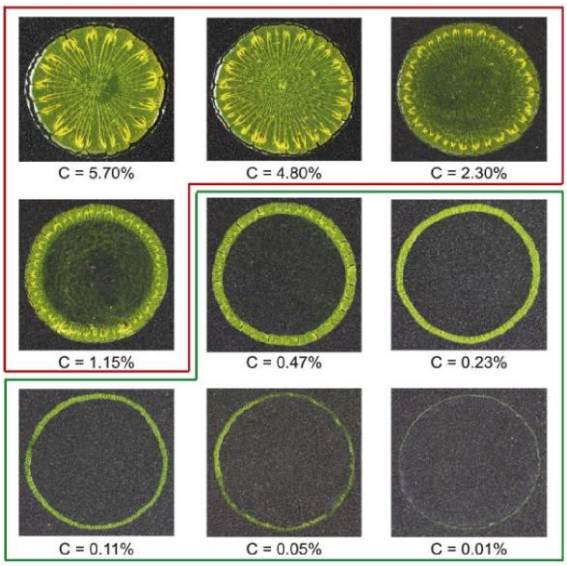


Figure 2. 11 Influence of nanoparticle concentration on final deposition patterns. A coffee-ring pattern is formed between 0.01 and 0.47 wt.%, and a flower petal pattern is formed between 1.15 and 5.70 wt.%. [50]

2.5.2 Size

In terms of the size of particles, Chon et al. [148] investigated the effect of particle sizes (2, 11, 30, and 47 nm) on drying formations. The experimental results showed that particles with large size tended to form ring-like structure patterns, while

smaller size particles formed a uniform pattern with a wider ring. Furthermore, some studies also researched multiple sizes in a single droplet. Jung et al.'s [149] syringed both nanosized and micro-sized particles (500 nm, 5 μm). The results showed that size scales made the particle distribution differently. Nanoparticles accumulated outward to enhance the pinning effect, while microparticles moved towards the central region of the droplet due to surface tension. In addition, Wong et al. [150] also proposed a similar phenomenon with three different sizes in the droplet (Figure 2.12). In their report, three concentric rings were closed to the contact line. The small size particles travelled closest to the contact line, while big size particles formed the innermost ring. This size-dependent effect showed great potential for disease diagnosis.

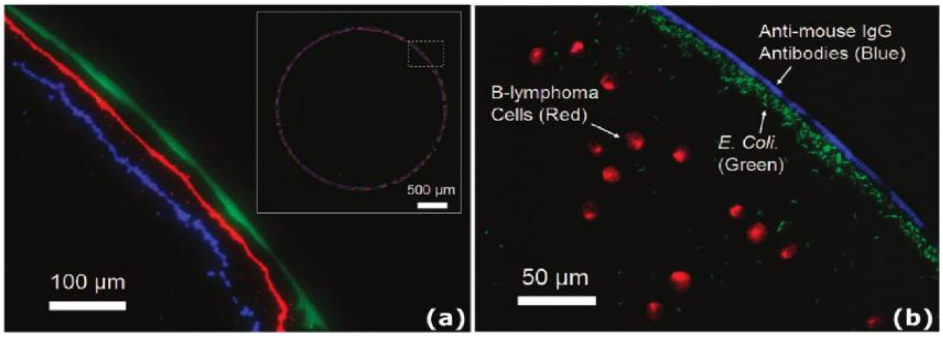


Figure 2. 12 (a) Separation of particles with different sizes (2 μm (blue), 1 μm (red), 40 nm (green)) after complete evaporation. (b) Separation of B-lymphoma cells (red), Escherichia coli (green), and antimouse IgG antibodies (blue). [150]

2.5.3 Surfactants

Surfactant is an important factor that affects the Marangoni flow. Tim Still et al. [126] investigated sodium dodecyl sulfate (SDS) modified solutions. In their study, SDS surfactant induced Marangoni flow along the air-liquid interface, reversing the ring-like structure at the edge and forming a more uniform deposition pattern of colloidal particles. Similarly, Sempels et al. [151] tried biosurfactant to induce the

Marangoni flow. Particles moved towards the droplet edge, but some returned back along the surface interface due to the induced Marangoni flow (Figure 2.13).

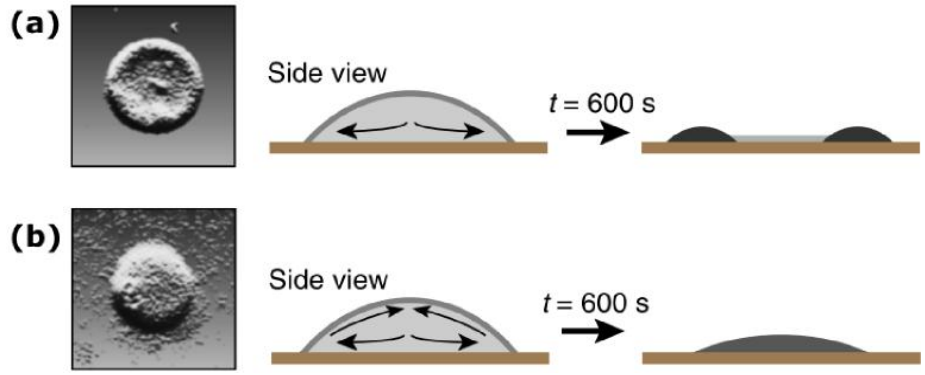


Figure 2. 13 (a) A coffee-ring pattern was formed without biosurfactants. (b) A uniform pattern was formed with biosurfactants due to the Marangoni flow. [151]

2.5.4 Wettability of the substrate

The ring-like structure is often occurred on the hydrophilic surface, while the uniform and the dot-like patterns are formed on the hydrophobic substrate. Nagesh D. Patil et al. [152] compared different kinds of the surface wettability with the non-heated and heated substrate. For the hydrophilic surface, the drying pattern exhibited the ring-like structure, but the ring on the heated one was much thinner than that of the non-heated one. The difference of the thickness might attribute to the Marangoni convection. For the hydrophobic surface, the non-heated substrate showed an inner deposit pattern due to depinning contact line, while on the heated hydrophobic surface, both the heating temperature and the concentration made contributions on the pinned contact line, leading to a thin ring with an inner deposit. Meanwhile, Lee et al. [147] showed the similar results that a lower contact angle was easier for the ring structure pattern, while a high contact angle easily formed patterns at the centre of the peripheral ring. Their explanations were very simple. For a big contact angle, they had a greater height at the centre with a small base

diameter, which led to a central accumulation. When it came to the low contact angle, there was a small height with large base diameter, which increased both the evaporation rate and the flow velocity. The enhancement of these two factors made it easier to form a ring-like deposition pattern.

In addition, Li et al. [153] investigated the distribution of the deposition pattern of polymer particles. In their results, pattern formations were manipulated by the contact angle hysteresis (CAH). Similarly, the ring-like structure was with strong CAH, like poly (vinyl pyrrolidone), and central accumulation was with weak CAH, like sodium polysulfonate (Figure 2.14).

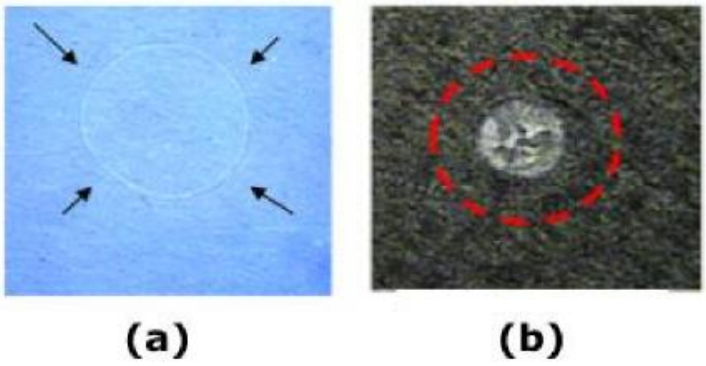


Figure 2. 14 Deposition patterns of polymer particles on substrates with different contact angle hysteresis (CAH): (a) strong CAH, (b) weak CAH. [153]

2.5.5 Substrate temperature

Parsa et al. [154] investigated water-based CuO nanofluids with heating temperatures of 47, 64, 81 and 99 °C respectively. At 47, 64, 81 °C, the dual ring was formed due to the Marangoni effect. At 99°C, there were two counter-rotating vortices at the central area at the early stage of the evaporation process, and there was a complex flow field close to the edge region due to the strong Marangoni flow. At the final stage, the distribution of the deposition pattern exhibited several drying curve lines due to the stick-slip behaviour.

In addition, Kim et al. [155] believed that the flow dynamics of the droplet were affected by the substrate temperature, mainly at the end of the evaporation process. The dried patterns of the water-polymer changed a lot when the substrate temperature was higher than that of the room temperature (Figure 2.15). The droplet formed a typical ring-like pattern on the isothermally heated substrate [156]. In addition, the non-isothermally heated substrate with a rate of 20 °C/min was also conducted and formed a peculiar 'dual-ring' pattern. With the increasing temperature, surface stress increased, while the viscous stress decreased, leading to a contact line recession. On a room temperature substrate, the Marangoni convection of droplets was roughly as strong as the inward Marangoni flow at the central region of the droplets during the evaporation.

On a heating substrate, the outward flow is more intense than the Marangoni flow near the end of the evaporation of droplets. These flow dynamics are responsible for the edge-concentrated deposit patterns after the evaporation of water droplets containing a polymer solute. The inward flow is more intense than the outward flow near the end of the evaporation.

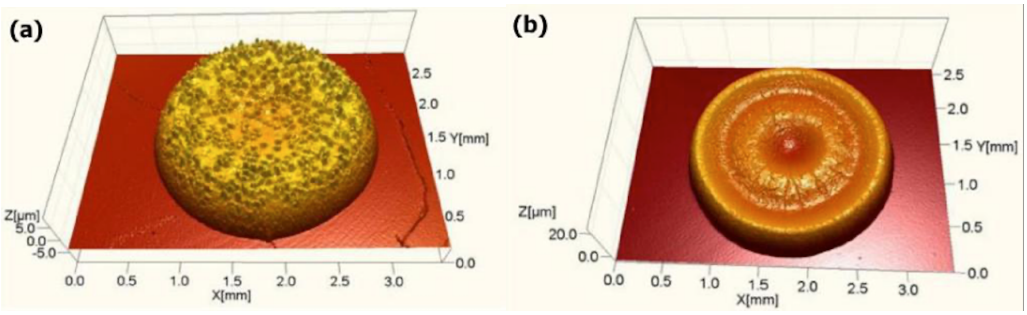


Figure 2. 15 The surface profile of poly (ethylene oxide) film: (a) isothermal evaporation process; (b) non-isothermal evaporation process. [156]

2.6 Summary

In this chapter, to optimise the stability of MNFs, the synthesis of MNFs and related mechanisms are firstly reviewed. There are two synthesis techniques for preparing MNFs, which are the one-step method and two-step method. Extensive studies indicate that the co-precipitation is an efficient method for the preparation of iron oxide based nanofluids. Due to the Van der Waals force, serious agglomerations are formed in MNFs. To overcome aggregation, in addition to ultrasonic treatment, there are two chemical modification methods, namely steric stabilization and electrostatic stabilization, stabilizing nanofluids efficiently.

Thermal properties of MNFs are also reviewed, which include density, specific heat capacity, viscosity, thermal conductivity and convective heat transfer. However, there are two main problems. The first one is the limited applicability of theoretical models to predict the viscosity and thermal conductivity of MNFs. The other one is that it is unclear for the effect of the magnetic field on convective heat transfer enhancement. Evidence shows that particle aggregations associate intimately with its thermal physical properties and convective heat transfer performance, but systematic studies are limited.

For deposition patterns, a brief history and related concepts are introduced. Meanwhile, typical drying pattern formations are reviewed for better understanding of the drying process. Meanwhile, different influencing factors have been reviewed, which include concentration, particle size, wettability, etc. According to our research, the substrate temperature is a potential method to control the deposition patterns without changing chemicals. However, limited studies are conducted in substrate temperatures.

Chapter 3 Properties of Citric Acid modified Magnetic Nanofluids

3.1 Introduction

This chapter aims to prepare stabilised MNFs and study their thermal properties comprehensively. MNFs are firstly prepared by the co-precipitation method, and then citric acid (CA) is modified on the MNPs due to its low cost and operability. In addition, influencing factors, including concentration and pH values, are investigated to optimise the stability of CA modified MNFs.

Density and specific heat capacity are measured with concentrations of 0.23%, 0.46%, 0.69%, 0.92% and 1.15%. Rheological measurements are conducted for the dependence of the viscosity on shear rate with pH values, temperatures and volume fractions. At the neutral pH value, the nanofluid behaves as a Newtonian fluid. Moreover, to avoid the corrosion of cooling systems, the pH value of the coolant needs to be considered carefully, mostly maintaining in the range of 7.5–10.5 [157]. However, increased ionic strength caused by changing pH will worsen the colloidal stability of particles. Therefore, a pH value of 8.5 is selected to investigate the heat transfer properties of prepared MNFs. The thermal conductivity of modified MNFs is promoted due to the proper degree of the stability [104]. For convective heat transfer, a test bench is set up to compare the convective heat transfer of the base liquid and 0.23 vol.% of MNFs.

3.2 Synthesis of Magnetic Nanofluids

Typically, 13.5 g of $FeCl_3 \cdot 6H_2O$ and 6 g of $FeCl_2 \cdot 4H_2O$ are first dissolved in 150 mL deionized water. The solution reacts at the ambient temperature and bubbles with nitrogen for 15 minutes to remove oxygen. 40 mL ammonium hydroxide is

added to the solution under vigorous stirring. And then, the mixture is heated to 60 °C for 1 hour, and the black precipitate is collected at the bottom of the flask by using a magnet and washed with water several times until the pH value reached 7. In the following, 50 g of wet precipitate is dispersed into 200 mL of distilled water with the aid of the ultrasonic treatment. The suspension is then transferred to a three-necked flask equipped with a stirring paddle and nitrogen inlet. After adding oleic acid, the suspension is stirred at 80 °C under the protection of nitrogen for 2 hours. The particles are washed several times with ethanol and hexane until the upper solution becomes transparent. After dumping the supernatant, oleic acid modified Fe_3O_4 particles are obtained. After that, the modified magnetic nanoparticles are added to 200 mL of the water solution with the sodium dodecyl sulfate (25 mg/mL). The mixture is then kept at 80 °C for 2 hours, and a particle–micelle solution then forms. Subsequently, the treated substances are kept at the room temperature for 2 days before experiments.

This synthesis procedure follows the electrostatic stabilization, which relies on the electric repulsive force arising between two particles possessing charges with the same sign. According to the classic DLVO theory [158], particles with charges cannot undergo aggregations when electric repulsive forces are stronger than Van der Waals attractive forces. In this way, the colloidal stability can be achieved by the surface modification. The citric acid (CA), a small molecule with three carboxyl groups, is often used as the surface ligand to stabilize nanoparticles in water [159, 160]. Negatively charged carboxyl groups are attached on the surface of nanoparticles to repel other modified particles. The concentration of electrolytes

will decrease when electrostatic stabilization is applied. Therefore, well-dispersed MNFs are prepared with an average diameter of 10 nm.

3.3 Characterizations of Fe_3O_4 Particles and Clusters

To study the characterizations of MNPs, parameters for the stability of MNPs are discussed in this section. They include transmission electron microscopy (TEM), X-Ray powder diffraction (XRD), thermogravimetric analysis (TGA), zeta-potential measurements and dynamic light scattering (DLS). The detailed specifications are provided in Table 1.

Table 1 Experimental equipment of characterizations.

Model	Specifications
JEOL-2000 electron microscope	Operating voltage: 200 kV Point Image: 0.28 nm Lattice Image: 1.4 nm Specimen Size: 3 mm diameter Tilt angle: Up to 25 ° (with double tilt holder) Cu K-alpha radiation source
Bruker D8 Advance Powder X-ray diffractometer	Theta-theta vertical goniometer Parallel beam optics (primary beam Göbel mirror and secondary beam 0.12 º equatorial Soller slit collimator) Scintillation counter 0D x-ray detector Three exchangeable stages: 9-position sample changer, capillary spinner and controlled temperature/pressure cell with vacuum pumps and gas supply system Sample capacity: 200 mg
TGA-SDTQ600 thermogravimetric analyser	Balance sensitivity: 0.1 μg Calorimetric accuracy: ±2% Temperature range: up to 1300 ºC Heating rate: 80 ºC/min for < 1000 ºC; 20 ºC/min for 1000-1300 ºC Particle size range of 0.3 nm to 10 μm
Malvern Zen 3600 Zetasizer	Temperature range: 0 ° C to 90 ° C Stable temperature range: 15 - 35 °C M3-PALS technology enables accurate measurements of zeta potential in aqueous and non-aqueous dispersions.

The morphology and size of as-prepared particles and clusters are observed by TEM. The samples for TEM observation are prepared via dropping the diluted particle dispersion onto a TEM copper grid. The size distribution is obtained based on at least 300 particles or clusters. MNPs exhibit the spherical shape with the size from 4 nm to 22 nm (Figure 3.1). The average size is approximately 10 nm. Comparing to CA modified MNFs (Figure 3.2), both shape and size do not change very much.

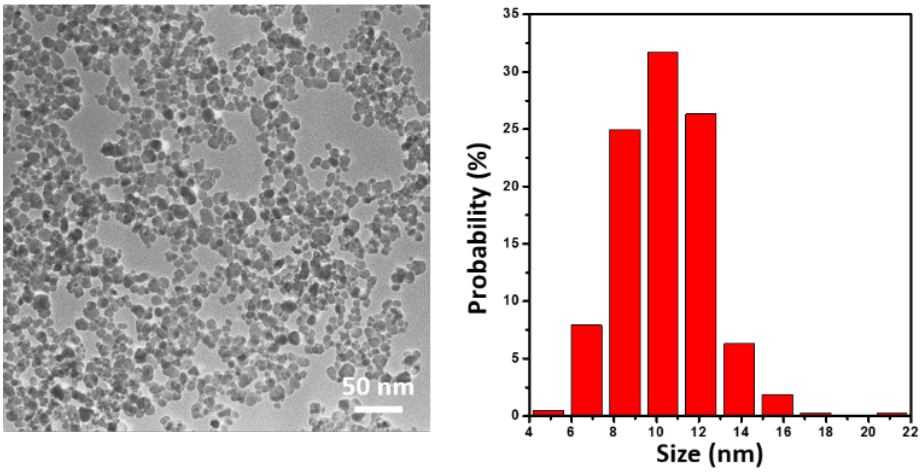


Figure 3. 1 TEM Image and Size Distribution of Fe_3O_4 nanofluids.

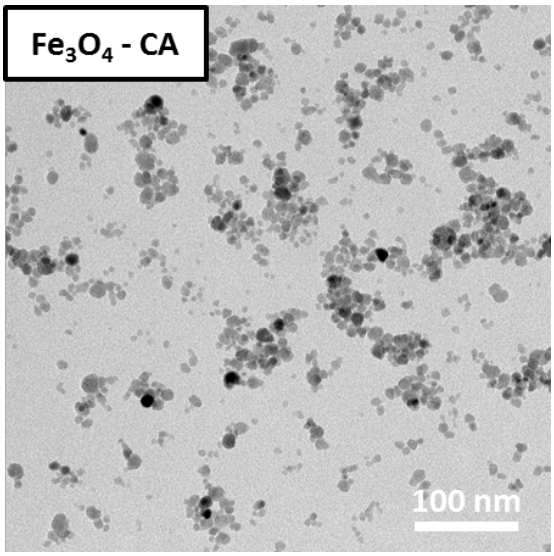


Figure 3. 2 TEM image of citric acid modified Fe_3O_4 particle sample.

The crystal structure of particles and clusters are tested by XRD measurements. Samples are grounded before the test. Step size and time are kept at 0.02 degrees

and 2 seconds respectively. The XRD characterization (Figure 3.3) shows the characteristic peaks of the cubic inverse spinel structure, which means that crystal structure for modified MNPs does not change compared to bare MNPs.

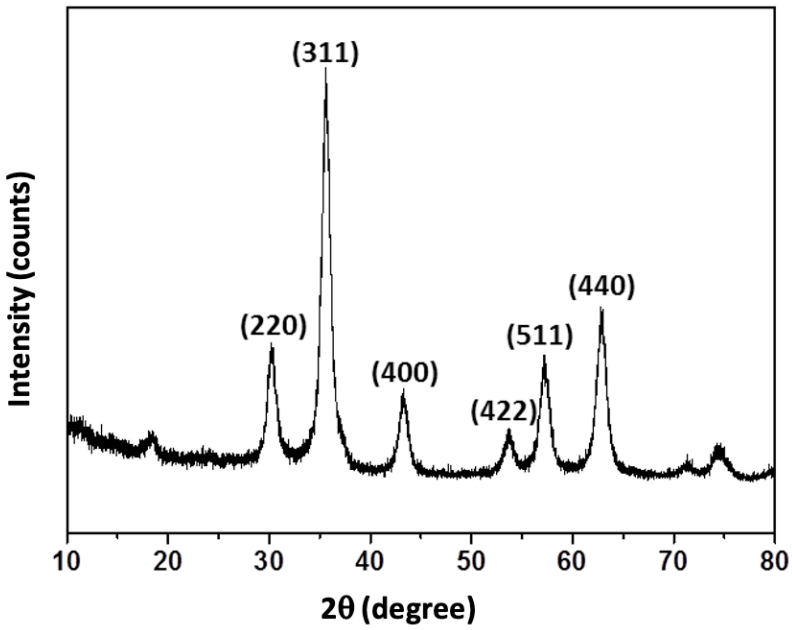


Figure 3. 3 XRD characterization of modified Fe_3O_4 nanoparticles.

TGA is used to measure the stabilized particles' amount around surfaces. The CA modified Fe_3O_4 nanoparticles are heated to 1000 ^oC under an atmosphere of N_2. The rate of the increasing temperature is kept at 10 ^oC/min. The weight fraction of the modified nanoparticles is found to be about 4% by TGA measurement (Figure 3.4).

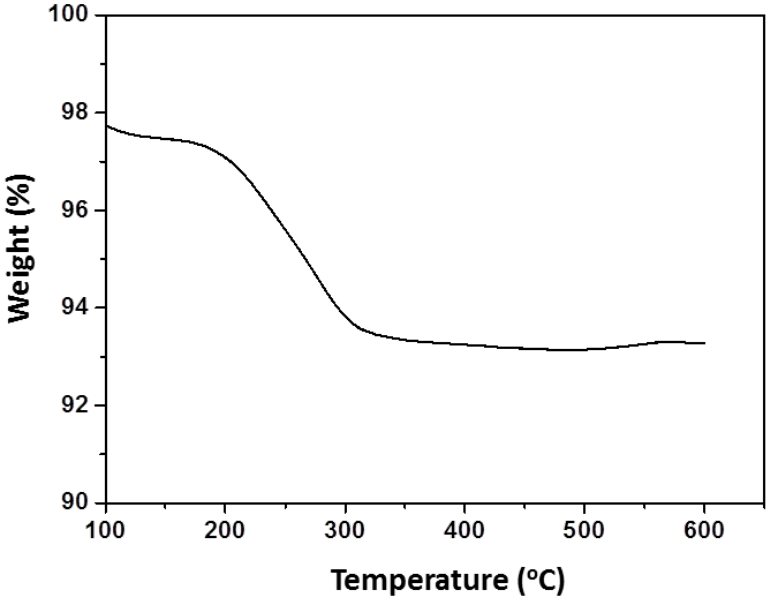


Figure 3. 4 Weight fraction of citric acid by TGA measurement.

Zeta-potential measurements and DLS are used to study the surface potential and hydrodynamic diameter of MNPs. All samples are diluted, and the temperature is set at 25 °C. Figure 3.5 presents the effect of the zeta potential on pH values and the size distribution of CA modified MNFs with pH values. When pH value is below 5, the surface potential is not strong enough to make particles repel each other, leading to severe aggregations. Especially, when the pH is at 2 (Figure 3.5b), hydrodynamic diameter reaches almost 1000 nm. When pH increases to 5, zeta potential drops to -33.8 mV, which means that more carboxyl groups become negatively charged COO-, enhancing the stability and suppressed aggregations. At the pH of 5, the hydrodynamic diameter decreases to 33.8 nm. When the pH value is between 5 and 9, the hydrodynamic diameter is around 34 nm, which does not change significantly. This is because the dissociations of carboxyl groups are completed. In other words, at a neutral pH value, the base colloidal stability is obtained. When pH value increases to 11, it might be related to the increased ionic strength of the suspension [267, 268], caused by Na+ added during the pH

adjustment. At the pH of 11, the decrease of the diameter should be caused by the rise of the ionic strength, which reduces the thickness of the electric double layer [161].

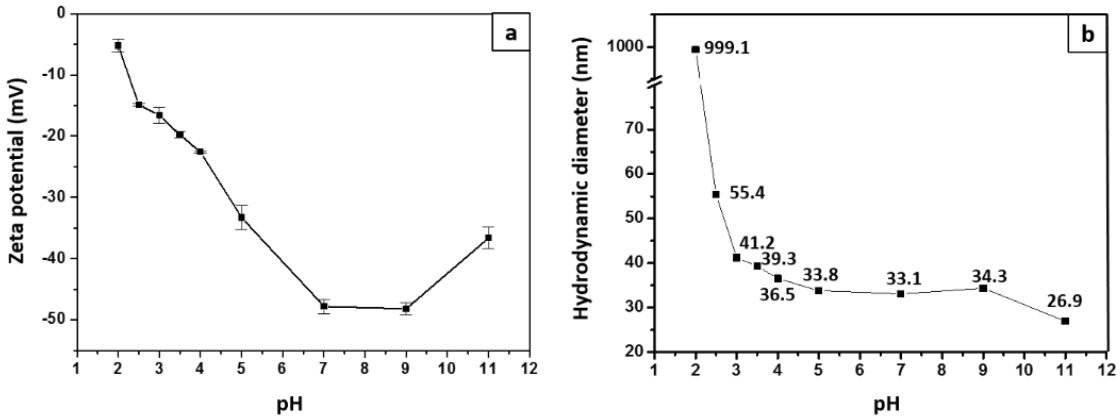


Figure 3. 5 (a) the relationship between Zeta-potential and pH values. (b) relationship between hydrodynamic diameter and pH values of CA coated Fe_3O_4 particles dispersed in the base liquid.

Figure 3.6a shows a comparison between CA modified MNPs and bare MNPs after keeping for 8 months. It is clear that the uncoated sample precipitates down to the bottom after 8 months, while the modified sample is more stable. After vigorous shaking, CA modified MNFs produce little foams (Figure 3.6b) since there is no surfactant in the solution. However, the one stabilized by the surfactant SDS generates more foams.

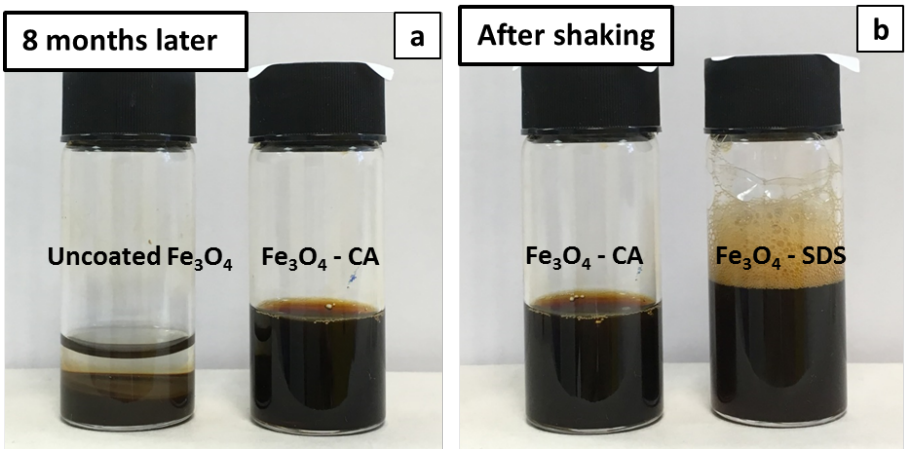


Figure 3. 6 Comparison of colloidal stability (a) and foaming (b) of naked and modified Fe_3O_4.

3.4 Characterizations of Ferrofluids

In this section, the thermal physical properties of modified MNFs are investigated. They include density, specific heat capacity, viscosity, thermal conductivity and convective heat transfer. The detailed specifications are provided in Table 2.

Table 2 Experimental equipment of thermal physical properties.

Helium Pycnometer (Accupyc 1330)	Humidity: 20-80% Voltage: 220/240 VAC Current: 0.25 A Sample Volume: 0.5-100 mL Temperature range ambient to 725 °C
Differential Scanning Calorimeter (DSC) (TA Instruments Q2000)	Temperature accuracy ± 0.1 °C Temperature precision ± 0.01 °C Dynamic measurement range > +/- 500 mW Bearing: air
Rheometer (Anton Paar MCR 302) with a measuring cone (CP50-1)	Max torque: 1 nNm Min torque: 0.5 nNm Angular velocity: 10-9-314 rad/s Temperature range: -160 °C to 1000 °C Measure range: 0.001-5.0 W/(m·K)
TC3020L Liquid Thermal conductivity meter	Temperature range: -30 °C-200 °C Sample volume: ≥ 25 mL Pressure range: 0-20 MPa

3.4.1 Density

Figure 3.7 shows the effect of volume fraction of MNFs on density. The density is measured by Helium Pycnometer (Accupyc 1330), which determines the sample volume by monitoring differential helium gas pressure with and without sample present. Since the density of modified MNPs is higher than that of the base liquid, which is 1.0685 g/mL, the density of nanofluids increases by adding more particles. The increase rate is slow at first and then accelerates when the volume fraction reaches 0.23%. As introduced in Chapter 2, the density of nanofluids is often calculated with the mixing theory. The results are calculated by using mixing rules as shown in Figure 3.7 as the red line. The experimental results are lower than those calculated. Once particles undergo aggregation, the aggregates will form spherical flow units with an effective volume fraction larger than that of isolated particles. As a result, ρ_{nf} is lower than expected at each concentration. However, the maximum relative deviation is only 0.8%, which is accurate for predicting ρ_{nf} of modified MNFs.

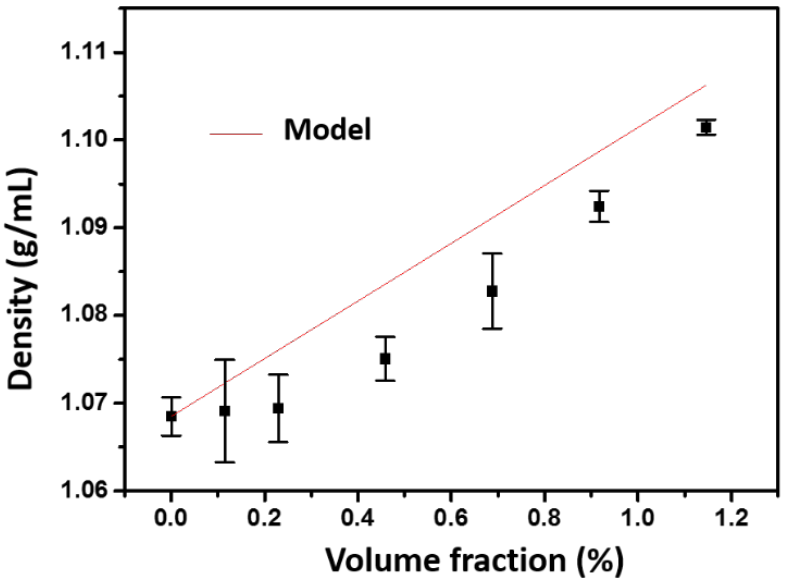


Figure 3. 7 Density of CA modified MNFs as a function of the particle concentration.

3.4.2 Specific heat capacity

To validate the accuracy of the measurements tested, two models are predicted by ϕ dependent $C_{p,nf}$. The first model is based on the mixing theory for ideal gas mixtures as equation 3.1, where subscripts *nf*, *n* and *f* are respectively nanofluids, nanoparticles and the base liquid. The other model is called thermal equilibrium model [87], which relates to the classical and statistical mechanics [83, 93]. The condition for this equation is that the base liquid and nanoparticles achieve thermal equilibrium (equation 3.2). ρ_n and ρ_{bl} are the density of particles and the base liquid respectively. Meanwhile, equation 3.2 is a density-dependent model, which is more accurate for interpreting ϕ-dependent $C_{p,nf}$ [82].

$$C_{p,nf} = \phi C_{p,n} + (1-\phi) C_{p,bl} \tag{3.1}$$

$$C_{p,nf} = \frac{\phi \rho_n C_{p,n} + (1-\phi)\rho_{bl} C_{p,bl}}{\phi \rho_n + (1-\phi)\rho_{bl}} \tag{3.2}$$

The specific heat of MNFs is measured by a Differential Scanning Calorimeter (DSC). The sample is held in an aluminum pan and covered with a lid. An empty pan with lid is used as a reference. The scan is conducted in a nitrogen atmosphere. The temperature firstly maintains at 5 °C for 15 minutes and then increases rapidly to 85 °C with a heating rate of 25 °C/min.

Each test is repeated for 3 times to obtain an average profile of the specific heat as a function of the temperature. It is found that the specific heat increases a little after the temperature is higher than 60 °C. So, the average specific heat in the range of 30 to 60 °C is used in the experimental results between the volume fraction of 0.23% and 1.15%.

Figure 3.8 shows the effect of the volume fraction on specific heat capacity. The results are calculated by two models. Meanwhile, $C_{p,n}$, $C_{p,bl}$ and $C_{p,nf}$ are measured with DSC. $C_{p,n}$ is 1.08 J/g K, which is much lower than that of $C_{p,bl}$ with 3.3 J/g K. The relative deviation of model 2 is 0.9%, and that of model 1 is 1.6%. Model 2 fits the measured results better than model 1. This is because model 2 gives the specific heat when the nanofluids achieve thermal equilibrium [162].

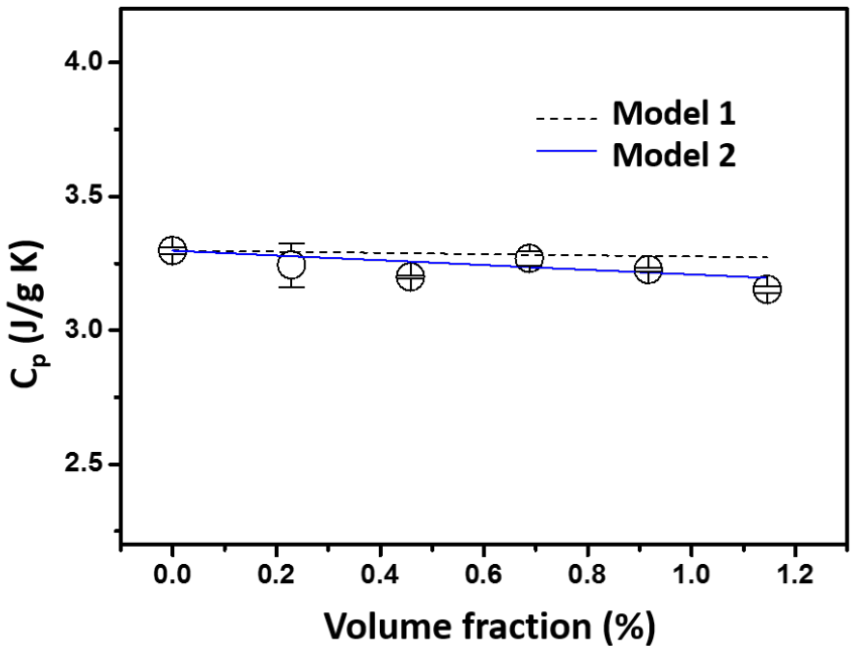


Figure 3. 8 Specific heat capacity of CA modified Fe_3O_4 nanofluids against particle concentration.

3.4.3 Viscosity

Viscosity plays an important role in the thermal applications of nanofluids. This is because the lower viscosity decreases the pressure drop and saves the pump power. Different influencing factors of the viscosity are studied in this section. They include pH values, temperatures and concentrations. The rheological behaviour, as an important parameter of the viscosity, is measured by a rheometer (Anton Paar MCR 302) with a measuring cone (CP50-1). The diameter of the cone is 50 mm, and the angle is 1°. Shear rate is changed from 50 to 2500 s^{-1} and is recorded every 6 seconds. Each shear rate is carried out for 120 seconds under steady conditions. The average value is used as the final viscosity.

With the volume fraction of 0.69% remaining at 30 °C, the effect of the shear rate on the viscosity is studied with pH values. As shown in Figure 3.9 a. When pH values are 2.5 and 3, the modified MNFs exhibit a Non-Newtonian behaviour. In

this range, the viscosity decreases below 40% when the shear rate increases to 2500 s^{-1}. When the pH is between 3.5 and 5, the decrease of the viscosity stops at 800 s^{-1}, with a decrease of 7.2%, 9.0% and 1.8% respectively (Figure 3.9b). When pH value is at 7 and 9, the modified MNFs exhibit the Newtonian behaviour with the decreasing percentages of almost zero. Therefore, Newtonian fluids show better colloidal stability at the pH value of 7 and 9.

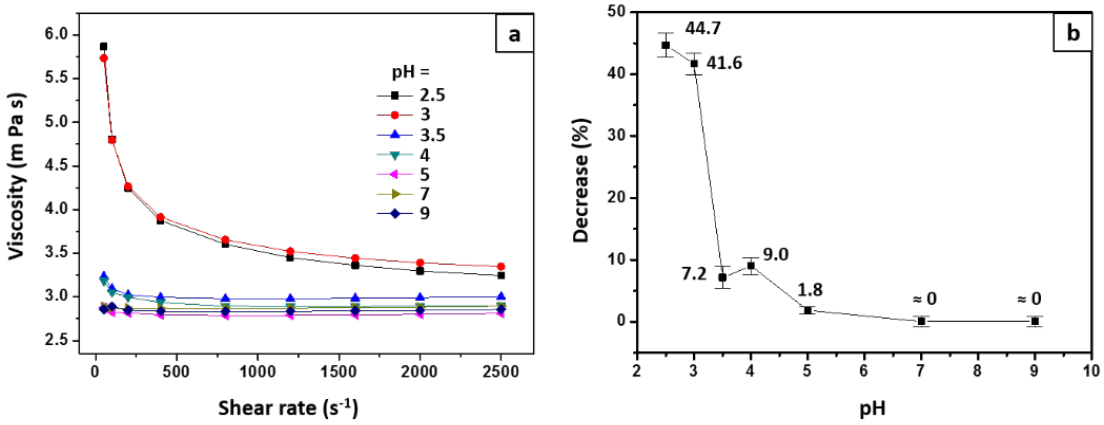


Figure 3. 9 (a) Viscosity as a function of shear rate for CA modified Fe_3O_4 nanofluids at different pH values. (b) Decrease of the viscosity at each pH.

To study the effect of the temperature and the concentration on the viscosity, the pH value is fixed at 8.5, which is between 7 and 9. As shown in Figure 3.10, the viscosity exhibits a linear increase with the concentration at the same temperature. Meanwhile, the viscosity of nanofluids decreases with the increasing temperature. Moreover, the rise of the concentration at the high temperature (45 °C, 50 °C) increases faster than that at a low temperature.

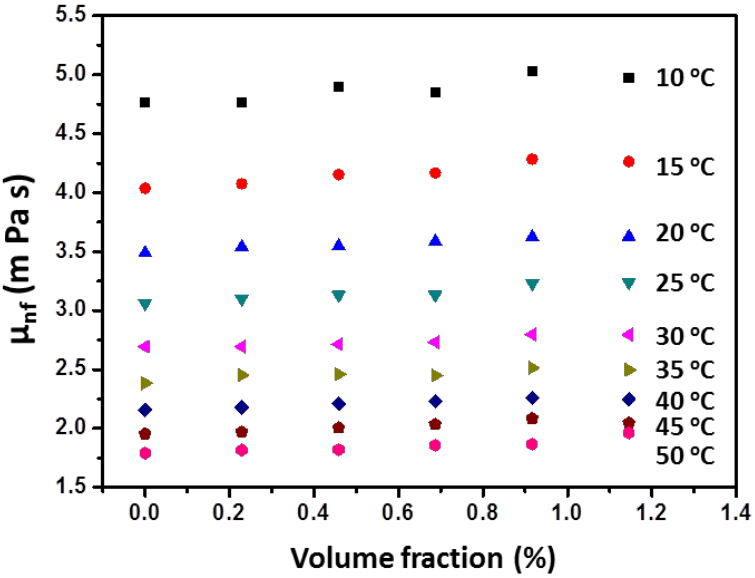


Figure 3. 10 Viscosity of CA modified Fe_3O_4 nanofluids against particle concentration with different temperatures.

3.4.4 Thermal conductivity

Thermal conductivity of the modified MNFs is measured by TC3020L Liquid Thermal conductivity meter, which is based on the transient hot-wire method. Figure 3.11 shows the thermal conductivity of nanofluids of CA modified Fe_3O_4 nanoparticles at different temperatures and concentrations. The pH value is kept at 8.5 with the volume fraction ranging from 0 to 1.2%. When temperatures of a 1.2% particle volume fraction are set at 30, 40, 50 and 60 ^oC, their thermal conductivities bring enhancements of 2.2, 2.3, 2.3 and 1.6% respectively, such enhancements are much lower. Generally, the thermal conductivity increases with the increase of temperatures and concentrations. However, when the concentration is at 0.34%, thermal conductivity is higher than that at 0.52% and 0.69%. At 40^oC, the thermal conductivity of 0.34% is even higher than that of 1.2%.

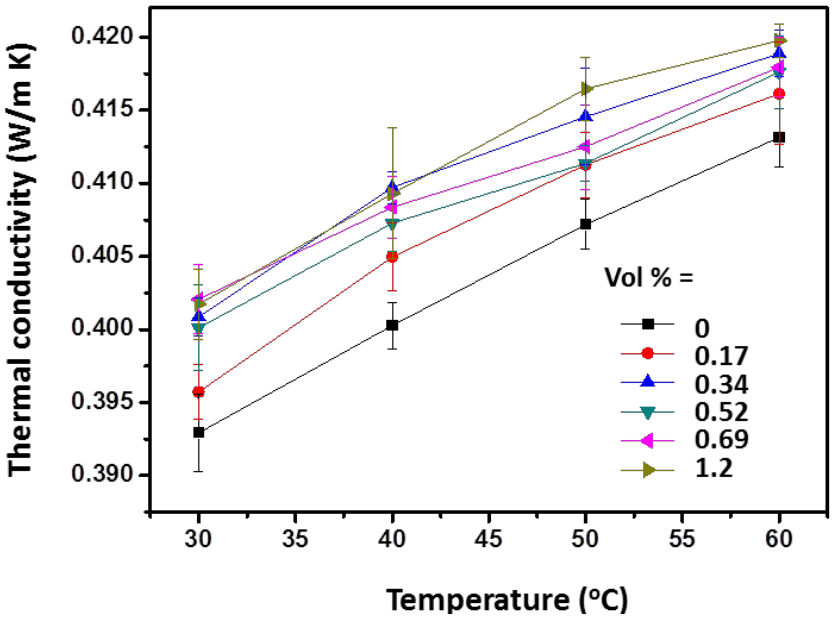


Figure 3. 11 Thermal conductivity of CA modified Fe_3O_4 nanofluids against the temperature at different particle concentrations.

There are many arguments on influencing factors of the thermal conductivity of MNFs [163, 164]. Based on our experimental results, particle aggregations dominate the thermal conductivity [107, 165]. Particle aggregations can form thermal percolation paths that work like "highway" for heat transfer [118]. Moreover, the degree of the aggregation is highly related to the thermal conduction of MNFs. Serious aggregations will lead to the sediment of particles, consequently, the heat conduction only accounts on the base liquid. However, when particles are ideally dispersed, thermal percolation paths are not formed to enhance heat transfer. Evidence has shown that the enhancement observed on the ideally dispersed particle suspension can be very little [166].

In our study, the experimental data are compared with the Maxwell model that presumes that nanofluids have common features with solid-liquid mixtures. Maxwell model is described as,

$$k_{nf} = k_{bl}\left[\frac{k_p + 2k_{bl} + 2\phi(k_p - k_{bl})}{k_p + 2k_{bl} - \phi(k_p - k_{bl})}\right] \quad (3.3)$$

The results show that experimental data do not fit well with the Maxwell model. When concentration is too low or too high (Figure 3.12) compared to the Maxwell model, thermal conductivity is even lower than the model. However, when the concentration is moderate, thermal conductivity is much higher than the Maxwell model. This is because of different degrees of the aggregation. At a low concentration, MNFs are ideally dispersed, and the heat conduction is mainly conducted by the base liquid. When the concentration is too high, a large number of agglomerations are formed in MNFs, leading to precipitation. This is similar to the fully dispersed condition when the base liquid dominates heat conduction. Therefore, only when the concentration is moderate, MNPs can form chain-like paths to enhance the thermal conductivity of MNFs.

Based on the experimental results, the effects of the solid-like nanolayer [167, 168], interfacial thermal resistance [169] and Brownian motion [170-172] are not the main reasons for thermal conductivity enhancement. The degree of aggregations is the key to the thermal conductivity of MNFs.

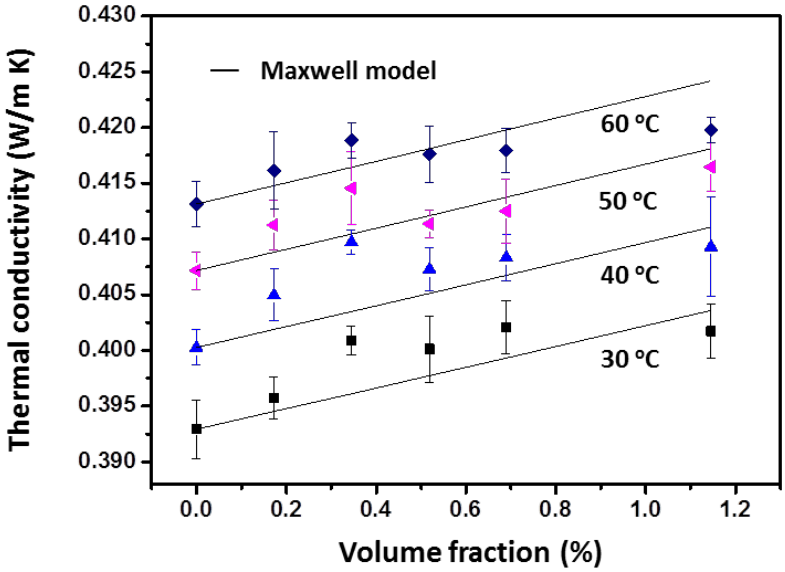


Figure 3. 12 Comparison of experimental data and the Maxwell model in thermal conductivity.

3.4.5 Convective heat transfer

For convective heat transfer, the detailed specifications are shown in Table 3 and the experimental schematic diagram is shown in Figure 3.13. The test section is a copper-made tube with an inner diameter of 6.8mm and the length of the tube is 1000 mm. The tube is heated by a rope heater wrapped along the test section. Two K-type thermal couples are placed at two ends of the copper tube to test inlet and outlet temperatures. Three more thermocouples are located along the tube surface. Meanwhile, two differential pressure gauges are applied for the pressure drop in the test section. The test section is covered with thermal insulation to minimize heat loss.

Table 3 The detailed specifications of the convective heat transfer.

Model	Specifications
Copper tube	Inner diameter: 6.8 mm Length of test section: 1000 mm
Rope heater (FGR-080)	Max allowable temperature: 482 °C Standard diameter: 3/16 inch Voltage: 120/240 Volt ac Linear wattage: 4 Watts/in.
K-type thermal couple	Temperature range: -75 °C, 250 °C Standards Met: IEC
Differential pressure meter (Digitron 2000P)	Pressure measurement: 0-25 mbar Overpressure maximum 350 bar Operating temperature: -10 °C to 50 °C
Fluorooptic fibre thermometer (OPSENS SOLUTIONS INC, Canada)	Temperature range: -100 °C to 400 °C Unaffected by electromagnetic interference Unaffected by radio frequency interference
Ultrasonic flow meter (UF8B, Cynergy 3)	Max. flow rate: 8 L/min Min. flow rate: 0.1 L/min Transitional flow: 0.4 Output selectable: pulse/Analogue
Electric motor (EC IE1, UK)	Operating power: 1.5 kW Max speed: 1400 r/min

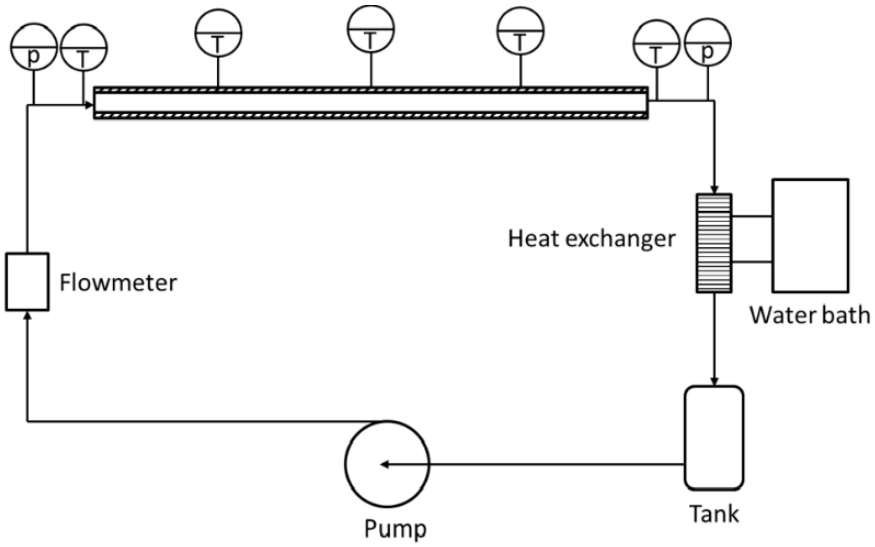


Figure 3. 13 The experimental schematics for the convective heat transfer.

As shown in Figure 3.14, K-type thermocouples are calibrated by the fluoroptic fibre thermometer. The thermocouples and standard platinum resistance are tested

in a water bath (10 ºC - 70 ºC). Temperature data are recorded when they reach the steady state. The temperature increment of each calibration point is set at 5 ºC. The volumetric flow rate is obtained by an ultrasonic flow meter with an output signal of voltage. To calibrate the flow meter, the liquid is pumped into a 1 L cylinder, and the volume is measured in every 10 seconds. The voltage increases proportionally with the increasing flow rate. The proportionality constant is found to be 1.66 L/(min V) for water and 1.51 L/(min V) for the base liquid and MNFs.



Figure 3. 14 Experimental setup for the measurement of heat transfer coefficient of nanofluids.

According to the convective heat transfer coefficient,

$$h = \frac{q}{t_{w,in} - t_f} \tag{3.4}$$

where q is the input heat flux, $t_{w,in}$ is the inner wall temperature and $t_f = 0.5(t_{out} + t_{in})$ is the mean bulk temperature of the fluid. The heat supplied to the system is calculated by $\dot{m}C_{p,f}(t_{out} - t_{in})$, where $\dot{m}$ is the mass flow rate. $t_{w,in}$ is calculated as,

$$t_{w,in} = t_{w,out} - \frac{q}{2\pi Lk} ln \frac{D_{out}}{D_{in}} \tag{3.5}$$

where $t_{w,out}$ is the surface temperature of the tube, L is the length of the tube, k_{copper} is the thermal conductivity of copper, D_{in} and D_{out} are inner and outer diameters respectively.

The Nusselt numbers of water calculated from experimental data are compared with those predicted by the Seider-Tate equation [173] for laminar flow and the Dittus – Boelter equation for turbulent flow.

$$Nu = \frac{hD_{in}}{k_f} \tag{3.6}$$

Seider-Tate equation:

$$Nu = 1.86(Re \cdot Pr \cdot \frac{D_{in}}{L})^{\frac{1}{3}}(\frac{\mu_f}{\mu_{w,f}})^{0.14} \tag{3.7}$$

Dittus-Boelter equation:

$$Nu = 0.023 Re^{0.8} Pr^{0.4} \tag{3.8}$$

Re and Pr are defined as follow,

$$Re = \frac{\rho_f u D_{in}}{\mu_f} \tag{3.9}$$

$$Pr = \frac{C_{p,f}\mu_f}{k_f} \tag{3.10}$$

where μ_f and $\mu_{w,f}$ are dynamic viscosities at t_f and $t_{w,in}$ respectively, u is the velocity of the fluid, $C_{p,f}$ is the specific heat of the fluid and k_f is the thermal conductivity. Thermal physical properties of water are the same with reported ones. The uncertainty of the results is most likely to be caused by measuring errors of parameters, such as flow rate, temperature and pressure drop. The measurement uncertainty of the flow rate and the temperature are 3% and 1 °C respectively. During the investigation of the convective heat transfer of MNFs, one has to consider the measuring errors of thermal physical properties of MNFs. The uncertainties of the Reynolds number, convective heat transfer and Nusselt number are analysed by using the method described by Moffat [174]. If y is a function of several independent variables, x_i, each with their uncertainties, δ_{xi}, the overall uncertainty in y is calculated as,

$$\delta y = \sqrt{\sum_{i=1}^{n} (\frac{\partial y}{\partial x_i})^2 (\delta x_i)^2} \tag{3.11}$$

Calibration

To calibrate the volume flow rate of nanofluids, the voltage signal of the flow rate is not only recorded, the three-way valve is also adjusted to collect liquid to the 1 litre measuring bottle and to record the measurement time. After recording different flow rates for 10 times, it is found that the actual volume flow rate is linearly related to the voltage signal.

To verify the correct functioning of the experimental apparatus, primary tests have been carried out by measuring convective heat transfer characteristics of water at 40 ˚C. The experimental data are compared with the values calculated by the Dittus-Boelter model as shown in Figure 3.15. The uncertainty of Re number is very small (0.000109%). The average uncertainty in the calculation of Nu number is 7.3% when Re is less than 10000. The experimental results show a good agreement with the Dittus-Boelter model. The average deviation is 4%.

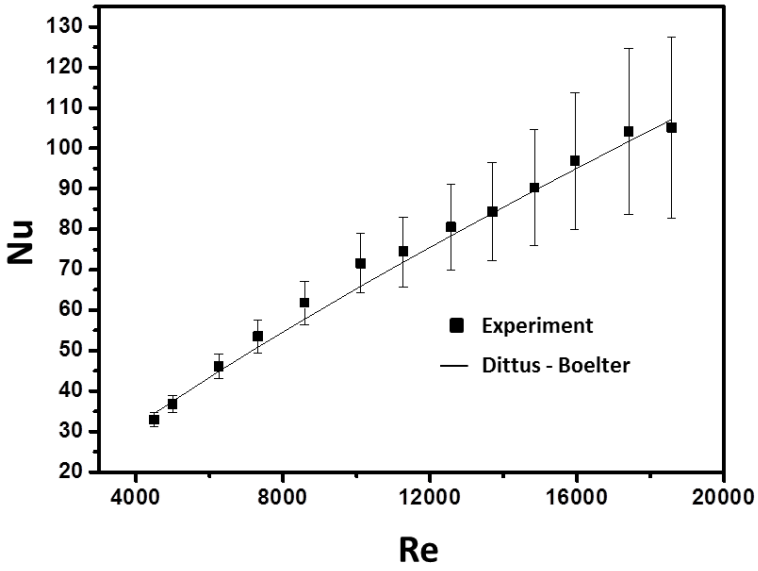


Figure 3. 15 Comparison between the experimental data of water with the ones calculated by the Dittus-Boelter equation.

Experiments are carried out to measure the convective heat transfer coefficient *h* of the base liquid and 0.23 vol.% of MNFs. The pH of MNFs is adjusted to 8.5, and the inlet temperature is kept at 40 °C. Figure 3.16 shows the comparison of the convective heat transfers between the base liquid and MNFs at different Reynolds numbers. Uncertainty values have been calculated for all the measured cases. The uncertainty of Re number is very small (0.00011%). The average uncertainty in the calculation of the convective heat transfer coefficient is 8.6%. Most engineering applications are related to turbulence as turbulence is the coolant flow in an IC

engine. To obtain a fully developed turbulent flow, Reynolds number generally should be higher than 10000. In this work, due to the limitation of the pumping power, Reynolds number can only cover a range from 1000 to 6000, which can achieve the laminar range, transitional flow, and some of the turbulent flow.

For laminar flow (Re <2500), *h* of MNFs is almost the same as the base liquid (Figure 3.16). Once Re > 2500, *h* becomes higher than that of the base liquid. The average enhancement is 11.9%. Usually, the heat transfer enhancement by using nanofluids is attributed to: first, the dispersed particles improve the thermal conductivity of the boundary layer; secondly, the particle migration disturbs the boundary layer; thirdly, particle aggregates work like “obstacles” at the wall of the pipe, which breaks the boundary layer, thus reinforcing local turbulence. Now, the first two reasons should be paid more attention since the colloidal stability of MNFs has achieved the best. From the last section, it has been known that the thermal conductivity increases by only 2-3% as the particle concentration reaches 1 vol.%. Therefore, the increase in the thermal conductivity of the boundary layer should not play an important role.

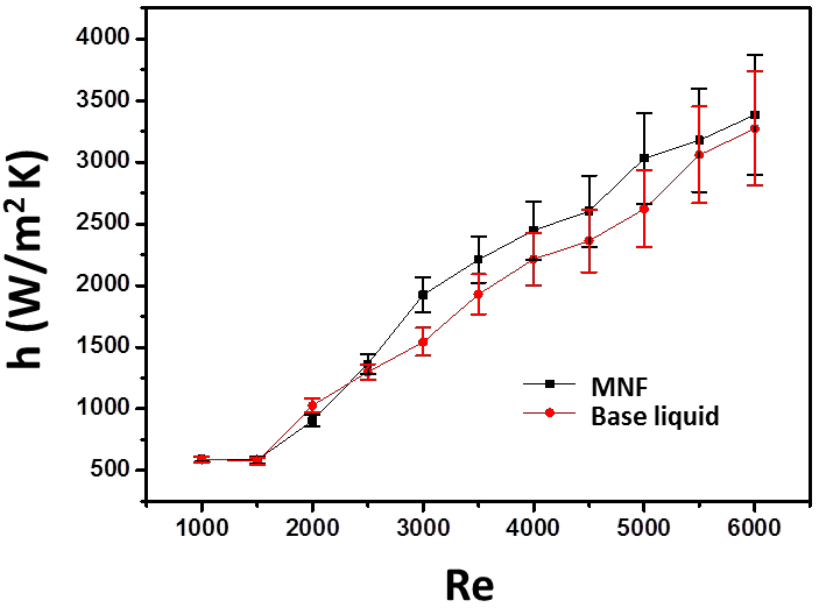


Figure 3. 16 Convective heat transfer coefficients of the base liquid and MNFs as a function of the Reynold number.

3.5 Summary

In this chapter, to obtain the well-dispersed MNFs, Fe_3O_4 nanoparticles are synthesized by the co-precipitation method and modified with citric acid. The average size of particles is approximately 10 nm. In addition, the effects of temperature, concentration and colloidal stability on thermal properties of Fe_3O_4 nanofluids are also discussed.

The colloidal stability of modified particles is enhanced by reducing the acidity of the particle suspension. By increasing the pH to 7, the surface potential of particles keeps increasing due to the dissociations of CA attached to the particles. As a result, the enhanced surface potential helps particles repel each other, resulting in a decrease of the hydrodynamic size of particles. The particle aggregations are suppressed to the lowest level as pH reaches 5. The dissociations of CA attached are completed at the neutral pH, which suggests that the best colloidal stability is obtained. At the neutral pH, the viscosity of Fe_3O_4 nanofluids does not change with

shear rate despite of the variance in the particle concentration and temperature. It is found that, at the pH of 8.5, the thermal conductivity of nanofluids changes with the particle concentration according to the Maxwell model. Although thermal conductivity enhancement of well-dispersed nanofluids is relatively low, proper concentration and colloidal stability are competitive in the thermal conductivity. The smaller viscosity and the better colloidal stability should be competitive when the nanofluids are considered for convective heat transfer. In addition, once particles undergo uncontrolled aggregations, it is difficult to predict the thermal conductivity and the viscosity at a certain temperature and particle concentration. Therefore, nanofluids at the pH of 8.5 are used for the investigation of the convective heat transfer. The convective heat transfer is found to be enhanced by over 10% for Re > 2500. The enhancement should be explained by the particle migration.

Chapter 4 The Distribution of Droplet Deposition Patterns affected by Thermal Strategies

4.1 Introduction

The ‘Coffee ring’ effect is a pattern formation deposited by the non-volatile solute of the liquid after complete evaporation. However, ring-like patterns are not desirable in many applications, such as pharmaceutical purification [29], salt manufacturing [30], inkjet printing [31-33], DNA microarrays [34, 35], nanotechnology [36-38] and so on. Therefore, researchers have investigated different effective methods to actively manipulate the distribution of the drying formations and their mechanisms.

The interests in the droplet deposition pattern are inspired after the ring stain was first proposed and analysed by Deegan [39]. For isothermal evaporation, the evaporation flux at the edge is higher than the air-liquid interface, forcing particles to transport from the central area to the periphery for the compensation of the loss of solvents. Eventually, evaporation flow carries the central particles to the contact line, leading to most particles accumulating along the edge, thus, forming a ring-like formation.

To suppress the ring-like pattern formation, researchers have studied methods to control the distribution of deposition patterns. Mainak et al. [130] experimentally suppressed the coffee ring effect under volatile condition. Dan Soltman et al. [31] investigated effects of the droplet spacing and the temperature on droplet deposition pattern. In their study, they found an optimized condition to control the size of the pattern. Alexandros Askounis et al. [175] studied biodrop deposition and found that

the morphology of the biodrop can change the ratio of CCR and CCA in the process of the evaporation. In addition, Chen et al. [123] experimentally showed the onset time of CCR-CCA transition and found that the critical base size at the Cassie-Wenzel transition depend on the surface roughness. Many researchers [39, 49, 126, 176] found that the Marangoni flow and the capillary flow were two significant factors influencing the deposition pattern and tried to control patterns through balancing them.

However, most solutions intend to manipulate the distribution of pattern formations by adjusting properties of original solvents with chemicals. This work aims to explore an effective method to control the distribution of droplet deposition patterns without changing chemicals. In this chapter, droplets have been experimentally investigated through thermal strategies, which are substrate temperatures and heating directions.

For substrate temperatures, both saline and MNFs droplets are investigated by controlling substrate temperature, ranging from 10 °C to 70 °C. To analyse the mechanism behind drying patterns, 3 μm microbeads are used to analyse the flow motion inside the droplet with microscopy (OPTIKA 400) mounted by CCD camera (BASLER acA2040-90uc). IR camera is also used to record the temperature distribution of the air-liquid interface of the studied droplets. The experimental results show that the distribution of deposition patterns generally transits from uniformity, the ring-like structure to the dual-ring structure with an increase of its temperature. The Marangoni flow plays an important role in temperature-dependent pattern formations.

For different thermal directions, the deposition patterns of saline droplets are investigated by both the local and the substrate heating with different wettability. For the local heating, it is induced by the laser light, leading to rapid increase of the local temperature. However, the local high temperature makes modified MNPs invalid. Therefore, MNFs cannot be investigated in this section. The whole process of the droplet evaporation is recorded as it transits from the CCR mode to the CCA mode. In this process, the CCR stage dominates most of the evaporation time. Experimental results show that, without any chemicals, the laser-induced local heating drives particle deposition patterns from ring-like to dot-like patterns on a hydrophilic surface, transporting most saline solvents to the centre. For a hydrophobic surface, the results show that particles tended to assemble in the central region, while the deposition pattern is slightly different compared to that on the hydrophilic surface due to the surface tension gradient. Meanwhile, physical mechanisms of the local heating are also explored in the present study.

4.2 Materials

The hydrophobic material is a combination of nanoparticles and functional materials in the solution [177]. Silica (SiO_2) nanoparticles (fumed powder) with average size 7 nm and poly dimethyl siloxane (PDMS) solution (Molecular weight 95000, Fluka) are purchased from Sigma Aldrich. Firstly, PDMS is dissolved in white spirit solvents, forming the solution with a concentration of 6 wt.%, prior to adding nanoparticles. The SiO_2 nanoparticles of 7 nm are then dispersed into solution with concentrations of 0.5, 1.0, and 2.0% w/v respectively. Among them, 2.0% w/v exhibits a better hydrophobic property than other concentrations and is finally coated on the substrate.

For the hydrophilic material, water-based magnetic nanofluids are coated on the substrate. $FeCl_3 \cdot 6H_2O$ and $FeCl_2 \cdot 4H_2O$ are firstly dissolved in the deionized water. After removing the oxygen through nitrogen for 15 minutes, ammonium hydroxide is added to the solution under vigorous stirring at a temperature of 60 °C. With the aid of the ultrasonic treatment, precipitates collected are then modified by citric acid and finally dispersed into a base liquid [178].

PDMS-SiO_2 and magnetic nanofluids are both deposited on the substrate by airbrush. The coated substrates are dried in an oven at 40 °C for 2 hours. Subsequently, the treated substrates are kept at the ambient temperature for 2 days before experiments. As shown in Figure 4.1 and 4.2, the contact angle of the hydrophobic surface is 111.91 °, and the contact angle of the hydrophilic surface is 25.96 °.

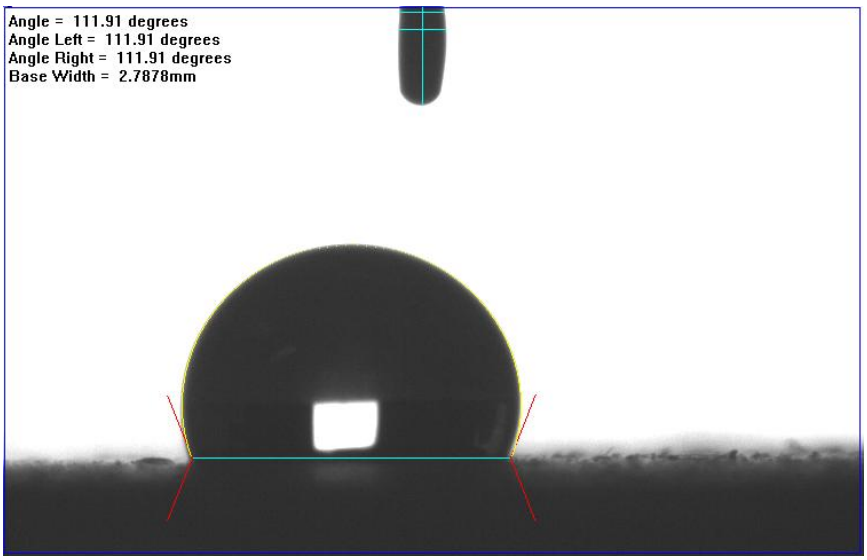


Figure 4. 1 Contact angle of the hydrophobic surface coated by PDMS-SiO_2.

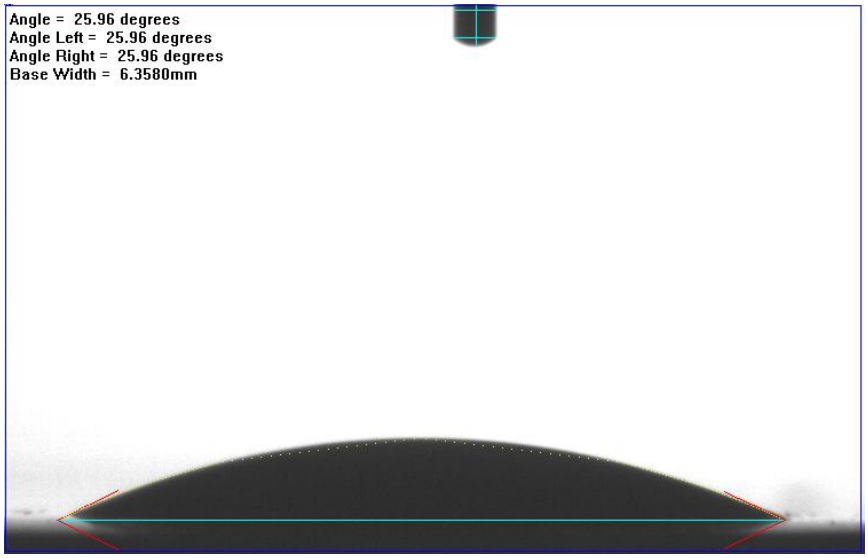


Figure 4. 2 Contact angle of the hydrophilic surface coated by magnetic nanofluids.

4.3 Experimental Setup

The experiments are conducted to control deposition patterns with the substrate temperature and the local heating. In this section, the detailed specifications are provided in Table 4 and the experimental setup is as follows.

Table 4 The detailed specifications for deposition patterns.

Micropipette (Ossila (C2001V1))	Volume range: 1-10 µL Accuracy: ±2.5 - 1.0% Repeatability ≤ 1.5-0.4%
Microscope (Optika)	Total magnification: 40x, 100x, 400x, 1000x Eyepieces: wide field WF10x/18
CCD camera (Basler aca2040-90uc)	Resolution: 2040px x 2046px Pixel size: 5.5 µm x 5.5 µm Frame rate 90 fps
High speed camera (Phantom v640)	Resolution: 2560 x 1600 – 8 bits, 12 bits frame rate: 1500 fps (full resolution)
Water bath (PolyScience 8006A11B Heated/ Circulating Waterbath)	Temperature range: -5 °C to 150 °C Temperature stability: +- 0.05 °C Readout accuracy: ± 0.5 °C Pressure flow rate: 2-speed, 9 or 15 lpm
IR (FLIR (SC7600M))	Pixel resolution: 640 x 512 Pixel pitch: 15 µm Spectral ranges: 1.5 - 5.1 µm Optional camera calibration range: -20 °C to 300 °C

4.3.1 Experimental setup for substrate heating temperatures.

For the substrate heating, both saline and MNFs droplets (0.2 wt.%) are deposited by a micropipette with the volume of 2 μL. The saline droplets are prepared by dissolving sodium chloride powders (NaCl, >99%) into deionized water with a concentration of 2.0%, which is also applied in the following local heating experiments. In terms of the synthesis of MNFs, it has been introduced in the previous section.

The test section is shielded in an open side cylinder to prevent the air turbulence disturbance. Side glass is placed to support the saline sample with a proper contact angle. Meanwhile, the side glass is attached to the aluminium heat exchanger which is connected to a water bath to control the substrate temperature of the test section. The substrate temperature ranges from 10 °C to 70 °C. Two calibrated K-type thermocouples with an accuracy of 0.05 K are attached to the surface of the side glass with one at the boundary and the other at the centre to monitor the temperature uniformity. The substrate temperature is regarded as uniform only when the temperature difference between the two thermocouples is less than 0.1 K.

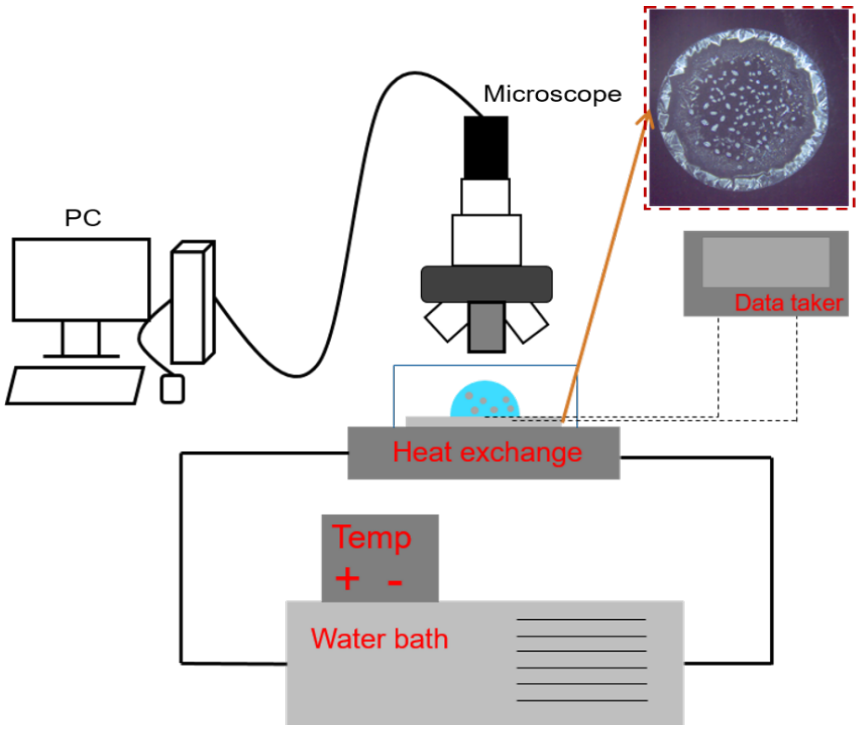


Figure 4. 3 Schematic set-up for controlling deposition patterns through substrate temperature.

4.3.2 Experimental setup for local heating

To supply a local heating (Figure 4.4), a 100 mW laser-induced heater (RPMC OEM), with the wavelength of 1392 nm, is placed at the apex of the saline droplet. Thus, the saline droplet can absorb heat from the pointed laser. Saline droplet has a concentration of 2 wt.%, and volume is 2 µL controlled by a micropipette for each test. A phantom v640 CCD camera is used to record the whole process of an evaporating saline droplet. LEDs array illuminators are placed to ensure that the CCD camera has enough exposure. In the experiment, the test substrates are coated with the hydrophobic and the hydrophilic materials respectively.

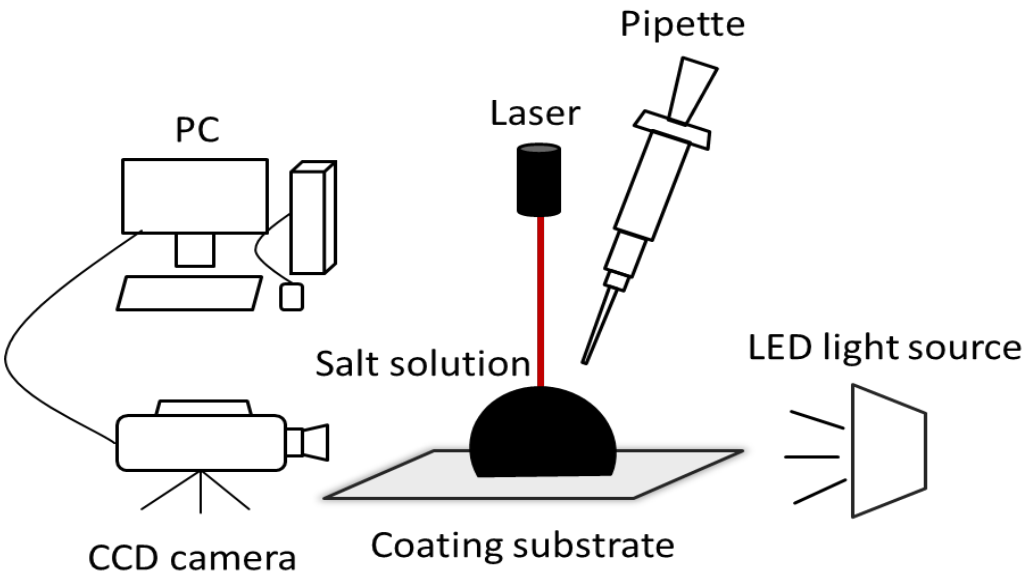


Figure 4. 4 Schematic set-up for deposition patterns of the saline droplet with both the local and the substrate heating on different wettability.

4.4 Results and Discussion for Substrate Temperatures

In this section, drying patterns of both saline and MNFs droplets are studied to investigate the effect of substrate temperatures on deposition patterns. The substrate temperatures are classified into three ranges, which include the low-temperature range (10 °C, 15 °C and 20 °C), the ambient temperature (25 °C), and the high-temperature range (40 °C, 55 °C and 70 °C). Each temperature is conducted three times to ensure repeatability. In addition, latex microbeads, with an average diameter of 3.0 μm made of polystyrene, are conducted to understand the flow motion and mechanism. Microscopy (OPTIKA 400) mounted with CCD camera (BASLER acA2040-90uc) is used to track the motion trajectory of particles. The surface temperature of the droplet is also recorded by an IR camera (SC7600M), which is used to analyse the effect of the temperature distribution along the air-liquid interface.

4.4.1 The properties of pattern formations with substrate temperatures.

Time is normalised by the evaporation lifetime, T/T_0, where T_0 is the time for complete evaporation and T refers to current evaporation time. Based on the distribution of deposition patterns, each drying formation is divided into three regions, namely central region, gap region and edge region. For the edge region, it is defined as the area along the contact line; for the central region, it refers to the central area of the whole pattern; The area between the central region and the edge region is defined as a gap region. In this section, the pattern features for both saline and MNFs are introduced from the low-temperature range to the high-temperature range, then the flow motion and analysis of different pattern formations are also discussed.

In the low-temperature range (10 °C, 15 °C, 20 °C), the entire evaporation process of saline droplets is shown in Figure 4.5. After complete evaporation, all three patterns show ring-like structures along the contact line, but not obvious as a typical coffee ring structure. There is no gap between the interior and the edge. Meanwhile, large-size crystals form due to the saturation inside the edge. It is clear that the size of the crystal decreases and the number of the crystal increases with the temperature increasing. Except for crystals, the distribution of the deposition pattern exhibits a more uniform property at the low-temperature range.

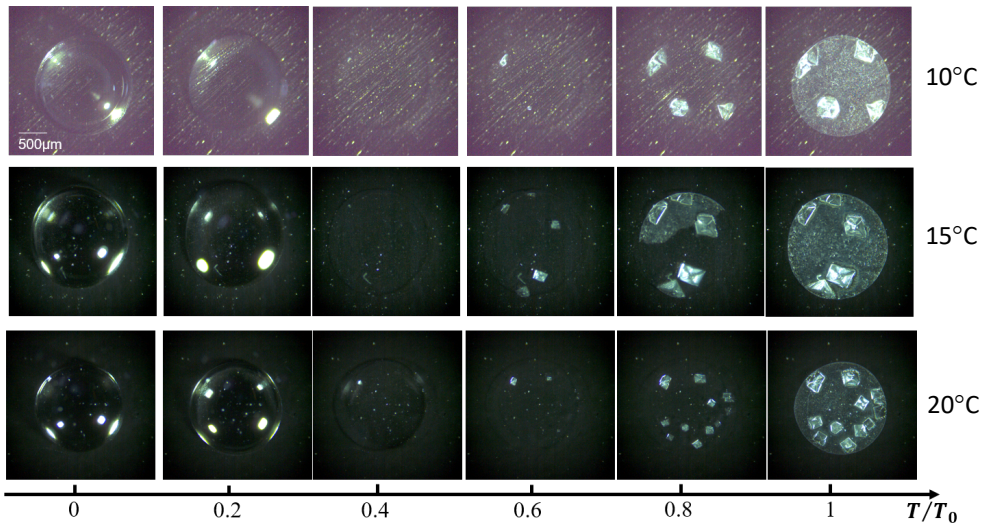


Figure 4. 5 Evaporation process of saline deposition patterns at temperatures (10 °C, 15 °C, 20 °C).

When it comes to MNFs droplets at the low-temperature range, all deposition patterns exhibit coffee ring patterns in the middle of the drying process (Figure 4.6). After complete evaporation, the ring-like structure becomes more prominent as the temperature increases from 10 °C to 20 °C. At 10 °C, the particle distribution is significantly different compared to other temperatures. The width of the ring belt at the edge is much wider than that at 15 °C and 20 °C respectively, and there is a clear spacing between the central region and the edge region. This may be because at 10 °C, the capillary flow is not high enough to transport magnetic nanoparticles to the contact line. Both the size and mass affect the path of particles, thus, some magnetic nanoparticles get stuck on the path to the contact line and finally a wide ring belt is formed.

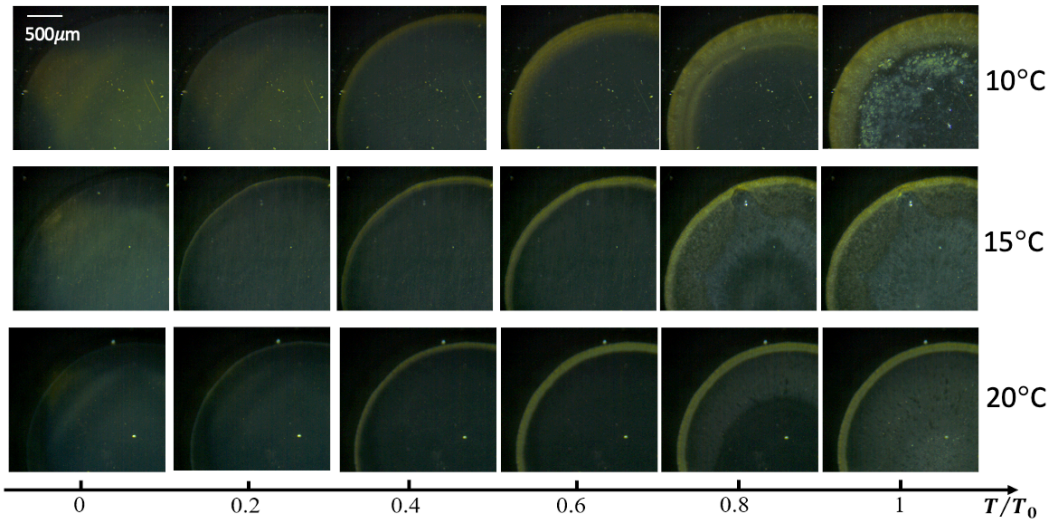


Figure 4. 6 Evaporation process of MNFs deposition patterns at the low temperature range (10 °C, 15 °C, 20 °C).

At 25 °C (Figure 4.7), there are fewer saline crystals in the central region with the smaller size compared to the low-temperature range, and the number of salt particles distributed at the interior significantly reduced. A gap region is formed between the central and boundary, but it is not prominent. Moreover, the ring-like structure is presented at the edge. The crystallization at the edge is concentrated and potentially exhibits towards the interior.

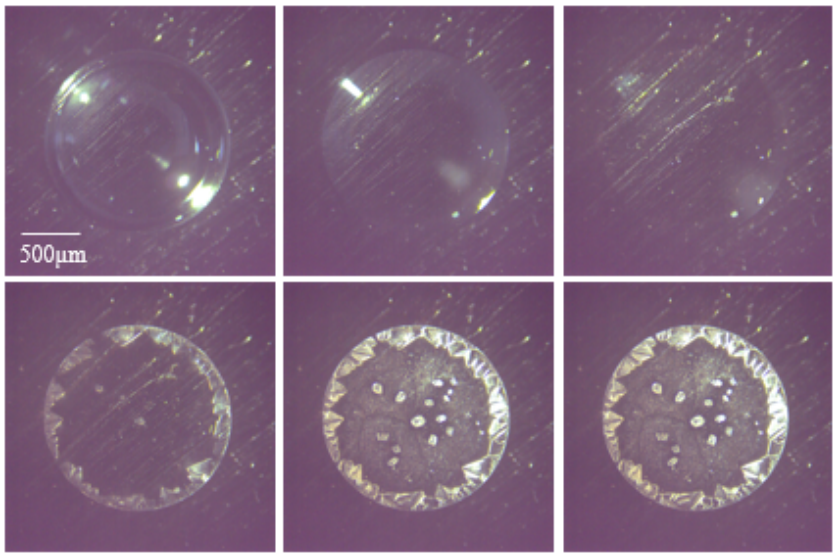


Figure 4. 7 Evaporation process of saline deposition patterns at 25 °C.

For deposition patterns of MNFs at 25 °C, similarly, the ring-like structure can be observed at the early stage of the evaporation (Figure 4.8). More magnetic nanoparticles aggregate along the contact line with the evaporation process. When it almost dries up, the ring belt along the contact line tends to move radially towards the central region, forming a finger shape pattern. Compared to the low-temperature range, fewer particles deposit at the central region and a vague gap forms when the droplet dries up.

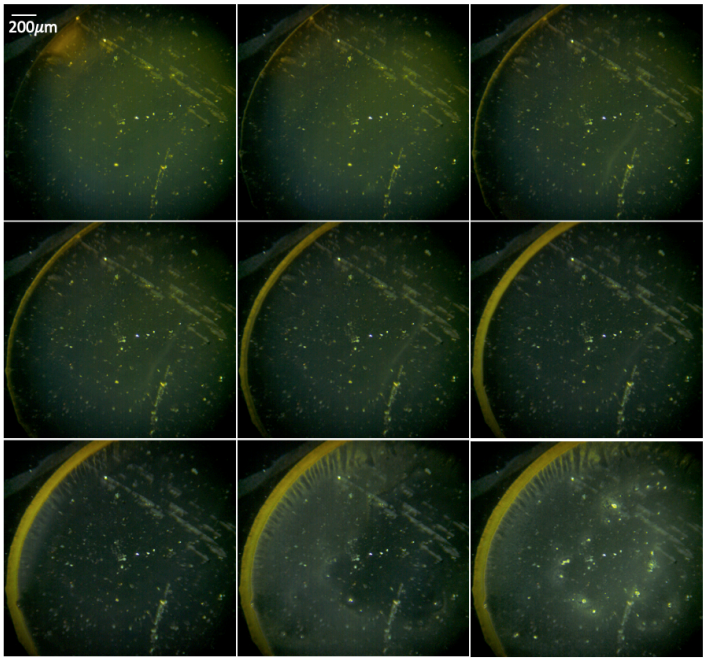


Figure 4. 8 Evaporation process of MNFs deposition patterns at 25 °C.

When temperatures increase to the high-temperature range (40 °C, 55 °C, 70 °C) as shown in Figure 4.9, all three crystal patterns are formed at the edge. The relative time for the start of the patterns is earlier with the increasing temperature. At 40 °C, the distribution of the deposition pattern is similar to that at 25 °C, forming a ring-like structure along the contact line. However, when temperatures are at 55 °C and 70 °C, the secondary rings are formed which are close to the contact line. There is a groove shape patterns between two rings. At the central region, the number of

saline particles rises, while the crystal size decreases. Meanwhile, more particles assemble in a dual ring rather than the central region with the increase of the temperature.

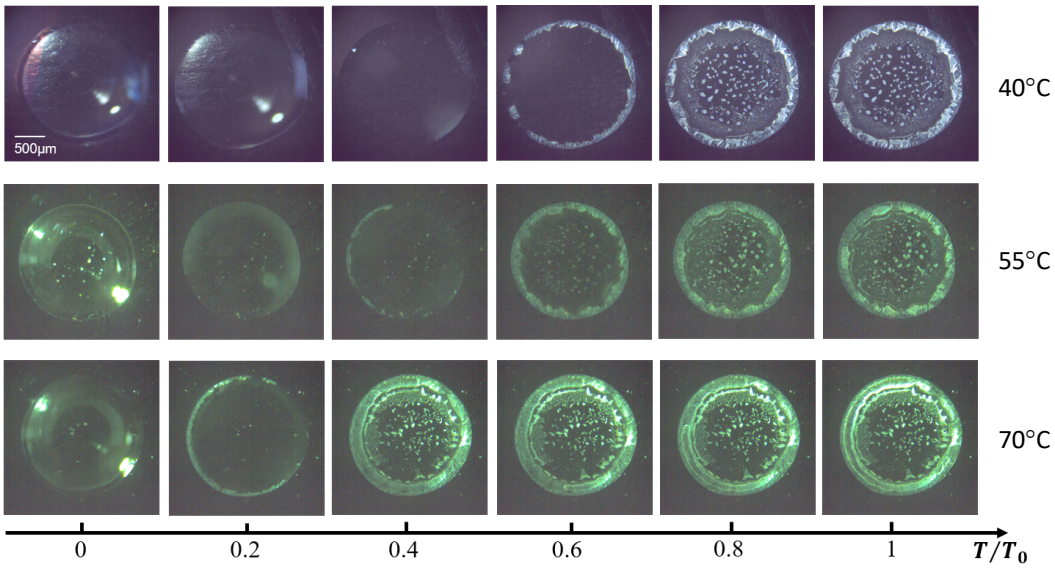


Figure 4. 9 Evaporation process of saline deposition patterns at the high-temperature range (40 °C, 55 °C, 70 °C).

For MNFs droplets at the high-temperature range, the coffee ring formation is accelerated. At 40 °C, the distribution of drying patterns of MNFs is similar to that at 25 °C. There is an array of finger shape patterns, along the ring-like structure, towards the central region of the MNFs. The width of the coffee ring effect decreases with the increasing temperature. Moreover, when the temperature increases to 70 °C, there is an obvious gap region. At the central region, the other finger-like pattern is formed outward radially.

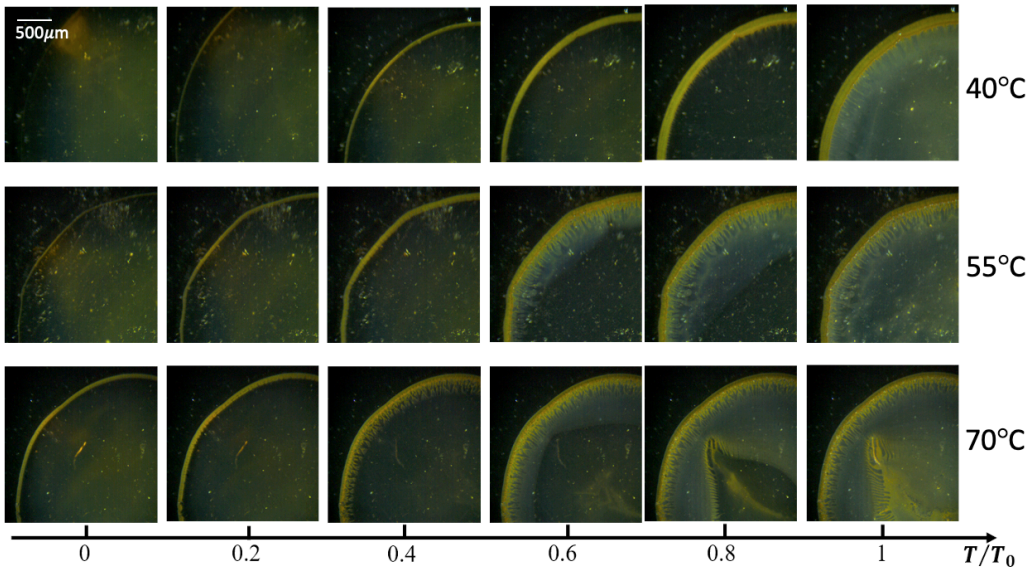


Figure 4. 10 Evaporation process of MNFs deposition patterns at the high-temperature range (40 °C, 55 °C, 70 °C).

4.4.2 Results and discussion for the mechanism of deposition patterns with substrate temperatures

To demonstrate the mechanism of pattern formations at different substrate temperatures, both the flow motion and the surface temperature distribution are analysed. In this study, 3.0 μm microbeads are used to track the trajectory of particles. The whole evaporation process is recorded by a high-speed camera (BASLER acA2040-90uc), which is mounted on the microscope (OPTIKA 400) from the top view. Meanwhile, a FLIR IR camera (SC7600M) is employed to analyse the effect of the temperature distribution along the droplet surface interface on deposition patterns. Deposition patterns are discussed from the low-temperature range to the high-temperature range.

Flow patterns and mechanism of microbead deposition at the low-temperature range (10 °C, 15 °C, and 20 °C).

At a low-temperature range (10 °C, 15 °C, and 20 °C), the surface temperature distribution of the droplet is shown in Figure 4.15. It is clear that the temperature along the contact line is higher than that at the apex along the air-liquid interface. The maximum temperature differences along the air-liquid interface are respectively 1.1 °C, 0.7 °C and 1.15 °C. Such differences are not big comparing to other temperature ranges. However, the evaporative rate at the edge is always the highest, which also drives the solvents from the central region flowing outwards to the contact line to compensate for the lost solvent (Figure 4.11). The substrate temperature is lower than the ambient temperature. Outward transport exists, but it is not intensive. In addition, four particles at the early stage are tracked in Figure 4.12. Particles at the central region follow a vortex flow.

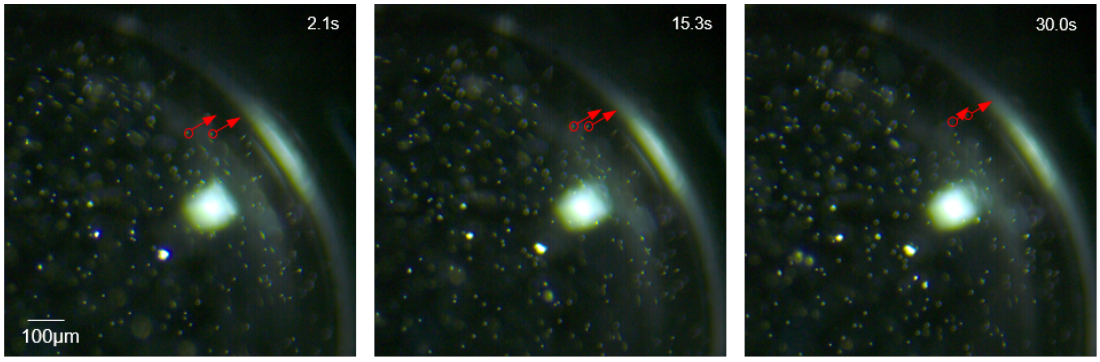


Figure 4. 11 Microbeads travel to the boundary along the air-liquid interface at the low temperature range.

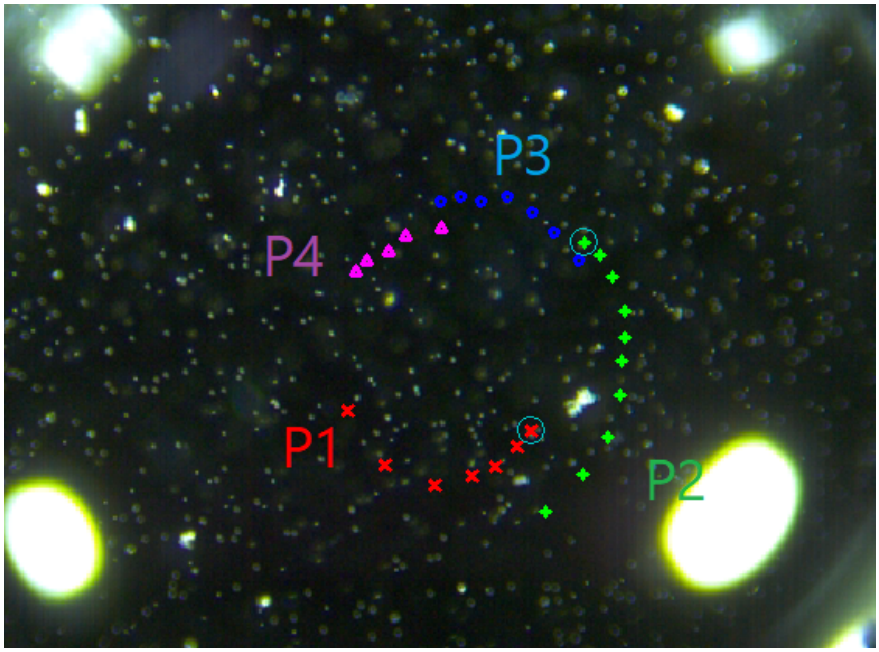


Figure 4. 12 Microbeads tracked at the central area at the early stage.

In terms of the heat transfer, the surface tension gradient is dependent on temperature gradients along the air-liquid interface, which is known as the Marangoni effect. Surface tension decreases as the temperature increases. The solvents always transport from the low surface tension to the high surface tension. Thus, according to the surface temperature distribution (Figure 4.15), the solvents are transported from the edge to the central region, which is also proved by the flow motion in Figure 4.13. Meanwhile, the central region is dominated by a vortex flow, which is driven by the Marangoni flow. The vortex flow impedes particles travelling to the central area.

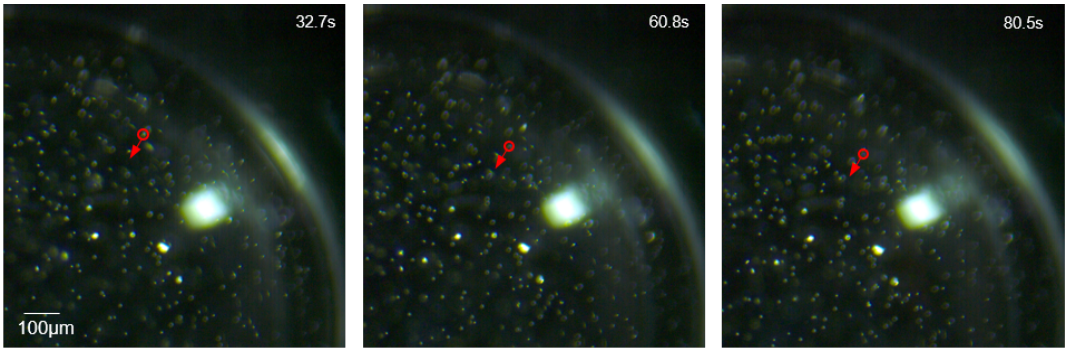


Figure 4. 13 Red marked microbead travel back from the edge along air-liquid interface at the middle stage.

Additionally, three microbeads are also marked as the target particles. When the evaporative time is at 313.4 s, there is nearly no movement in the radial direction (Figure 4.14). When the droplet almost dries up, no beads travel back towards the inward direction, and particles barely move. This is because the temperature difference along the air-liquid interface decreases over the evaporation process. The Marangoni effect also decreases with the decrease of the temperature difference, which causes particles to deposit on the substrate as the droplet evaporates.

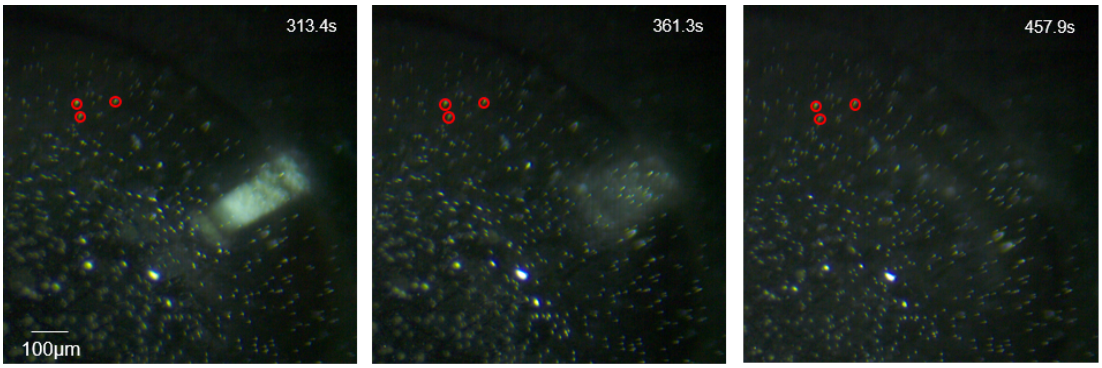


Figure 4. 14 Microbeads trajectories at the end of the evaporation.

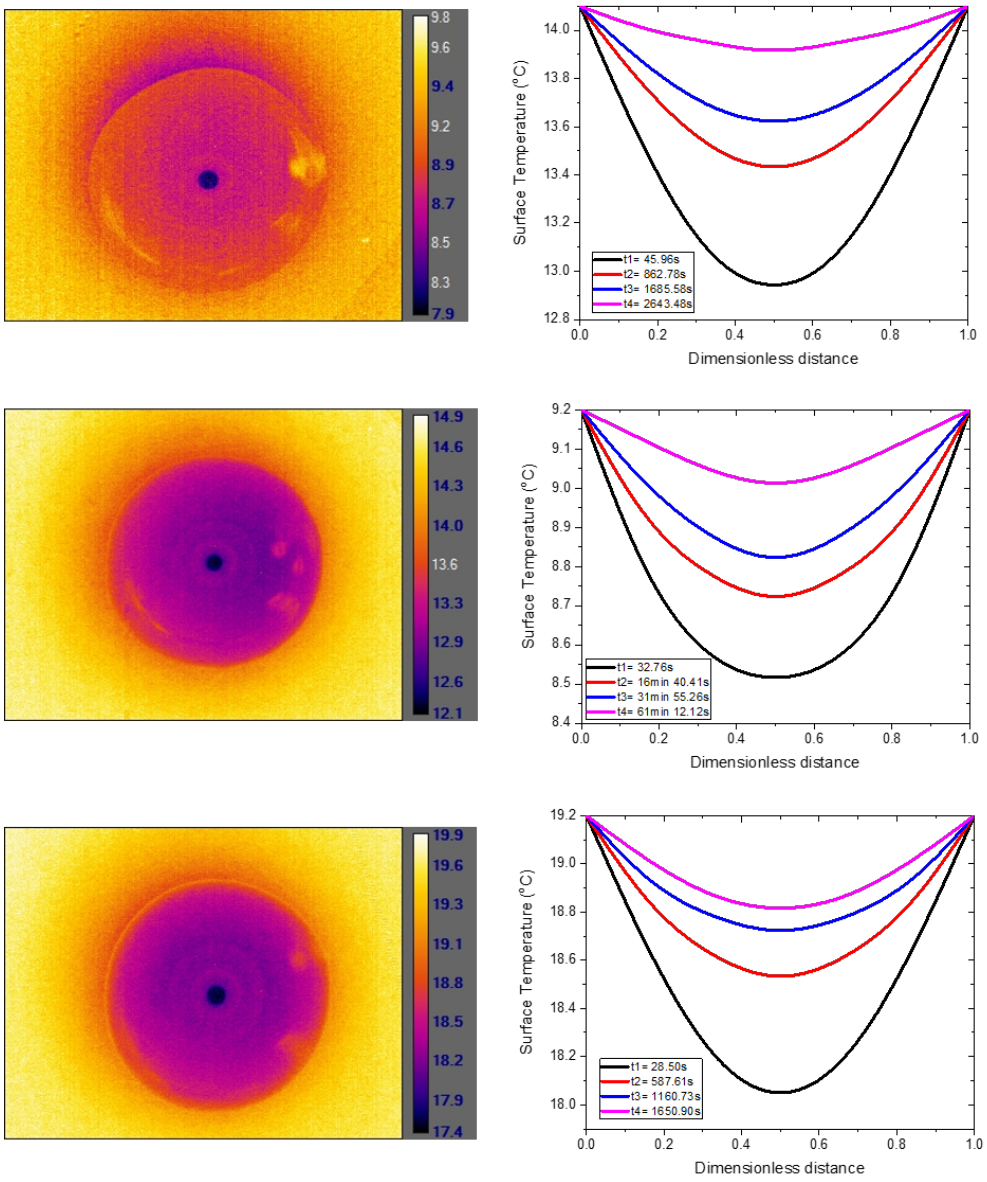


Figure 4. 15 Surface temperature distributions at the low-temperature range.

Therefore, according to the discussion above, the particle motion distribution at low temperatures can be divided into three stages. At the early stage, the motion of particles is dominated by the vortex flow due to the Marangoni flow at the central area, and there seems to be a boundary line between the central and the gap areas. When some particles escape from the centre to the gap, beads transport along the air-liquid surface to the edge due to the Marangoni effect. Both the outward transport and the Marangoni flow are not intensive. With the evaporation process,

the temperature difference decreases. In other words, in the middle stage, most particles are at the static state. Suspended particles distribute uniformly with the decrease of the height of the droplet. At the final stage, towards the end of the lifetime, beads travel back gently. The deposition pattern exhibits uniform on both the edge and the interior.

Flow patterns and mechanism of microbead deposition at 25 °C.

At 25 °C, at the early stage of the evaporation process, both central and gap regions are chaotic (Figure 4.16). At 185.0 s, the marked white particle moves irregularly over time, while other marked particles at the edge region travel outwards to the edge. In other words, the capillary flow dominates the outward flow trend in the edge region at this stage. According to the surface temperature distribution in Figure 4.19, the evaporation flux at the edge is higher than that at the central region, leading to more solvent loss at the boundary. The CCR mode occupies most of the lifetime, and particles are transported to the pinned contact line to compensate for the lost solvent.

When it comes to the second stage, at 225.3 s, the particles at the central region, as the green particle (Figure 4.16), become more orderly. Most particles follow a pair of counter-rotating vortices (Figure 4.17). The pair of counter-rotating vortices are at the central area in the colder regions and are essentially parallel to the horizontal plane. The strength of these vortices diminishes with time as the interface temperature is homogenized by the central stream of the warm fluid as well as by the heat being transported towards the cold vortices from the contact line due to both the conduction and the convection. Eventually, the vortices disappear, along with the preferential direction of the Marangoni convection. The drop reaches its

new quasi-steady equilibrium where the apex is in the coldest region, and the interface flow radially transports to the apex. Even though the capillary flow still dominates at the second stage (Figure 4.16), some particles flowing towards the edge are involved in counter-rotating vortices as P8 (Figure 4.17). Eventually, more particles travel back from the boundary region due to the Marangoni convection.

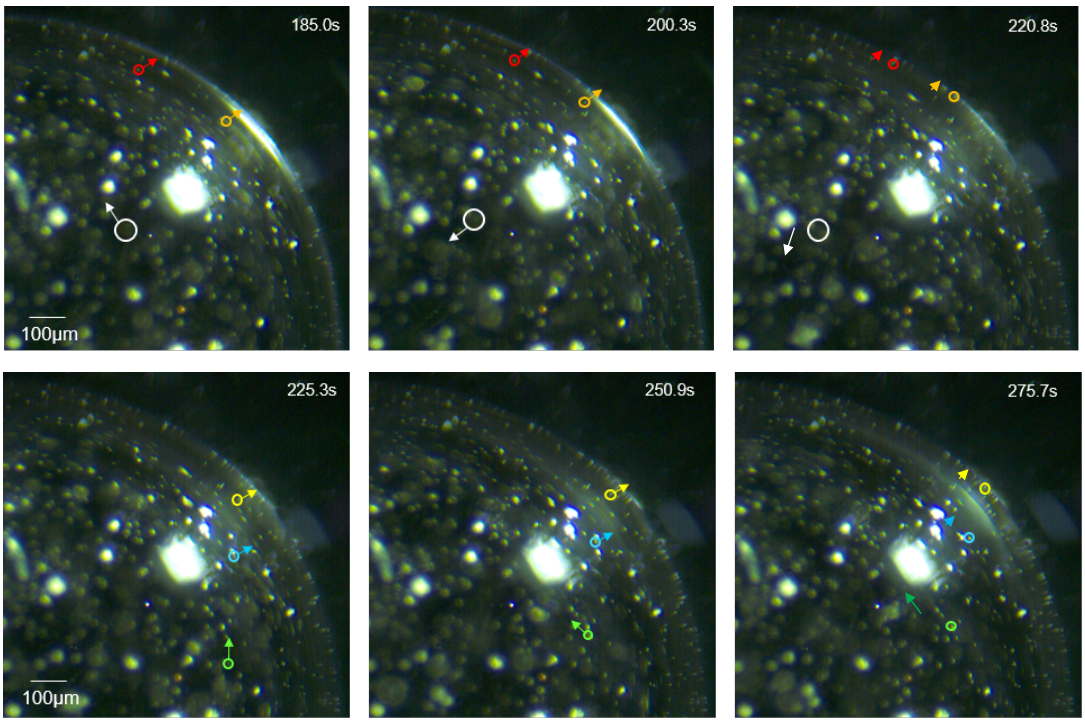


Figure 4. 16 Microbeads movement directions at 25 °C.

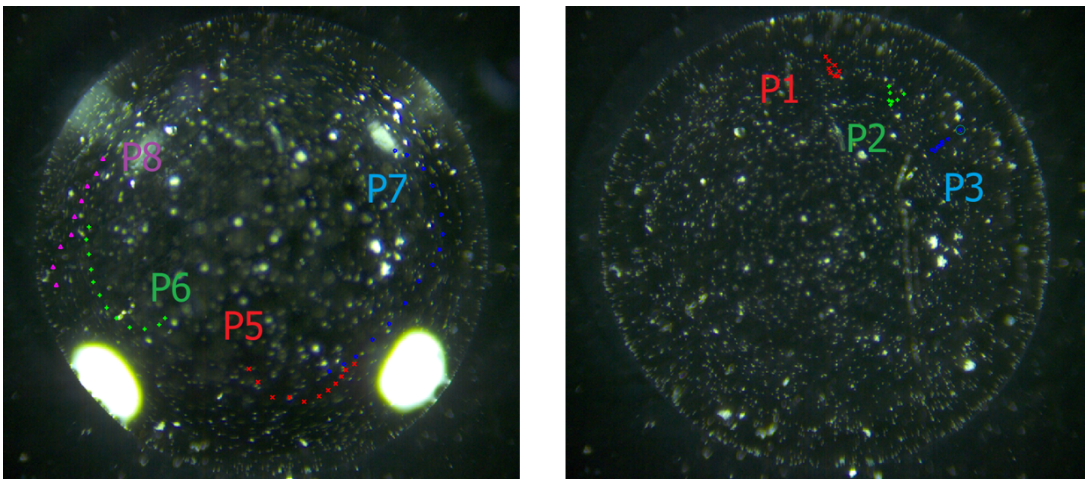


Figure 4. 17 Particles motion distribution at 25 °C.

At the final stage, the pair of counter-rotating vortices disappear, the capillary flow still dominates outward transport near the edge. The marked red particle shows that particles flow back from the boundary region to the central region. This is because the saline droplet reaches a new quasi-steady equilibrium when the vortices disappear with the preferential direction of the Marangoni convection. However, the temperature difference (Figure 4.19) still exists along the air-liquid interface. Eventually, the droplet deposition pattern presents a typical 'coffee-ring' pattern due to a dominant capillary flow. Meanwhile, particles in the central region are evenly distributed due to both the Marangoni convection and the Marangoni flow.

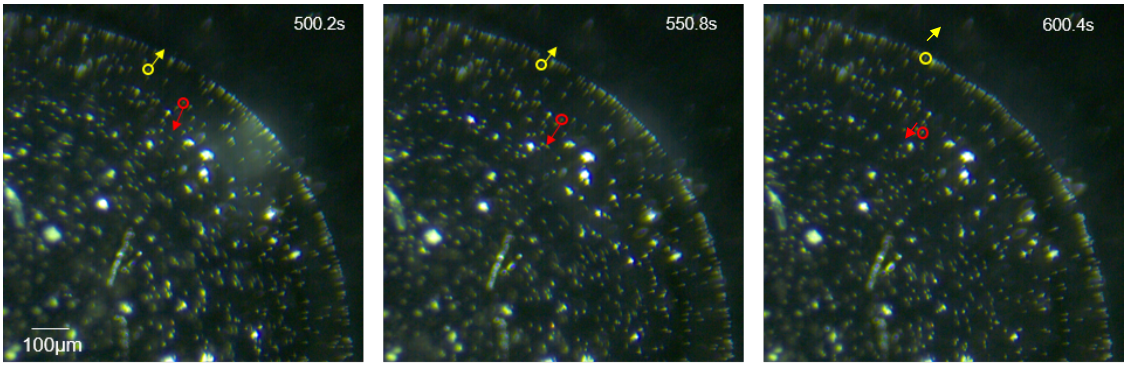


Figure 4. 18 Microbeads movement direction trends at the final stage at 25 °C.

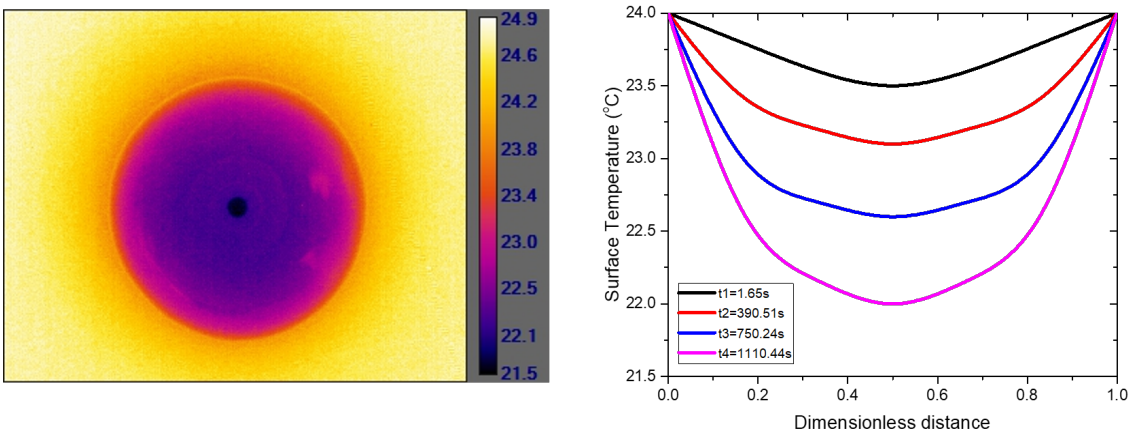


Figure 4. 19 Surface temperature distributions at 25 °C.

Flow patterns and mechanism of deposition at the high-temperature range

At the high-temperature range, the flow motion of particles is similar to that at 25 °C in the first two stages. At the early stage, the central region is chaotic, while the capillary flow dominates the edge and the gap region. However, the duration of the first stage is shorter than that at 25 °C, and the flow motion is more intensive. In the second stage, a pair of counter-rotating vortices flow at the central region due to the Marangoni convection. However, the process is not as intense as that at 25 °C while the capillary flow still dominates the edge and gap regions. Compared to that at the ambient temperature, the Marangoni flow exists at the boundary region due to a big temperature difference as shown in Figure 4.24. Some particles transported to the edge are also driven back to the central region along the air-liquid interface by the Marangoni flow as shown in Figure 4.21.

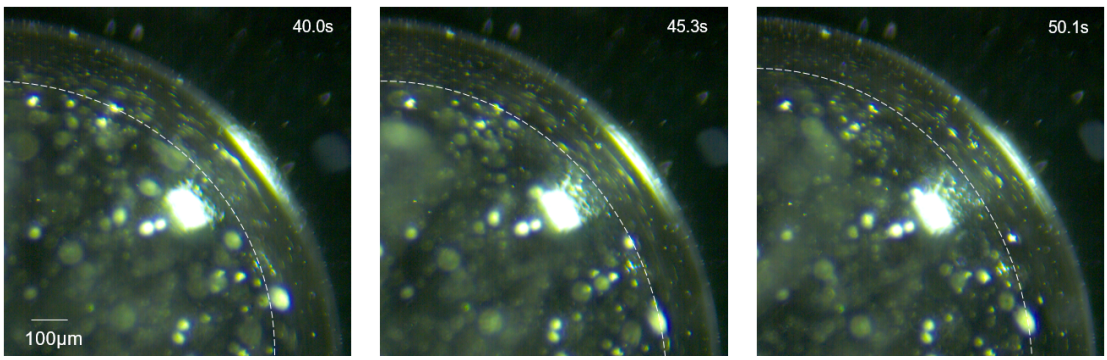


Figure 4. 20 Microbeads movement recording at the early stage of 55 °C.

In the final stage, at 90.8sec, a contra-rotating vortex disappears, as shown in Figure 4.21. A marked red particle travels towards the contact line, then goes back to the central region. Most of particles move radially as shown in Figure 4.22. This is because the temperature difference along the surface is still large enough to drive particles back to the central region radially with the increasing substrate

temperature. At this stage, both the Marangoni and the capillary flow contribute the self-circulation.

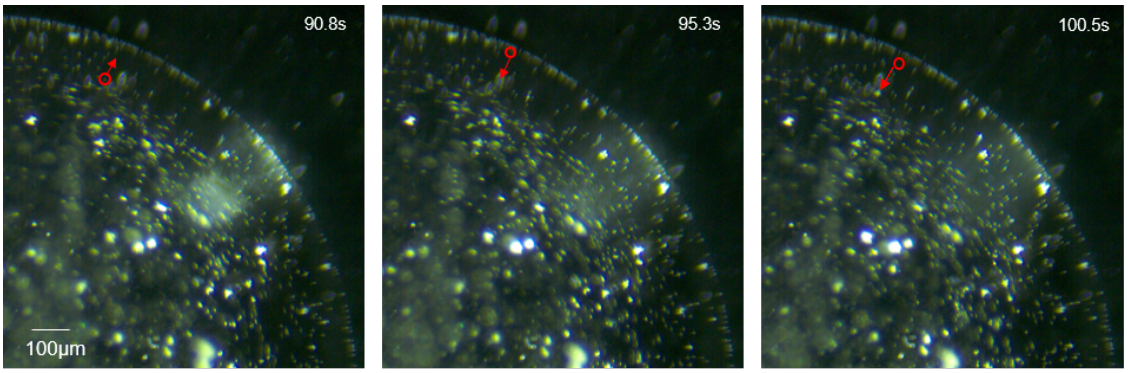


Figure 4. 21 Microbeads movement direction tracking at the middle stage of 55 °C.

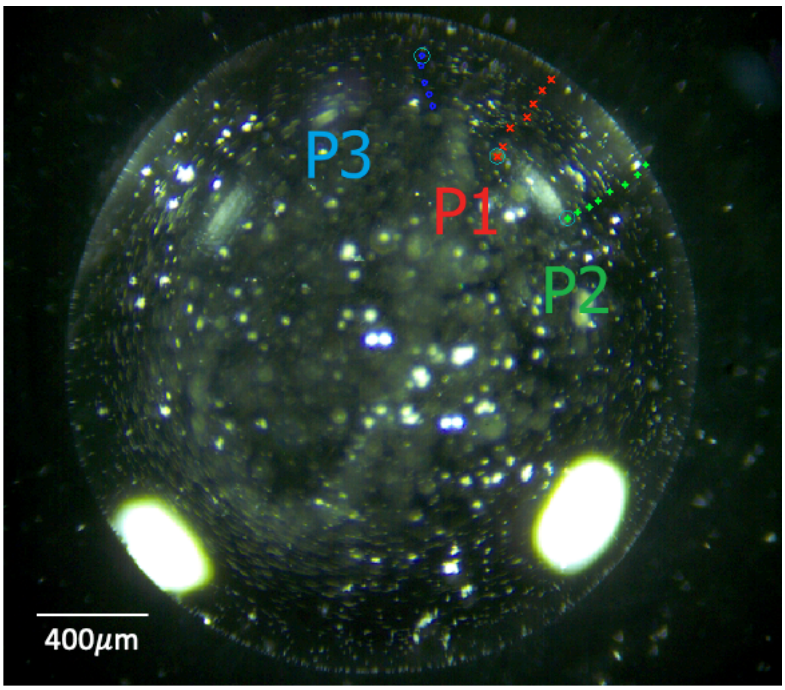


Figure 4. 22 Microbeads movement trajectory at the final stage of 55 °C.

When droplet almost dries up, the height of the droplet decreases over the evaporation time. During this period, the same amount of the liquid has to be squeezed through an area that is vanishing, leading to a sharp increase in the particle motion speed. Therefore, when the droplet almost evaporates, both the Marangoni

flow and the capillary flow are in the same layer close to the substrate. When the velocity is high enough, both inward and outward particles collide and accumulate in the gap region, eventually forming a secondary-ring pattern (Figure 4.23).

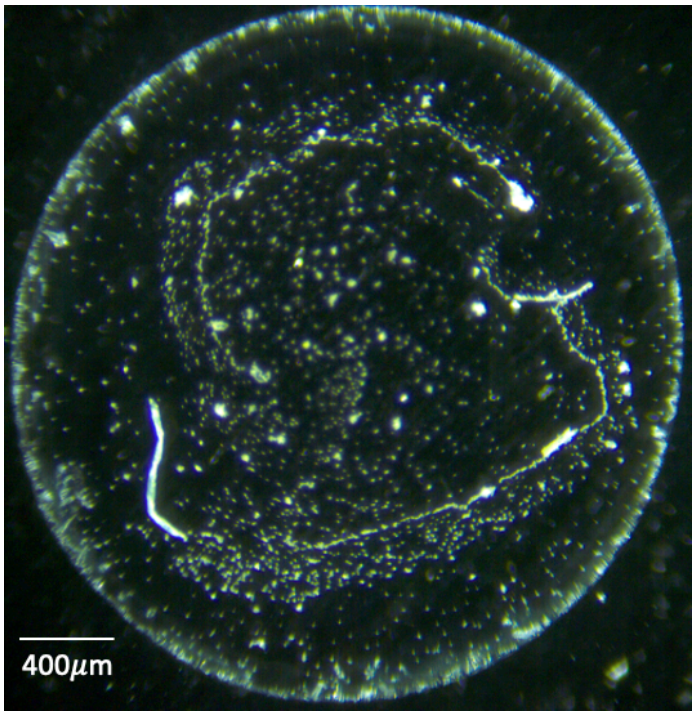


Figure 4. 23 Final pattern distribution of microbeads at 55 °C.

Therefore, the whole evaporation process at the high-temperature range can be divided into three stages. The first stage is similar to that at the ambient temperature, while the duration is much shorter. In the second stage, both the Marangoni and the capillary flow are intense at the edge and gap regions, outward transport still dominates at this stage. Meanwhile, a pair of the counter-rotating flowing in the central region distribute particles uniformly. In the final stage, the large temperature difference along interface makes the Marangoni flow the main factor for the dual ring formation.

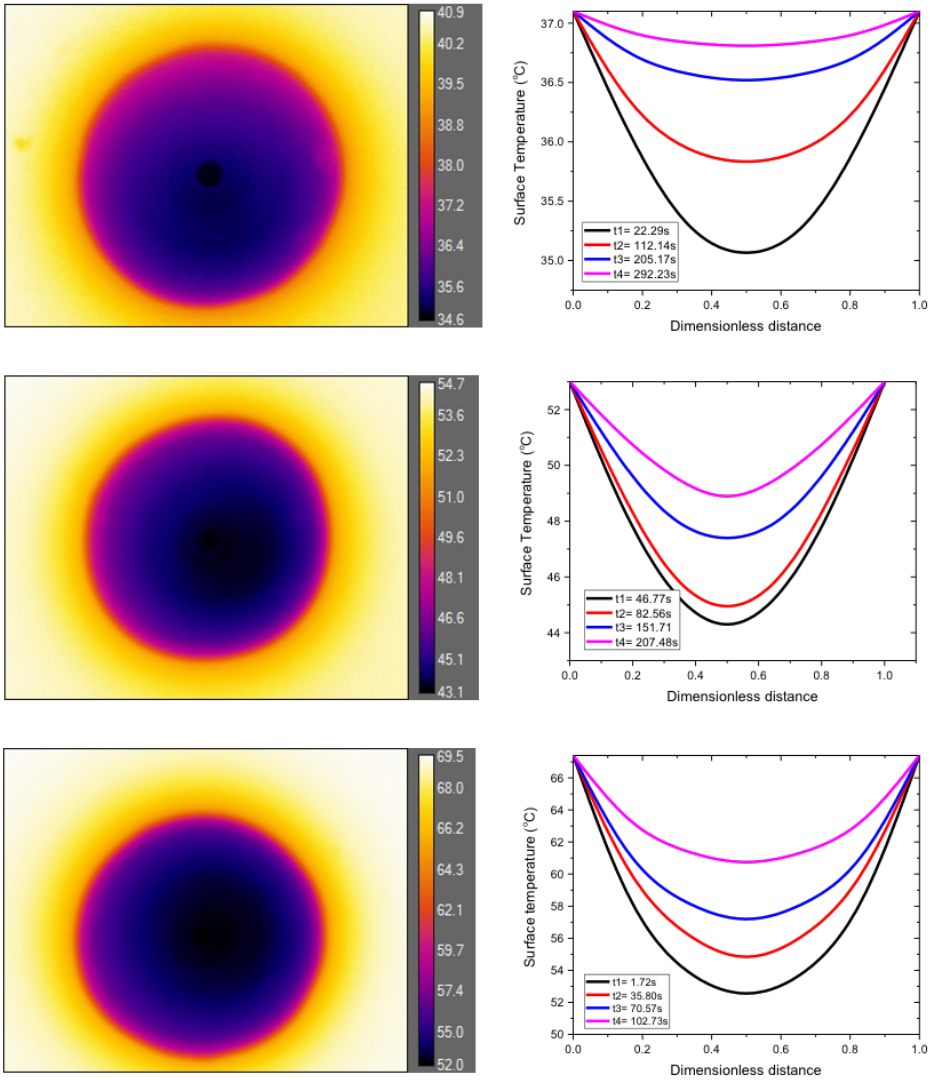


Figure 4. 24 Surface temperature distributions at the high-temperature range.

4.5 Results and Discussion for the Local Heating.

4.5.1 The properties of pattern formations for the local heating

To investigate heating directions, the evaporation process has been investigated on both hydrophilic and hydrophilic surfaces as shown in Figure 4.25. Generally, saline droplet evaporation process with various wettability can be divided into different modes, namely constant contact radius (CCR) mode, constant contact angle (CCA) mode and mixed mode. The mixed mode transits from the CCR mode

to the CCA mode. The CCR mode is an extreme case that a drop evaporates with a fixed contact line over the lifetime. Simultaneously, the contact angle decreases to adapt to the volume loss. For the CCA stage, it is an ideal condition that the contact line recedes with a constant contact angle. In terms of the mixed mode, it is closer to the actual condition. A drop starts to evaporate in the CCR mode where the contact line is pinned. The contact angle simultaneously decreases until it reaches the receding contact angle, at which point the contact line begins to slide. As shown in Figure 4.25, saline droplets are experimentally investigated with different degrees of wettability and the local heating respectively. Time is normalised by the lifetime, T/T_0, where T_0 is the time for complete evaporation, and T is the current evaporation time. All experimental results in four groups ((a), (b), (c), (d)) show that the CCR stage occupies most of the time, and T/T_0 is at around 0.8. This assists the solvents to transport to the edge.

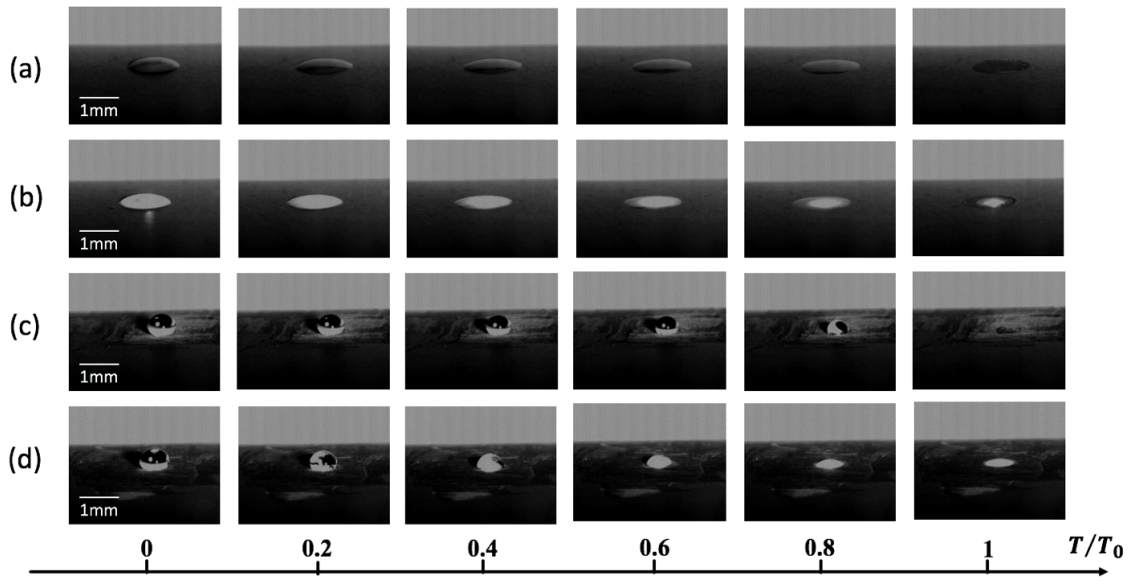


Figure 4. 25 Evaporation process from the substrate heating to the localized heating on the hydrophilic and the hydrophobic surfaces. (a) 2μL saline droplet heated from the substrate (hydrophilic surface). (b) 2μL saline droplet heated from the apex (hydrophilic surface). (c) 2μL saline droplet heated from substrate

(hydrophobic surface). (d) 2μL saline droplet process heated from apex (hydrophilic surface).

Figure 4.26 (a) and (b) compare the effect of both the local heating from apex and the substrate heating on the distribution of the saline deposition patterns on the same hydrophilic surface. In the experimental results of (a) and (b), the substrate heating shows a typical ring-like structure as shown in Figure 4.26 (a). When it comes to the local heating from the apex, the ring-like structure still exists, but the number of particles at the edge is reduced. A clear dot-like pattern appears at the heating point of the droplet centre as shown in Figure 4.26 (b).

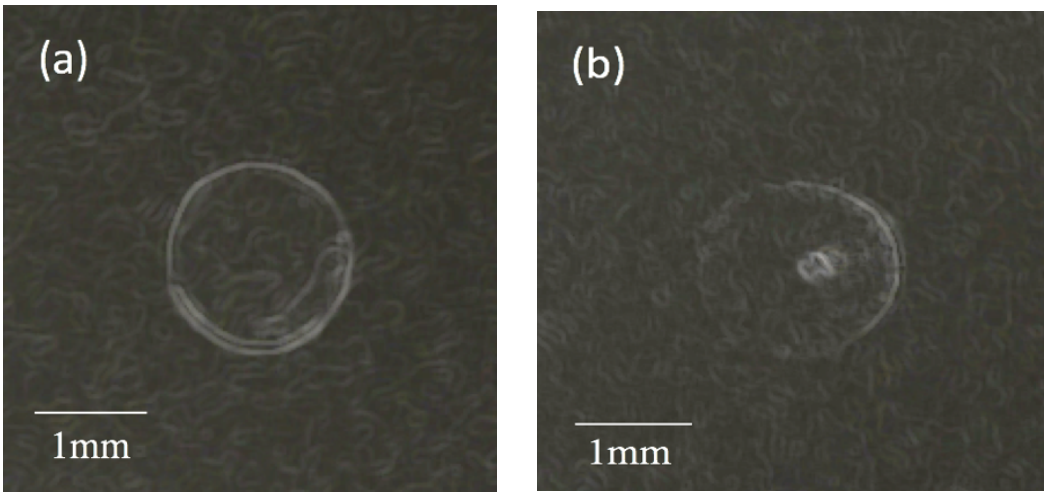


Figure 4. 26 Substrate and local heating of saline deposition patterns on the hydrophilic surface.

For the hydrophobic surface, compared to the hydrophilic one, the deposition patterns of the substrate heating show nearly similar results as the hydrophilic surface. Most saline particles assemble along the contact line as shown in Figure 4.27 (a). When it comes to the local heating from the apex, different degrees of wettability show different distributions. For the hydrophilic surface, most saline particles transport from the contact line to the central area, forming a dot-like deposition pattern, but barely saline particles are deposited between the edges and

the central region as shown in Figure 4.27 (b). On the hydrophobic surface, particles at the edge also tend to accumulate at the central area. However, many deposits are located between the boundary and the centre, which makes the pattern more uniform as shown in Figure 4.27 (b).

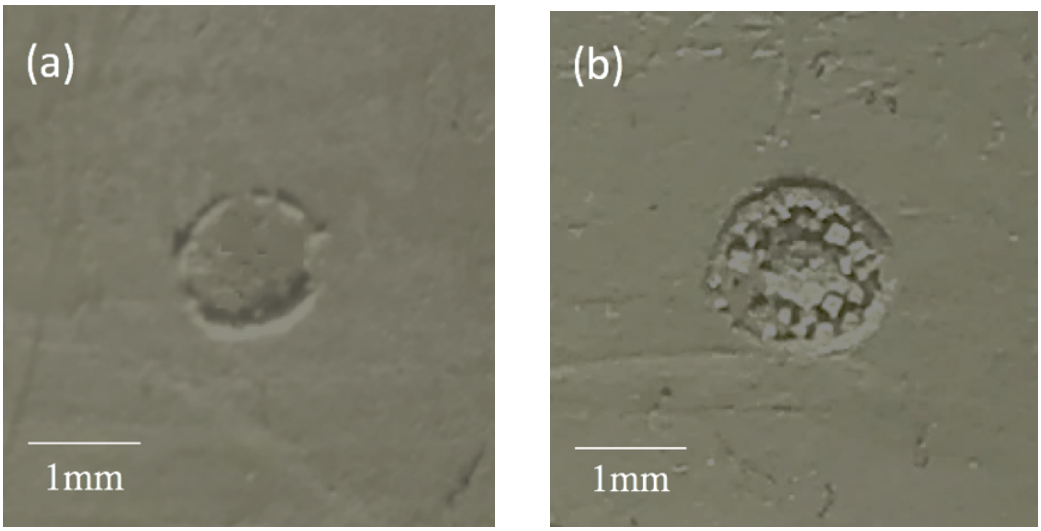


Figure 4. 27 Substrate and local heating of saline deposition patterns on the hydrophobic surface.

4.5.2 Results and analysis for the local heating

For the substrate heating, at 25 °C, the surface temperature distribution is shown in Figure 4.28. The experimental results show that there is an evident temperature gradient between the apex and the edge along the liquid-air interface throughout the evaporating process. Along the droplet surface, the apex of the droplet is always the coolest temperature point. In contrast, the surface temperature at the contact line is the highest temperature point, which leads to more solvents losing at the saline droplet edge than that at the central area. Meanwhile, the CCR mode occupies most of the evaporation process as T/T_0 is at around 0.8. Therefore, the boundary of the saline droplet is fixed on the contact line, which means that the saline solvents flow from the droplet centre towards the edge to compensate for the lost mass.

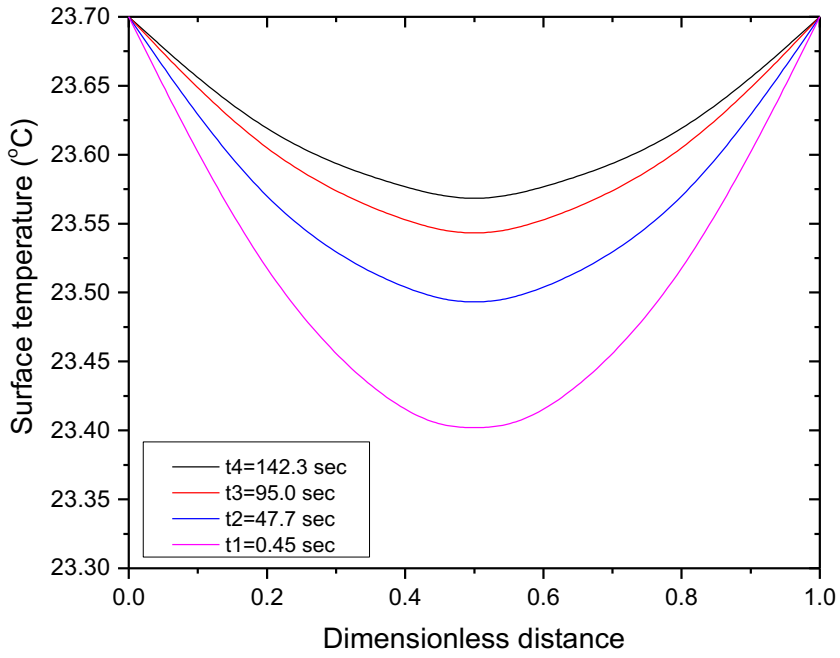


Figure 4. 28 Surface temperature distribution profiles of the substrate heating at 25 °C.

After complete evaporation, most solvents have already transported and deposited at the contact line, forming a ring-like deposition pattern (Figure 4.29 (a)). In this process, the flow behaviour also makes a great contribution based on the mass balance. The evaporation from the saline surface triggers the internal flow, meanwhile, the saline evaporation flow rate remains approximately constant over the evaporation process. Since the contact line needs to be replenished from the centre constantly, a steady flow towards the droplet edge is generated in the droplet. Moreover, the height of the saline droplet decreases due to the constant volume loss during the evaporation process. Therefore, the same amount of solvents has to squeeze through an area that is vanishing, inducing a diverging radial velocity. The "rush hour" behaviour is also regarded as having a great contribution to the coffee ring effect. It should be noticed that the variance of wettability has little effect for

the substrate heating case. This is because the temperature difference along the solid-liquid interface dominates saline radial flow motion, which transports the solvents from the central bottom to the boundary to compensate for the lost mass. In this process, although wettability can affect the flow along the air-liquid interface, it is weak. The flow motion near the air-liquid interface is mainly influenced by the capillary flow.

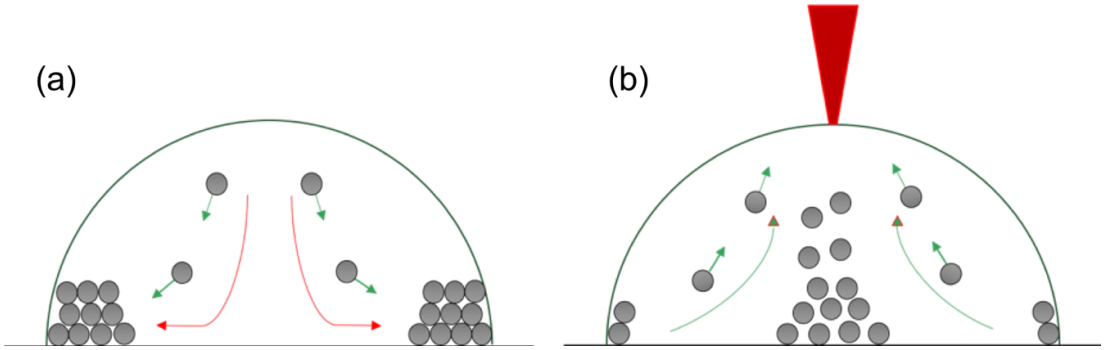


Figure 4. 29 Schematic diagrams for the mechanism of the coffee ring effect and reversing internal flow by the localized heating.

For the local heating, although there is an evident temperature difference along the liquid-air interface at 25 °C, the local heating allows the apex of saline droplets to absorb most of the energy. Therefore, the temperature at the contact line becomes the coolest, while the apex is the highest temperature point. Such temperature difference results in more solvents lost at the apex than that at other positions. More solvents must flow from the periphery to the apex to compensate as Figure 4.29 (b). Therefore, most solvents are hanging at the apex area over the evaporation process. With droplet height decreasing, compensated solutes drop down gradually, and most salts gather at the central area, forming a dot-like pattern. Eventually, surface temperature gradients cause the changes of the internal flow. Compared to the substrate heating conducted by other researchers [154, 179], with the transition of

deposition patterns from the ring-like structure to the dual ring and the uniform pattern, the local heating and the substrate heating both control the distribution of droplet deposition patterns by balancing the Marangoni flow and the capillary flow. However, the local heating shows more potential to actively control the distribution of deposit patterns than that of the substrate heating.

Moreover, in the case of the local heating, the Marangoni flow dominates the flow motion of the saline droplet due to the temperature difference along the air-liquid interface. Therefore, even though Deegan et al. [180] observed that the Marangoni flow was weak for water-based droplets, that does not mean factors affecting surface tension need to be ignored in the case of the local heating. Wettability, as a factor affecting surface tension, also needs to be considered. Surface tension is the tendency of fluid surfaces to shrink into the minimum surface which makes droplet tend to be spherical. Therefore, the surface area of the hydrophobic one is bigger than that of the hydrophilic one. The surface free energy increases with surface area, resulting in the increase of surface tension. On the other hand, the surface tension gradient also results from a temperature gradient. Surface tension of liquids decreases as the temperature increases. When the saline droplet is heated from the apex, molecules flow from the apex to the contact line along the air-liquid interface, which impedes the internal flow of saline droplets. To some extent, the Marangoni flow prevents the compensation for the evaporation loss at the apex. In this process, wettability and the local heating both make contributions to the Marangoni effect [181]. Therefore, on the hydrophobic surface, it is very likely that surface tension overcomes the internal flow, so that some particles are finally dispersed between

the edge and the centre, making the deposition pattern more uniform than that of the hydrophilic one.

4.6 Summary

In this chapter, two thermal strategies for controlling the distribution of deposit patterns have been presented. They are the substrate heating and the local heating.

For the substrate heating, experiments and mechanisms of droplet deposition patterns have been conducted, ranging from the low temperature to the high temperature. With the increase of the substrate temperature, the deposited patterns develop from the uniform pattern, the coffee ring structure to the dual-ring pattern. At the low-temperature range, the Marangoni flow plays an important role in the particle motion distribution. When the substrate temperature increases to 25 °C, the outward flow dominates the particle motion to compensate for the evaporation loss at the contact line. At the high-temperature range, both the radial outward flow and the Marangoni flow dominate the distribution of the deposition pattern at different stages. In addition, when it ultimately dries up, the 'rush hour' behaviour makes a contribution to the formation of the secondary ring that is formed at the gap area. This work highlights the effect of substrate temperatures on the deposition patterns, which potentially affects the distribution of particles.

In the local heating experiment, the distribution of droplet deposition patterns with both the local and the substrate heating on different wettability have been investigated. Experimental results show that evaporation starts from the CCR mode, then switches to the CCA mode. The CCR mode dominates the evaporation process. In the case of the substrate heating, the deposition patterns of salt exhibit the ring-like structure along the contact line on both the hydrophobic and the hydrophilic

surfaces. This mainly happens due to the compensation for the evaporation losses along the contact line. For the local heating, the drying pattern switches to the dot-like pattern by reversing the internal flow. For the hydrophilic surface, the Marangoni effect also needs to be considered. To some extent, surface tension can balance the internal flow induced by the localized heating from the apex even in water-based solutions. This work not only shows the potential to suppress the internal flow, but also makes the deposition pattern more uniform.

Chapter 5 Conclusions and Further Work

The subject of this work presents the properties of surfactant-free MNFs and thermal methods for controlling deposition patterns. Practical problems regarding the stability of MNFs, thermal properties of MNFs, and methods to control deposition patterns are experimentally investigated. Firstly, for the stability of MNFs, magnetic nanoparticles are synthesised by the co-precipitation method, and then modified with citric acid to improve the stabilization. The characterizations of MNPs are studied to verify the stability and their influencing factors. The thermal properties of MNFs include density, specific heat capacity, viscosity, thermal conductivity, and convective heat transfer. All these properties are compared with classical models. Moreover, the relationship between the stability and thermal properties is also analysed theoretically in this section. In addition, thermal strategies are applied to control the deposition patterns, including the substrate temperature and the local heating. The detailed conclusions and outlook for further work are presented in the following sections.

5.1 Properties of CA modified MNFs

In this work, the surfactant-free MNFs are obtained with predictable thermal physical properties. MNPs are modified with citric acid to stabilise them in the base liquid. The main finding of this work is that the colloidal stability of modified MNPs can be controlled by changing the pH value of the particle suspension. Moreover, most thermal properties can be explained by classical models. Following conclusions can be drawn from the experimental investigations:

1. The colloidal stability of modified particles is controlled by changing the pH values of the particle suspension. CA modified MNFs keep a good dispersion when the pH is controlled at the neutral values.
2. Properties of CA modified MNFs can be predicted by classical models. The density of nanofluids at a certain concentration can be predicted accurately by the mixing theory, and the specific heat of nanofluids can be predicted by the thermal equilibrium model.
3. After the colloidal stability is optimized, the viscosity of MNFs exhibits Newtonian behaviour, despite of the variance in the particle concentration and the temperature. The viscosity increases almost linearly with the particle concentration, which can be explained by the Krieger and Dougherty model.
4. The thermal conductivity of nanofluids can be generally predicted by the Maxwell model, but at a certain particle concentration, thermal conductivity is higher than that predicted by the Maxwell model due to the proper aggregation.
5. The convective heat transfer coefficient is found to be enhanced by over 10% for Re > 2500, which should be explained by the particle migration.

The MNFs prepared in this work are controlled at a low concentration. Even though thermal properties of MNFs can be predicted by classical models at the low concentration, higher particle concentrations and Reynold number still need to be investigated in the future to verify the models. Moreover, well-dispersed MNFs should be further tested in practical applications.

5.2 Droplet Deposition Patterns affected by Thermal Strategies

In this work, the distribution of deposition patterns is experimentally controlled by the substrate heating and the local heating. For the substrate heating, both saline and MNFs droplets are experimentally studied. The substrate temperatures are set from 10 °C to 70 °C. Drying patterns transit from the uniform pattern, the coffee ring pattern to the dual-ring pattern with the increase of substrate temperatures. The capillary and the Marangoni flows play an important role in the evaporation process. For the local heating, the deposition patterns are studied by both the local and the substrate heating with different wettability. The laser-induced local heating drives particle deposition patterns from the ring-like to the dot-like patterns by reversing the internal flow. The following results can be obtained.

1. At the low-temperature range, the distribution of the pattern formation exhibits a uniform pattern. The Marangoni flow plays an important role in the particle motion distribution.
2. At the ambient temperature, the distribution of the pattern formation exhibits a ring-like structure. Outward flow dominates the particle motion to compensate for the evaporation loss at the contact line.
3. At the high-temperature range, the distribution of the pattern formation exhibits a dual ring pattern. Both the capillary and the Marangoni flows control the distribution of the deposition pattern during different evaporation periods.
4. For the local heating, the distribution of the pattern formation exhibits a dot-like structure. The capillary flow makes an important contribution to the reversing flow. In addition, the Marangoni effect should be considered in

the hydrophobic surface. Surface tension can balance the internal flows by the local heating at the apex.

5. For the hydrophilic surface, droplet evaporation transits from the CCR mode to the CCA mode, and the CCR stage dominates the evaporation period. For the hydrophobic surface, the Marangoni flow also makes a contribution to the drying formation. The surface free energy increases with the increase of the surface area, resulting in the increase of surface tension.

For the future outlook of this work, firstly, the PIV technique should be further conducted to capture details at the high-temperature range. Then, for the local heating, the present test rig cannot apply the heater, the CCD camera and the IR camera simultaneously. Experimental setup still needs to be upgraded in the future work.

Reference

1. Chol, S., *Enhancing thermal conductivity of fluids with nanoparticles.* ASME-Publications-Fed, 1995. **231**: p. 99-106.
2. Bahiraei, M. and M. Hangi, *Flow and heat transfer characteristics of magnetic nanofluids: A review.* Journal of Magnetism and Magnetic Materials, 2015. **374**: p. 125-138.
3. Nkurikiyimfura, I., Y. Wang, and Z. Pan, *Heat transfer enhancement by magnetic nanofluids—A review.* Renewable and Sustainable Energy Reviews, 2013. **21**: p. 548-561.
4. Odenbach, S., *Ferrofluids: magnetically controllable fluids and their applications*. Vol. 594. 2008: Springer.
5. Li, Q. and Y. Xuan, *Experimental investigation on heat transfer characteristics of magnetic fluid flow around a fine wire under the influence of an external magnetic field.* Experimental Thermal and Fluid Science, 2009. **33**(4): p. 591-596.
6. Afifah, A.N., S. Syahrullail, and N.A.C. Sidik, *Magnetoviscous effect and thermomagnetic convection of magnetic fluid: A review.* Renewable and Sustainable Energy Reviews, 2016. **55**: p. 1030-1040.
7. Chiu, Y.P., et al., *Specific heat of magnetic fluids under a modulated magnetic field.* J. Appl. Phys., 2003. **93**(4): p. 2079-2081.
8. Azizian, R., et al., *Effect of magnetic field on laminar convective heat transfer of magnetite nanofluids.* International Journal of Heat and Mass Transfer, 2014. **68**: p. 94-109.
9. Mousavi, S.M., et al., *Heat transfer enhancement of ferrofluid flow within a wavy channel by applying a non-uniform magnetic field.* Journal of Thermal Analysis and Calorimetry, 2020. **139**(5): p. 3331-3343.

10. De Heer, W.A., A. Chatelain, and D. Ugarte, *A carbon nanotube field-emission electron source.* Science, 1995. **270**(5239): p. 1179-1181.

11. Bozhko, A. and G. Putin, *Thermomagnetic convection as a tool for heat and mass transfer control in nanosize materials under microgravity conditions.* Microgravity Science and Technology, 2009. **21**(1-2): p. 89-93.

12. Dutz, S. and R. Hergt, *Magnetic particle hyperthermia—a promising tumour therapy?* Nanotechnology, 2014. **25**(45): p. 452001.

13. Warzoha, R.J. and A.S. Fleischer, *Heat flow at nanoparticle interfaces.* Nano Energy, 2014. **6**: p. 137-158.

14. Prasher, R., et al., *Effect of aggregation on thermal conduction in colloidal nanofluids.* Applied Physics Letters, 2006. **89**(14): p. 143119.

15. Li, Q., Y. Xuan, and J. Wang, *Experimental investigations on transport properties of magnetic fluids.* Experimental Thermal and Fluid Science, 2005. **30**(2): p. 109-116.

16. Krichler, M. and S. Odenbach, *Thermal conductivity measurements on ferrofluids with special reference to measuring arrangement.* Journal of Magnetism and Magnetic Materials, 2013. **326**(0): p. 85-90.

17. Bigdeli, M.B., et al., *A review on the heat and mass transfer phenomena in nanofluid coolants with special focus on automotive applications.* Renewable and Sustainable Energy Reviews, 2016. **60**: p. 1615-1633.

18. Duan, F., D. Kwek, and A. Crivoi, *Viscosity affected by nanoparticle aggregation in Al2O3-water nanofluids.* Nanoscale Res. Lett., 2011. **6**(1): p. 248.

19. Hong, J. and D. Kim, *Effects of aggregation on the thermal conductivity of alumina/water nanofluids.* Thermochimica acta, 2012. **542**: p. 28-32.

20. Nwosu, P.N., J. Meyer, and M. Sharifpur, *A Review and Parametric Investigation Into Nanofluid Viscosity Models.* J Nanotechnol Eng Med, 2014. **5**(3): p. 031008-031008.

21. Zhou, S.-Q., R. Ni, and D. Funfschilling, *Effects of shear rate and temperature on viscosity of alumina polyalphaolefins nanofluids.* J. Appl. Phys., 2010. **107**(5): p. 054317.

22. Pastoriza-Gallego, M.J., et al., *Rheological non-Newtonian behaviour of ethylene glycol-based Fe2O3 nanofluids.* Nanoscale Res. Lett., 2011. **6**(1): p. 560.

23. Yu, W., et al., *Experimental investigation on thermal conductivity and viscosity of aluminum nitride nanofluid.* Particuology, 2011. **9**(2): p. 187-191.

24. Kulkarni, D.P., D.K. Das, and G.A. Chukwu, *Temperature dependent rheological property of copper oxide nanoparticles suspension.* J. Nanosci. Nanotechnol. , 2006. **6**: p. 1150–1154.

25. Chen, H., et al., *Rheological behaviour of ethylene glycol-titanate nanotube nanofluids.* J. Nanopart. Res., 2009. **11**(6): p. 1513.

26. Sharma, A.K., A.K. Tiwari, and A.R. Dixit, *Rheological behaviour of nanofluids: A review.* Renew. Sustainable Energy Rev., 2016. **53**: p. 779-791.

27. Faraudo, J., J.S. Andreu, and J. Camacho, *Understanding diluted dispersions of superparamagnetic particles under strong magnetic fields: a review of concepts, theory and simulations.* Soft Matter, 2013. **9**(29): p. 6654-6664.

28. Zhuang, J., et al., *Supercrystalline Colloidal Particles from Artificial Atoms.* J. Am. Chem. Soc., 2007. **129**(46): p. 14166-14167.

29. Qazi, M.J., et al., *Influence of surfactants on sodium chloride crystallization in confinement.* Langmuir, 2017. **33**(17): p. 4260-4268.

30. Wei, X., et al., *Comparison investigation of the effects of ionic surfactants on the crystallization behavior of calcium oxalate: From cationic to anionic surfactant.* Colloids and Surfaces A: Physicochemical and Engineering Aspects, 2012. **401**: p. 107-115.

31. Soltman, D. and V. Subramanian, *Inkjet-printed line morphologies and temperature control of the coffee ring effect.* Langmuir, 2008. **24**(5): p. 2224-2231.

32. Singh, M., et al., *Inkjet printing—process and its applications.* Advanced materials, 2010. **22**(6): p. 673-685.

33. Teichler, A., J. Perelaer, and U.S. Schubert, *Inkjet printing of organic electronics–comparison of deposition techniques and state-of-the-art developments.* Journal of Materials Chemistry C, 2013. **1**(10): p. 1910-1925.

34. Ramaswamy, S. and T.R. Golub, *DNA microarrays in clinical oncology.* Journal of clinical oncology, 2002. **20**(7): p. 1932-1941.

35. Hu, H. and R.G. Larson, *Marangoni effect reverses coffee-ring depositions.* The Journal of Physical Chemistry B, 2006. **110**(14): p. 7090-7094.

36. Deegan, R.D., *Pattern formation in drying drops.* Physical review E, 2000. **61**(1): p. 475.

37. Sefiane, K., *Patterns from drying drops.* Advances in colloid and interface science, 2014. **206**: p. 372-381.

38. Zhong, X., A. Crivoi, and F. Duan, *Sessile nanofluid droplet drying.* Advances in colloid and interface science, 2015. **217**: p. 13-30.

39. Deegan, R.D., et al., *Capillary flow as the cause of ring stains from dried liquid drops.* Nature, 1997. **389**(6653): p. 827.

40. Brutin, D. and V. Starov, *Recent advances in droplet wetting and evaporation.* Chemical Society Reviews, 2018. **47**(2): p. 558-585.

41. Kordás, K., et al., *Inkjet printing of electrically conductive patterns of carbon nanotubes.* Small, 2006. **2**(8-9): p. 1021-1025.

42. Brutin, D., et al., *Pattern formation in drying drops of blood.* Journal of fluid mechanics, 2011. **667**: p. 85-95.

43. Shimoni, A., S. Azoubel, and S. Magdassi, *Inkjet printing of flexible high-performance carbon nanotube transparent conductive films by "coffee ring effect".* Nanoscale, 2014. **6**(19): p. 11084-11089.

44. Huang, Z., et al., *Rapid and nondestructive method for evaluation of embryo culture media using drop coating deposition Raman spectroscopy.* Journal of Biomedical Optics, 2013. **18**(12): p. 127003.

45. Kanai, T. and T. Sawada, *New route to produce dry colloidal crystals without cracks.* Langmuir, 2009. **25**(23): p. 13315-13317.

46. Brutin, D., *Droplet wetting and evaporation: from pure to complex fluids*. 2015: Academic Press.

47. Chhasatia, V.H., A.S. Joshi, and Y. Sun, *Effect of relative humidity on contact angle and particle deposition morphology of an evaporating colloidal drop.* Applied Physics Letters, 2010. **97**(23): p. 231909.

48. Bhardwaj, R., et al., *Self-assembly of colloidal particles from evaporating droplets: role of DLVO interactions and proposition of a phase diagram.* Langmuir, 2010. **26**(11): p. 7833-7842.

49. Kim, H., et al., *Controlled uniform coating from the interplay of Marangoni flows and surface-adsorbed macromolecules.* Physical review letters, 2016. **116**(12): p. 124501.

50. Brutin, D., *Influence of relative humidity and nano-particle concentration on pattern formation and evaporation rate of pinned drying drops of nanofluids.* Colloids and Surfaces A: Physicochemical and Engineering Aspects, 2013. **429**: p. 112-120.

51. Evans, W., et al., *Effect of aggregation and interfacial thermal resistance on thermal conductivity of nanocomposites and colloidal nanofluids.* International Journal of Heat and Mass Transfer, 2008. **51**(5): p. 1431-1438.

52. Akoh, H., et al., *Magnetic properties of ferromagnetic ultrafine particles prepared by vacuum evaporation on running oil substrate.* Journal of Crystal Growth, 1978. **45**: p. 495-500.

53. Tsuji, T., et al., *Preparation of silver nanoparticles by laser ablation in solution: influence of laser wavelength on particle size.* Applied Surface Science, 2002. **202**(1): p. 80-85.

54. Mafune, F., et al., *Structure and stability of silver nanoparticles in aqueous solution produced by laser ablation.* The Journal of Physical Chemistry B, 2000. **104**(35): p. 8333-8337.

55. Lu, A.-H., E.L. Salabas, and F. Schüth, *Magnetic Nanoparticles: Synthesis, Protection, Functionalization, and Application.* Angew. Chem. Int. Ed., 2007. **46**(8): p. 1222-1244.

56. Bee, A., R. Massart, and S. Neveu, *Synthesis of very fine maghemite particles.* Journal of Magnetism and Magnetic Materials, 1995. **149**(1): p. 6-9.

57. Vekas, L., D. Bica, and M.V. Avdeev, *Magnetic nanoparticles and concentrated magnetic nanofluids: synthesis, properties and some applications.* China Particuology, 2007. **5**(1): p. 43-49.

58. Hanh, N., et al., *Synthesis of cobalt ferrite nanocrystallites by the forced hydrolysis method and investigation of their magnetic properties.* Physica B: Condensed Matter, 2003. **327**(2–4): p. 382-384.

59. Maaz, K., et al., *Synthesis and magnetic properties of cobalt ferrite (CoFe2O4) nanoparticles prepared by wet chemical route.* J. Magn. Magn. Mater., 2007. **308**(2): p. 289-295.

60. Syam Sundar, L., et al., *Viscosity of low volume concentrations of magnetic Fe3O4 nanoparticles dispersed in ethylene glycol and water mixture.* Chemical Physics Letters, 2012. **554**: p. 236-242.

61. de Sousa, M.E., et al., *Stability and Relaxation Mechanisms of Citric Acid Coated Magnetite Nanoparticles for Magnetic Hyperthermia.* J. Phys. Chem. C, 2013. **117**(10): p. 5436-5445.

62. Campelj, S., D. Makovec, and M. Drofenik, *Preparation and properties of water-based magnetic fluids.* J. Phys.: Condens. Matter, 2008. **20**(20): p. 204101.

63. Nigam, S., K.C. Barick, and D. Bahadur, *Development of citrate-stabilized Fe3O4 nanoparticles: Conjugation and release of doxorubicin for therapeutic applications.* J. Magn. Magn. Mater, 2011. **323**(2): p. 237-243.

64. Mikhaylova, M., et al., *BSA Immobilization on Amine-Functionalized Superparamagnetic Iron Oxide Nanoparticles.* Chemistry of Materials, 2004. **16**(12): p. 2344-2354.

65. Sahoo, Y., et al., *Alkyl Phosphonate/Phosphate Coating on Magnetite Nanoparticles: A Comparison with Fatty Acids.* Langmuir, 2001. **17**(25): p. 7907-7911.

66. Devendiran, D.K. and V.A. Amirtham, *A review on preparation, characterization, properties and applications of nanofluids.* Renewable and Sustainable Energy Reviews, 2016. **60**: p. 21-40.

67. Haisheng, C., D. Yulong, and T. Chunqing, *Rheological behaviour of nanofluids.* New J. Phys, 2007. **9**(10): p. 367.

68. Xuan, Y. and Q. Li, *Heat transfer enhancement of nanofluids.* International Journal of heat and fluid flow, 2000. **21**(1): p. 58-64.

69. Salentinig, S., L. Sagalowicz, and O. Glatter, *Self-assembled structures and p K a value of oleic acid in systems of biological relevance.* Langmuir, 2010. **26**(14): p. 11670-11679.

70. Verwey, E.J.W. and J.T.G. Overbeek, *Theory of the stability of lyophobic colloids*. 1948: Amsterdam : Elsevier.

71. Derjaguin, B.V., N.V. Churaev, and V.M. Muller, *The Derjaguin—Landau—Verwey—Overbeek (DLVO) Theory of Stability of Lyophobic Colloids*, in *Surface Forces*. 1987, Springer US: Boston, MA. p. 293-310.

72. Pak, B.C. and Y.I. Cho, *HYDRODYNAMIC AND HEAT TRANSFER STUDY OF DISPERSED FLUIDS WITH SUBMICRON METALLIC OXIDE PARTICLES.* Experimental Heat Transfer, 1998. **11**(2): p. 151-170.

73. Servati V, A.A., K. Javaherdeh, and H.R. Ashorynejad, *Magnetic field effects on force convection flow of a nanofluid in a channel partially filled with porous media using Lattice Boltzmann Method.* Advanced Powder Technology, 2014. **25**(2): p. 666-675.

74. Vajjha, R.S., D.K. Das, and B.M. Mahagaonkar, *Density Measurement of Different Nanofluids and Their Comparison With Theory.* Petroleum Science and Technology, 2009. **27**(6): p. 612-624.

75. Pastoriza-Gallego, M.J., et al., *Enhancement of thermal conductivity and volumetric behavior of FexOy nanofluids.* J. Appl. Phys., 2011. **110**(1): p. 014309.

76. Das, S.K., et al., *Temperature Dependence of Thermal Conductivity Enhancement for Nanofluids.* Journal of Heat Transfer, 2003. **125**(4): p. 567-574.

77. Murshed, S.M.S., K.C. Leong, and C. Yang, *Determination of the effective thermal diffusivity of nanofluids by the double hot-wire technique.* Journal of Physics D: Applied Physics, 2006. **39**(24): p. 5316.

78. Venerus, D.C., et al., *Study of thermal transport in nanoparticle suspensions using forced Rayleigh scattering.* Journal of Applied Physics, 2006. **100**(9): p. 094310.

79. Wen, D. and Y. Ding, *Experimental investigation into convective heat transfer of nanofluids at the entrance region under laminar flow conditions.* International Journal of Heat and Mass Transfer, 2004. **47**(24): p. 5181-5188.

80. Ding, Y., et al., *Heat transfer of aqueous suspensions of carbon nanotubes (CNT nanofluids).* International Journal of Heat and Mass Transfer, 2006. **49**(1–2): p. 240-250.

81. Wen, D. and Y. Ding, *Formulation of nanofluids for natural convective heat transfer applications.* International Journal of Heat and Fluid Flow, 2005. **26**(6): p. 855-864.

82. Nnanna, A.G., *Experimental Model of Temperature-Driven Nanofluid.* Journal of Heat Transfer, 2006. **129**(6): p. 697-704.

83. Buongiorno, J., *Convective Transport in Nanofluids.* Journal of Heat Transfer, 2005. **128**(3): p. 240-250.

84. Zhou, S.-Q. and R. Ni, *Measurement of the specific heat capacity of water-based Al2O3 nanofluid.* Appl. Phys. Lett., 2008. **92**(9): p. 093123.

85. De Robertis, E., et al., *Application of the modulated temperature differential scanning calorimetry technique for the determination of the specific heat of copper nanofluids.* Applied Thermal Engineering, 2012. **41**: p. 10-17.

86. Elias, M.M., et al., *Experimental investigation on the thermo-physical properties of Al2O3 nanoparticles suspended in car radiator coolant.* International Communications in Heat and Mass Transfer, 2014. **54**: p. 48-53.

87. Shahrul, I.M., et al., *A comparative review on the specific heat of nanofluids for energy perspective.* Renew. Sustainable Energy Rev., 2014. **38**: p. 88-98.

88. Kumaresan, V. and R. Velraj, *Experimental investigation of the thermo-physical properties of water–ethylene glycol mixture based CNT nanofluids.* Thermochimica Acta, 2012. **545**: p. 180-186.

89. Saeedinia, M., M.A. Akhavan-Behabadi, and P. Razi, *Thermal and rheological characteristics of CuO–Base oil nanofluid flow inside a circular tube.* Int. Commun. Heat MassTransf., 2012. **39**(1): p. 152-159.

90. Wang, B.-X., L.-P. Zhou, and X.-F. Peng, *Surface and Size Effects on the Specific Heat Capacity of Nanoparticles.* Int. J. Thermophys., 2006. **27**(1): p. 139-151.

91. He, Q., et al., *Experimental study on thermophysical properties of nanofluids as phase-change material (PCM) in low temperature cool storage.* Energy Conversion and Management, 2012. **64**: p. 199-205.

92. Xuan, Y. and W. Roetzel, *Conceptions for heat transfer correlation of nanofluids.* Int. J. Heat MassTransfer, 2000. **43**(19): p. 3701-3707.

93. Avsec, J. and M. Oblak, *The calculation of thermal conductivity, viscosity and thermodynamic properties for nanofluids on the basis of statistical nanomechanics.* International Journal of Heat and Mass Transfer, 2007. **50**(21–22): p. 4331-4341.

94. Vajjha, R.S. and D.K. Das, *Specific Heat Measurement of Three Nanofluids and Development of New Correlations.* Journal of Heat Transfer, 2009. **131**(7): p. 071601-071601-7.

95. Vajjha, R.S. and D.K. Das, *A review and analysis on influence of temperature and concentration of nanofluids on thermophysical properties, heat transfer and pumping power.* International Journal of Heat and Mass Transfer, 2012. **55**(15–16): p. 4063-4078.

96. Fakoor Pakdaman, M., M.A. Akhavan-Behabadi, and P. Razi, *An experimental investigation on thermo-physical properties and overall performance of MWCNT/heat transfer oil nanofluid flow inside vertical helically coiled tubes.* Experimental Thermal and Fluid Science, 2012. **40**: p. 103-111.

97. Einstein, A., *Eine neue Bestimmung der Moleküldimensionen.* Annalen der Physik, 1906. **324**(2): p. 289-306.

98. Krieger, I.M. and T.J. Dougherty, *A Mechanism for Non-Newtonian Flow in Suspensions of Rigid Spheres.* Trans. Soc. Rheol. , 1959. **3**(1): p. 137-152.

99. Prasher, R., P.E. Phelan, and P. Bhattacharya, *Effect of Aggregation Kinetics on the Thermal Conductivity of Nanoscale Colloidal Solutions (Nanofluid).* Nano Lett., 2006. **6**(7): p. 1529-1534.

100. Prasher, R., et al., *Measurements of nanofluid viscosity and its implications for thermal applications.* Appl. Phys. Lett., 2006. **89**(13): p. 133108.

101. Abareshi, M., et al., *Fabrication, characterization and measurement of thermal conductivity of Fe3O4 nanofluids.* J. Magn. Magn. Mater., 2010. **322**(24): p. 3895-3901.

102. Sundar, L.S., M.K. Singh, and A.C.M. Sousa, *Thermal conductivity of ethylene glycol and water mixture based Fe3O4 nanofluid.* Int. J. Heat Mass Transf. , 2013. **49**: p. 17-24.

103. Hamilton, R.L. and O.K. Crosser, *Thermal Conductivity of Heterogeneous Two-Component Systems.* Ind. Eng. Chem. Fundamen., 1962. **1**(3): p. 187-191.

104. Azmi, W.H., et al., *The enhancement of effective thermal conductivity and effective dynamic viscosity of nanofluids – A review.* Renew. Sustainable Energy Rev., 2016. **53**: p. 1046-1058.

105. Tawfik, M.M., *Experimental studies of nanofluid thermal conductivity enhancement and applications: A review.* Renew. Sustainable Energy Rev., 2016.

106. Hong, K., T.-K. Hong, and H.-S. Yang, *Thermal conductivity of Fe nanofluids depending on the cluster size of nanoparticles.* Applied Physics Letters, 2006. **88**(3): p. 031901.

107. Chen, H., et al., *Thermal conductivity of polymer-based composites: Fundamentals and applications.* Progress in Polymer Science, 2016. **59**: p. 41-85.

108. Xuan, Y. and Q. Li, *Investigation on Convective Heat Transfer and Flow Features of Nanofluids.* J. Heat Transfer, 2003. **125**(1): p. 151-155.

109. Vanaki, S.M., P. Ganesan, and H.A. Mohammed, *Numerical study of convective heat transfer of nanofluids: A review.* Renew. Sustainable Energy Rev., 2016. **54**: p. 1212-1239.

110. Sohn, C.H. and K.D. Kihm, *Nonhomogenous modeling of nanofluidic energy transport accounting for the thermophoretic migration of nanoparticles inside laminar pipe flows.* J. Korean Phys. Soc., 2009. **55**: p. 2200.

111. Bahiraei, M. and S.M. Hosseinalipour, *Particle migration in nanofluids considering thermophoresis and its effect on convective heat transfer.* Thermochimica Acta, 2013. **574**: p. 47-54.

112. Heyhat, M.M. and F. Kowsary, *Effect of Particle Migration on Flow and Convective Heat Transfer of Nanofluids Flowing Through a Circular Pipe.* J. Heat Transfer, 2010. **132**(6): p. 062401-062401-9.

113. Ryzhkov, I.I. and A.V. Minakov, *The effect of nanoparticle diffusion and thermophoresis on convective heat transfer of nanofluid in a circular tube.* Int. J. Heat Mass Transf., 2014. **77**: p. 956-969.

114. Hong, J., *An innovative application of nuclear magnetic resonance technology to complex flows*, in *Faculty of Engineering*. 2016, the University of Nottingham: Nottingham.

115. Motozawa, M., et al., *Effect of magnetic field on heat transfer in rectangular duct flow of a magnetic fluid.* Phys. Proc., 2010. **9**: p. 190-193.

116. Lajvardi, M., et al., *Experimental investigation for enhanced ferrofluid heat transfer under magnetic field effect.* J. Magn. Magn. Mater., 2010. **322**(21): p. 3508-3513.

117. Azizian, R., et al., *Effect of magnetic field on laminar convective heat transfer of magnetite nanofluids.* Int. J. Heat Mass Transf., 2014. **68**: p. 94-109.

118. Goharkhah, M., et al., *Convective heat transfer characteristics of magnetite nanofluid under the influence of constant and alternating magnetic field.* Powder Technology, 2015. **274**: p. 258-267.

119. Shahsavar, A., et al., *Experimental investigation on laminar forced convective heat transfer of ferrofluid loaded with carbon nanotubes under constant and alternating magnetic fields.* Exp. Thermal Fluid Sci., 2016. **76**: p. 1-11.

120. Ghofrani, A., et al., *Experimental investigation on laminar forced convection heat transfer of ferrofluids under an alternating magnetic field.* Exp. Therm. Fluid Sci., 2013. **49**: p. 193-200.

121. Yarahmadi, M., H. Moazami Goudarzi, and M.B. Shafii, *Experimental investigation into laminar forced convective heat transfer of ferrofluids under constant and oscillating magnetic field with different magnetic field arrangements and oscillation modes.* Exp. Therm. Fluid Sci., 2015. **68**: p. 601-611.

122. Good, R.J., *Contact angle, wetting, and adhesion: a critical review.* Journal of adhesion science and technology, 1992. **6**(12): p. 1269-1302.

123. Chen, X., et al., *Evaporation of droplets on superhydrophobic surfaces: Surface roughness and small droplet size effects.* Physical review letters, 2012. **109**(11): p. 116101.

124. Mangel Jr, R. and E. Baer, *The evaporation of water drops from a "Teflon" surface*. 1962, Pergamon.

125. Camarinha Lopes, M., *The influence of substrate's elasticity and thermal properties on drop evaporation*. 2013, Technische Universität.

126. Still, T., P.J. Yunker, and A.G. Yodh, *Surfactant-induced Marangoni eddies alter the coffee-rings of evaporating colloidal drops.* Langmuir, 2012. **28**(11): p. 4984-4988.

127. Zhong, X., A. Crivoi, and F. Duan, *Sessile nanofluid droplet drying.* Adv Colloid Interface Sci, 2015. **217**: p. 13-30.

128. Chen, R., et al., *Wetting and drying of colloidal droplets: physics and pattern formation.* Advances in Colloid Science, 2016: p. 3-25.

129. Uno, K., et al., *Particle adsorption in evaporating droplets of polymer latex dispersions on hydrophilic and hydrophobic surfaces.* Colloid and polymer science, 1998. **276**(9): p. 810-815.

130. Majumder, M., et al., *Overcoming the "coffee-stain" effect by compositional Marangoni-flow-assisted drop-drying.* The Journal of Physical Chemistry B, 2012. **116**(22): p. 6536-6542.

131. Orejon, D., *Study of nanosuspension droplets free evaporation and electrowetting.* 2013.

132. Sefiane, K., *On the role of structural disjoining pressure and contact line pinning in critical heat flux enhancement during boiling of nanofluids.* Applied physics letters, 2006. **89**(4): p. 044106.

133. Thokchom, A.K., et al., *Characterizing self-assembly and deposition behavior of nanoparticles in inkjet-printed evaporating droplets.* Sensors and Actuators B: Chemical, 2017. **252**: p. 1063-1070.

134. Wu, J., et al., *Generation of the smallest coffee-ring structures by solute crystallization reaction on a hydrophobic surface.* RSC advances, 2013. **3**(16): p. 5328-5331.

135. Moffat, J.R., K. Sefiane, and M.E. Shanahan, *Effect of TiO2 nanoparticles on contact line stick− slip behavior of volatile drops.* The Journal of Physical Chemistry B, 2009. **113**(26): p. 8860-8866.

136. Moffat, J.R., K. Sefiane, and M.E. Shanahan. *Nanofluid droplet evaporation kinetics and wetting dynamics on flat substrates*. in *Journal of Nano Research*. 2009. Trans Tech Publ.

137. Orejon, D., K. Sefiane, and M.E. Shanahan, *Stick–slip of evaporating droplets: substrate hydrophobicity and nanoparticle concentration.* Langmuir, 2011. **27**(21): p. 12834-12843.

138. Adachi, E., A.S. Dimitrov, and K. Nagayama, *Stripe patterns formed on a glass surface during droplet evaporation.* Langmuir, 1995. **11**(4): p. 1057-1060.

139. Yakhno, T.A., et al., *The informative-capacity phenomenon of drying drops.* IEEE engineering in medicine and biology magazine, 2005. **24**(2): p. 96-104.

140. Chen, G. and G.J. Mohamed, *Complex protein patterns formation via salt-induced self-assembly and droplet evaporation.* The European Physical Journal E, 2010. **33**(1): p. 19-26.

141. Kaya, D., V. Belyi, and M. Muthukumar, *Pattern formation in drying droplets of polyelectrolyte and salt.* The Journal of chemical physics, 2010. **133**(11): p. 114905.

142. Gorr, H.M., et al., *Salt-induced pattern formation in evaporating droplets of lysozyme solutions.* Colloids and Surfaces B: Biointerfaces, 2013. **103**: p. 59-66.

143. Yakhno, T., et al., *Drops of biological fluids drying on a hard substrate: Variation of the morphology, weight, temperature, and mechanical properties.* Technical Physics, 2010. **55**(7): p. 929-935.

144. Tarasevich, Y.Y. and A. Ayupova, *Effect of diffusion on the separation of components in a biological fluid upon wedge-shaped dehydration.* Technical Physics, 2003. **48**(5): p. 535-540.

145. Yakhno, T., *Sodium chloride crystallization from drying drops of albumin–salt solutions with different albumin concentrations.* Technical Physics, 2015. **60**(11): p. 1601-1608.

146. Sefiane, K., *On the formation of regular patterns from drying droplets and their potential use for bio-medical applications.* Journal of Bionic Engineering, 2010. **7**: p. S82-S93.

147. Lee, H., et al., *Study of residue patterns of aqueous nanofluid droplets with different particle sizes and concentrations on different substrates.* International Journal of Heat and Mass Transfer, 2017. **105**: p. 230-236.

148. Chon, C.H., et al., *Effect of nanoparticle sizes and number densities on the evaporation and dryout characteristics for strongly pinned nanofluid droplets.* Langmuir, 2007. **23**(6): p. 2953-2960.

149. Jung, J.-Y., Y.W. Kim, and J.Y. Yoo, *Behavior of particles in an evaporating didisperse colloid droplet on a hydrophilic surface.* Analytical chemistry, 2009. **81**(19): p. 8256-8259.

150. Wong, T.-S., et al., *Nanochromatography driven by the coffee ring effect.* Analytical chemistry, 2011. **83**(6): p. 1871-1873.

151. Sempels, W., et al., *Auto-production of biosurfactants reverses the coffee ring effect in a bacterial system.* Nature communications, 2013. **4**(1): p. 1-8.

152. Patil, N.D., et al., *Effects of substrate heating and wettability on evaporation dynamics and deposition patterns for a sessile water droplet containing colloidal particles.* Langmuir, 2016. **32**(45): p. 11958-11972.

153. Li, Y.-F., Y.-J. Sheng, and H.-K. Tsao, *Evaporation stains: suppressing the coffee-ring effect by contact angle hysteresis.* Langmuir, 2013. **29**(25): p. 7802-7811.

154. Parsa, M., et al., *Effect of substrate temperature on pattern formation of nanoparticles from volatile drops.* Langmuir, 2015. **31**(11): p. 3354-3367.

155. Kim, J.-H., et al., *Polymer transports inside evaporating water droplets at various substrate temperatures.* The Journal of Physical Chemistry C, 2011. **115**(31): p. 15375-15383.

156. Hu, Y.-C., et al., *Peculiar surface profile of poly (ethylene oxide) film with ring-like nucleation distribution induced by Marangoni flow effect.* Colloids and Surfaces A: Physicochemical and Engineering Aspects, 2013. **428**: p. 39-46.

157. WH, A., *Engine coolant testing: state of the art*. 1980: ASTM STP 705.

158. Israelachvili, J. and H. Wennerström, *Role of hydration and water structure in biological and colloidal interactions.* Nature, 1996. **379**(6562): p. 219.

159. Sperling, R.A. and W.J. Parak, *Surface modification, functionalization and bioconjugation of colloidal inorganic nanoparticles.* Philosophical Transactions of the Royal Society of London A: Mathematical, Physical and Engineering Sciences, 2010. **368**(1915): p. 1333-1383.

160. Neouze, M.-A. and U. Schubert, *Surface modification and functionalization of metal and metal oxide nanoparticles by organic ligands.* Monatshefte für Chemie-Chemical Monthly, 2008. **139**(3): p. 183-195.

161. Jung, J.-Y. and J.Y. Yoo, *Thermal conductivity enhancement of nanofluids in conjunction with electrical double layer (EDL).* International Journal of Heat and Mass Transfer, 2009. **52**(1-2): p. 525-528.

162. Saeedinia, M., M.A. Akhavan-Behabadi, and M. Nasr, *Experimental study on heat transfer and pressure drop of nanofluid flow in a horizontal coiled wire inserted tube under constant heat flux.* Experimental Thermal and Fluid Science, 2012. **36**: p. 158-168.

163. Malekzadeh, A., et al., *Experimental Investigations on the Viscosity of Magnetic Nanofluids under the Influence of Temperature, Volume Fractions of Nanoparticles and External Magnetic Field.* Journal of Applied Fluid Mechanics, 2016. **9**(2).

164. Karimi, A., et al., *Experimental investigation on thermal conductivity of MFe2O4 (M= Fe and Co) magnetic nanofluids under influence of magnetic field.* Thermochimica Acta, 2014. **598**: p. 59-67.

165. Özerinç, S., S. Kakaç, and A.G. Yazıcıoğlu, *Enhanced thermal conductivity of nanofluids: a state-of-the-art review.* Microfluid Nanofluid, 2010. **8**(2): p. 145-170.

166. Buongiorno, J., et al., *A benchmark study on the thermal conductivity of nanofluids.* Journal of Applied Physics, 2009. **106**(9): p. 094312.

167. Jiang, H., et al., *Effective thermal conductivity of nanofluids considering interfacial nano-shells.* Mater. Chem. Phys., 2014. **148**(1–2): p. 195-200.

168. Yu, W. and S.U.S. Choi, *The Role of Interfacial Layers in the Enhanced Thermal Conductivity of Nanofluids: A Renovated Maxwell Model.* J. Nanopart. Res., 2003. **5**(1): p. 167-171.

169. Nan, C.-W., et al., *Effective thermal conductivity of particulate composites with interfacial thermal resistance.* J. Appl. Phys., 1997. **81**(10): p. 6692-6699.

170. Jang, S.P. and S.U.S. Choi, *Role of Brownian motion in the enhanced thermal conductivity of nanofluids.* Appl. Phys. Lett., 2004. **84**(21): p. 4316-4318.

171. Koo, J. and C. Kleinstreuer, *A new thermal conductivity model for nanofluids.* J. Nanopart. Res., 2004. **6**(6): p. 577-588.

172. Koo, J. and C. Kleinstreuer, *Impact analysis of nanoparticle motion mechanisms on the thermal conductivity of nanofluids.* Int. Commun. Heat Mass Transf., 2005. **32**(9): p. 1111-1118.

173. Sieder, E.N. and G.E. Tate, *Heat Transfer and Pressure Drop of Liquids in Tubes.* Ind. Eng. Chem., 1936. **28**(12): p. 1429-1435.

174. Moffat, R.J., *Describing the uncertainties in experimental results.* Exp. Therm. Fluid Sci., 1988. **1**(1): p. 3-17.

175. Askounis, A., et al., *"Biodrop" Evaporation and Ring-Stain Deposits: The Significance of DNA Length.* Langmuir, 2016. **32**(17): p. 4361-4369.

176. Dague, E., et al., *Assembly of live micro-organisms on microstructured PDMS stamps by convective/capillary deposition for AFM bio-experiments.* Nanotechnology, 2011. **22**(39): p. 395102.

177. Abareshi, M., et al., *Fabrication, characterization and measurement of thermal conductivity of Fe3O4 nanofluids.* Journal of Magnetism and Magnetic Materials, 2010. **322**(24): p. 3895-3901.

178. Liu, Z., et al., *Enhancement of solar energy collection with magnetic nanofluids.* Thermal Science and Engineering Progress, 2018. **8**: p. 130-135.

179. Li, Y., et al., *From coffee rings to coffee eyes.* Soft Matter, 2015. **11**(23): p. 4669-4673.

180. Deegan, R.D., et al., *Contact line deposits in an evaporating drop.* Physical review E, 2000. **62**(1): p. 756.

181. McGrew, J.L., F.L. Bamford, and T.R. Rehm, *Marangoni flow: an additional mechanism in boiling heat transfer.* Science, 1966. **153**(3740): p. 1106-1107.

182. Shatat, M., A. Mayere, and S. Riffat, *A standardized empirical method of testing solar simulator coupled with solar tube and concentrator collectors.* Internacional Journal of thermal & environmental engineering, 2013. **5**(1): p. 13-20.

183. Karimi, A., et al., *Thermal Conductivity of $$\mathrm {Fe} _ {2}\mathrm {O} _ {3} $$ and $$\mathrm {Fe} _ {3}\mathrm {O} _ {4} $$ Fe3O4 Magnetic Nanofluids Under the Influence of Magnetic Field.* International Journal of Thermophysics, 2015. **36**(10-11): p. 2720-2739.

184. Bakos, G., et al., *Design, optimisation and conversion-efficiency determination of a line-focus parabolic-trough solar-collector (PTC).* Applied energy, 2001. **68**(1): p. 43-50.

185. Nkurikiyimfura, I., Y. Wang, and Z. Pan, *Effect of chain-like magnetite nanoparticle aggregates on thermal conductivity of magnetic nanofluid in magnetic field.* Experimental Thermal and Fluid Science, 2013. **44**: p. 607-612.

186. Philip, J., P. Shima, and B. Raj, *Evidence for enhanced thermal conduction through percolating structures in nanofluids.* Nanotechnology, 2008. **19**(30): p. 305706.

187. Zhang, L., et al., *Radiative properties of ionic liquid-based nanofluids for medium-to-high-temperature direct absorption solar collectors.* Solar Energy Materials and Solar Cells, 2014. **130**: p. 521-528.

188. Hordy, N., et al., *High temperature and long-term stability of carbon nanotube nanofluids for direct absorption solar thermal collectors.* Solar Energy, 2014. **105**: p. 82-90.

Appendix

Experimental Study of Solar Energy Collection with Magnetic Nanofluids

The test rig for the parabolic trough solar collector is modified on the basis of the thermal convection test rig as shown in Figure 1.

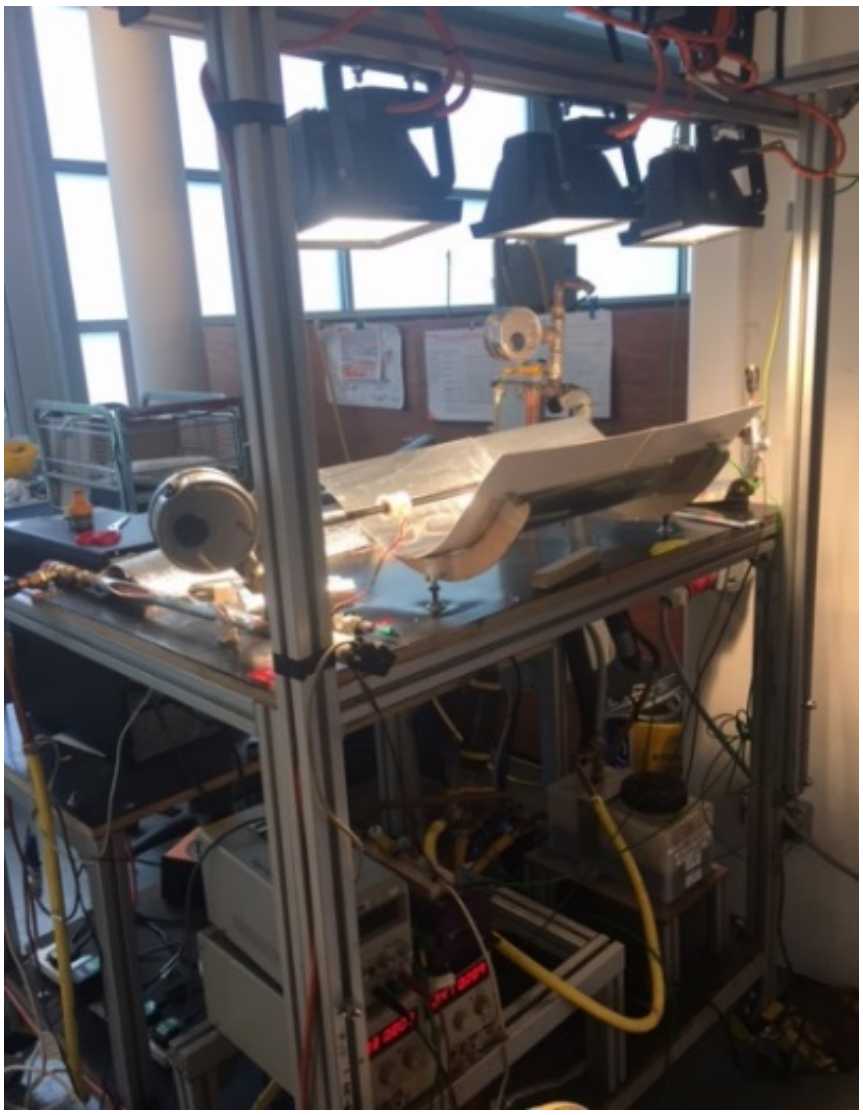


Figure 1 Experimental setup for parabolic trough solar collector.

Respectively, the solar simulator contains three tungsten halogen lamps, which can provide a stable spectral output ranging from 360-2500 nm [182]. Some experimental tests were carried out for various distances of the light surface from the simulator surface to investigate the unevenness of variations in the light

distribution. The absorber tube is made of the borosilicate glass, which allows MNFs to absorb radiation directly. Three solenoids fed by transistorized regulated DC power supply are used to generate magnetic field parallel to the flow direction. The intensity of the magnetic field is measured with a Gauss meter. A reflective mirror, with 1mm thick high impact polystyrene sheet, is used to concentrate the radiation to the absorber tube. A pyranometer is used to measure the solar radiation, which is in a good agreement with British standards for testing a solar simulator. The flow rate is measured by an ultrasonic flow meter, FLOWNETIX 100. Two non-magnetic type T thermal couples are positioned to measure the inlet and outlet temperature. At the beginning of each test, the solar simulator is turned on first. It takes 30 minutes for the solar simulator to reach the maximum intensity and keep stable. A water bath is used to control the inlet temperature of fluids. The parameters of the parabolic trough are shown in Table 5.

Table 5 Parameters of the parabolic trough and test conditions

Parameters	**Values**
Length of the receiver	500 mm
Width of the aperture	250 mm
Outer diameter of absorbers	15 mm
Solar irradiance	1000 W/m^2
Mass flow	0.02 kg/s

The useful heat absorbed by MNFs is calculated by equation (1),

$$\dot{Q}_U = \dot{m}_f C_{p,f}(T_{out} - T_{in}) \quad (1)$$

where $\dot{m}_f$ refers to mass flow of modified magnetic nanofluids, $C_{p,f}$ refers to specific heat capacity of MNFs given by equation (2),

$$C_{p,f} = (1 - \varphi)C_{p,w} + \varphi C_{p,np} \quad (2)$$

where $C_{p,w}$and $C_{p,np}$ refers to the temperature dependent specific heat capacity of both water and nanoparticles. And heat capacity at the mean temperature T_m is given as equation (3),

$$T_m = \frac{T_{in} + T_{out}}{2} \quad (3)$$

The thermal efficiency can be calculated by equation (4),

$$\eta = \frac{\dot{Q}_U}{I_D A_C} \quad (4)$$

where η refers to thermal efficiency of the parabolic trough is, I_D is the direct solar radiation and A_C is the area of the collector.

The solar radiation uncertainty is less than 2%. The uncertainty of the mass flow is less than 1%. Uncertainties for inlet and outlet temperatures are less than 0.1 °C. Complex uncertainty is calculated by equation (5) and is between 1% and 5.2%, which are calculated by equation (5)

$$U_\eta = \sqrt{\left(\frac{\partial \eta}{\partial \dot{m}_f} U_{\dot{m}}\right)^2 + \left(\frac{\partial \eta}{\partial I_D} U_{I_D}\right)^2 + \left(\frac{\partial \eta}{\partial T_{out}} U_{T_{out}}\right)^2 + \left(\frac{\partial \eta}{\partial T_{in}} U_{T_{in}}\right)^2} \quad (5)$$

Results and discussion

Thermal efficiency of the parabolic trough solar collector is investigated with CA modified magnetic nanofluids. Meanwhile, there are two significant influencing factors, namely concentration (0% and 0.05%), and magnetic field strength, ranging from 0 mT to 10.47 mT. the intensity of the magnetic field is similar to the thermal conductivity of magnetic nanofluids [183].

As shown in Figure 2, we first study the thermal efficiency of the base liquid with the selective surface, meanwhile, direct absorption tube for the base liquid and ferrofluids of 0.05% is also investigated with the absence of the magnetic field strength under laminar flow condition. It is shown that thermal efficiency of the selective surface is 26.3%, of which the inlet temperature is close to the ambient environment. Thermal efficiency decreases with inlet temperature. The lowest thermal efficiency of the selective surface is only 14.8%, which is much less than the conventional parabolic trough. This is because the optical efficiency in the experiment is 70%, which is less than that of the conventional parabolic trough of 95%. Based on BS EN ISO 9806:2013 standard, unglazed collector defines as concentrating collectors without the transparent cover and the low concentration ratio. On the other hand, the high heat loss is also the other issue for the low thermal efficiency compared to the conventional one, which is caused by the small diameter and the small concentration ratio of the test section. The collector can minimize heat loss when the high concentration ratio is applied, but high demands on manufacturing [184]. When it comes to the base liquid with direct absorption tube, thermal efficiency is only 10%. Under this condition, the inlet temperature of the test section is 30.04 °C, and the ambient temperature is 20.23 °C. In addition, 0.05% ferrofluids are also investigated with the absence of the magnetic field with the highest thermal efficiency of 16% and the lowest efficiency of 6%. In this case, inlet and ambient temperatures are 30.04 °C and 20.23 °C respectively. Compare to the base liquid, the thermal efficiency of ferrofluids with 0.05% exhibits much more enhancement to the base liquid, which is around 6% higher.

In addition, magnetic nanofluids of 0.05% are also studied with different magnetic intensities. Generally, the experimental trends show that thermal efficiency increases with the increasing magnetic strength when the orientation of the magnetic field is parallel to the direction of the flow. The maximum thermal efficiency reaches 40% when magnetic intensity comes to 10.47mT. When the magnetic field is applied with 3.14mT and 6.28mT, the maximum efficiencies are 30% and 34% respectively. Moreover, magnetic nanofluids absorb solar radiation can gain more thermal efficiency than selective surface absorber in the presence of the magnetic field. However, it is clear that a bigger diameter is required to absorb the entire solar radiation and decrease thermal losses.

In this experiment, nanoparticles improve the heat transfer performance, allowing heat transfer faster from the absorber surface to the fluid. There are many mechanisms made to explain the enhancement of ferrofluids, including ballistic phonon transport, Brownian motion induced micro-convection and the aggregation of nanoparticles. Among them, conduction path through agglomerates is one possible influencing factors responsible for the big enhancement [185, 186]. With the applied magnetic field, chain-like structures of nanoparticles are formed in the magnetic nanofluids, which transfer heat faster through the metal chain. The length of the chain increases with the increasing magnetic field, more thermal conduction paths are created along the magnetic field direction. In optical properties, both the absorption and the scattering are improved compare to the base liquid. The enhancement is a function of nanoparticles size, concentration and the optical path length [187, 188]. In the presence of the external magnetic field, the chain-like structure will allow less radiation to transmit through the fluid. Higher heat transfer

performance can be reached if the solar radiation is completely absorbed by the nanoparticles distant from the absorber tube. Therefore, optical enhancement plays a bigger role in the collector efficiency. An optimal nanoparticle concentration, magnetic intensity, and tube diameter should be further investigated. For all these reasons thermal efficiency of a solar collector with direct absorber tube increases by using ferrofluids and becomes higher than a selective surface tube parabolic trough. Increasing the magnetic field further will not affect the thermal efficiency because the particles reached a saturation magnetization. This work shows the capability of using ferrofluids in the direct absorption parabolic trough. However, further work needs to be carried on making it applicable. The thermal and optical loss of the current work needs to be reduced. Higher operation temperatures, higher concentration ratios, larger glass tube with anti-reflection, using an envelope to decrease the thermal loss, and a high-quality reflector is required to compare the performance of ferrofluids parabolic trough solar collector with the commercial parabolic trough.

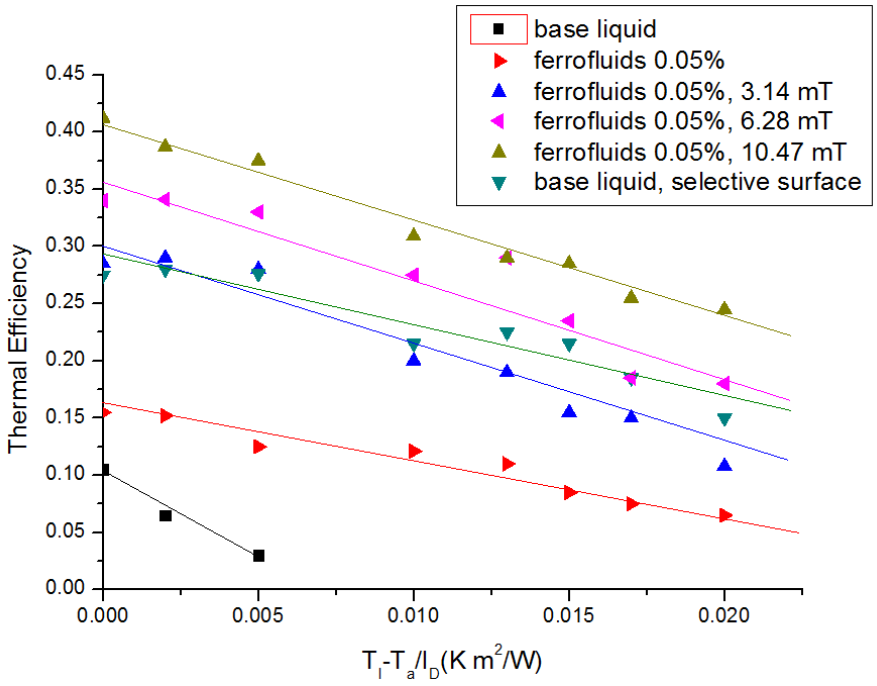


Figure 2 Thermal efficiency comparation of water and MNFs with and without magnetic field.